Accessing the quantum world through electronic transport in carbon nanotubes

INAUGURALDISSERTATION

zur
Erlangung der Würde eines Doktors der Philosophie
vorgelegt der
Philosophisch-Naturwissenschaftlichen Fakultät
der Universität Basel
von

Matthias Rudolf Gräber

aus Deutschland

Basel, 2006

Genehmigt von der Philosophisch-Naturwissenschaftlichen Fakultät auf Antrag der Herren Professoren:

Prof. Dr. C. Schönenberger
Prof. Dr. J.P. Kotthaus
Prof. Dr. W. Belzig

Basel, den 3. März 2006

Prof. Dr. H.-J. Wirz, Dekan

Contents

Introduction **ix**

1 Carbon nanotubes: Structure, growth and electrical contacts **1**
1.1 Geometry and energy dispersion of nanotubes 1
1.2 Growth by chemical vapor deposition 5
1.3 Making nanotube-based electrical devices 6

2 Charge transport in mesoscopic systems **13**
2.1 A few remarks 13
2.2 Conductance, transmission and interference 13
2.3 Quantum dots 15
2.4 Transport through a normal-superconductor junction 18
2.5 Double quantum dots 20

3 Quantum dot coupled to a normal and a superconducting lead **29**
3.1 Motivation 29
3.2 Sample fabrication and measurement 29
3.3 Kondo regime 31
3.4 Modelling the data 35
3.5 Coulomb blockade regime 41
3.6 Summary 41

4 Local gating of carbon nanotubes **45**
4.1 Motivation 45
4.2 Experimental 45
4.3 Local gating at room temperature 48
4.4 Local gating at low temperatures 51

5 Carbon nanotube double quantum dots **59**
5.1 Motivation 59
5.2 Sample preparation and characterization 60
5.3 Double quantum dot behavior 61
5.4 Extracting the tunnel coupling 63
5.5 Molecular states 65

5.6 Temperature dependence 67
5.7 Control experiment with a second device 69
5.8 DC measurements 70
5.9 Mapping the molecular wavefunctions 71
5.10 Summary 74

A Electrical measurements and cryostats **79**
A.1 Measurement setup 79
A.2 Electronic temperature 81
A.3 Cryostats 81

B Additional data **85**
B.1 Approaching the few-hole regime 85
B.2 Influence of the center gate on the dot-dot coupling 87

C CVD-growth recipe for single-walled carbon nanotubes **89**
C.1 Catalyst preparation 89
C.2 Growth protocol methane/hydrogen process 90

Publication list **95**

Curriculum Vitae **99**

Acknowledgements **101**

List of Figures

1.1 Sketch of a graphene sheet 2
1.2 Structure of carbon nanotubes 3
1.3 Band structure of graphene 4
1.4 Energy dispersion of a (5,5) and a (9,0) nanotube 5
1.5 Setup of the CVD apparatus 6
1.6 Schematics of a nanotube FET 7
1.7 SEM micrograph of nanotubes on SiO_2 7
1.8 Zoom into a nanotube device 8

2.1 Schematics and stability diagram of a quantum dot 15
2.2 Coulomb diamonds in a SWNT 16
2.3 Fabry-Perot oscillations in a SWNT 18
2.4 Illustration of a normal-superconducting interface 19
2.5 Differential conductance through an N-S interface 20
2.6 Schematics of a double quantum dot 21
2.7 Stability diagram of double dots 23
2.8 Two-level system 24

3.1 Schematics and SEM micrograph of an S-MWNT-N device . . . 30
3.2 Conductance in the normal and superconducting state 31
3.3 Temperature dependence of the Kondo conductance 32
3.4 Energy diagram of an S-quantum dot-N device 35
3.5 Comparison with resonant S-N transport 36
3.6 Comparison with a tunneling model 39
3.7 Conductance in the Coulomb blockade regime 40

4.1 Fabrication procedure of top-gate electrodes 46
4.2 SEM micrographs of nanotubes with two and three top-gates . . 47
4.3 Top-gate response at 300 K 48
4.4 Potential in a two top-gate device 49
4.5 Bending of bands due to local gates 50
4.6 Hysteresis of back-gate versus top-gate 52
4.7 Colorscale plot of the conductance at 77 and 4.2 K 53
4.8 Coulomb diamonds measured in a two top-gate device 54

4.9 Colorscale plot of the conductance versus top-gate voltages at 4.2 K 55

5.1 Schematics and SEM micrograph of the device 60
5.2 Honeycomb pattern of an SWNT double dot 62
5.3 Level repulsion in an SWNT double dot 64
5.4 Triple point region at finite bias 66
5.5 Temperature dependence of the conductance 68
5.6 Honeycomb pattern measured in a second sample 70
5.7 DC measurement of an SWNT double dot 71
5.8 Honeycomb pattern measured in a third sample 72
5.9 Mapping the wavefunctions 73

A.1 Electrical setup 80
A.2 Electronic temperature 81
A.3 Schematics of a dilution refrigerator 83

B.1 Few hole regime 85
B.2 Influence of the center gate 88

In this house, we obey
the laws of thermodynamics!

Homer Simpson

The cover picture shows a colorscale plot of the electrical conductance through a single-walled carbon nanotube at a temperature of 4.2 K when sweeping the voltages applied on locally acting top-gate electrodes.

Cover layout by Anna Schorner (annasch@gmx.ch).

Introduction

It was on December 23, 1947 when the first transistor was invented at Bell Laboratories by William Shockley, John Bardeen, and Walter Brattain [1]. This was perhaps the most important discovery in information technology in the 20th century setting off what is now known as the semiconductor revolution. Important steps such as the first integrated circuit (IC) by Jack Kilby in 1958, or the first IC available on a monolithic chip by Fairchild Corp. in 1961 followed and have finally resulted in a dramatic minituarization of semiconductor devices. Since 1960 the IC complexity has followed "Moore's Law", predicting a doubling of circuit density or capacity of semiconductor devices every 18 months [2].

Meanwhile lithography has reached IC feature sizes of 100 nm, approaching the ultimate limits of optical lithography, and gate oxide thicknesses have become as low as 1.7 nm [3]. From this fact, two problems arise. First, there is a need for new techniques allowing one to produce reliably features on the nm scale. Second, at theses dimensions, quantum effects can enter the game and drastically modify the performance of the logic devices. How to overcome this problem? Possible solutions to these problems may be provided by the emerging field of molecular electronics.

There are two basic devices people try to construct in molecular electronics, which can be distinguished as classical and quantum molecular transistor. The classical molecular transistor can be considered as a scaling of a field effect transistor down to the nm-scale without modifying the physical mechanism of operation. The quantum molecular transistor, however, additionally makes use of quantum effects in its device operation.

Since their discovery in 1991 [4], carbon nanotubes have been envisioned and realized for both types of devices. Due to their semiconducting behavior (2/3 of all nanotubes) they have been used as classical field effect transistors at room temperature with the potential of being integrated into Si-based electronics within the coming 20-30 years. At lower temperatures (below $\approx$ 20 K) the energy scales of quantum effects become accessible and carbon nanotubes have proven to be a fertile ground for the exploration of quantum electronics. Under these conditions carbon nanotubes become a mesoscopic system, where particles behave like extended objects with wave character. In fact, carbon nanotubes offer an experimentally easy accessible system for the quantum mechanics textbook example of a particle in a box, called quantum dot or artificial atom [5, 6].

Much of the following thesis will be devoted to the quantum dot behavior of carbon nanotubes. They represent an alternative system as compared to artificial atoms gate-defined in GaAs-based two-dimensional electron gas systems in which researchers have achieved an amazing degree of control over the system [7]. However, quantum dot physics in carbon nanotubes is not just about copying what has already been done in semiconductor structures. Due to the unique properties of nanotubes, new physics such as the effect of superconducting and ferromagnetic correlations on electronic transport through a single quantum-mechanical state can be probed [8, 9, 10]. In addition the big energy scales of nanotubes caused by the tiny diameter allow for operation of quantum dot devices at higher temperatures. When it is possible to obtain an even larger degree of control over carbon nanotube quantum dots, it seems thinkable to create quantum bits [11] or entangled Einstein-Podolsky-Rosen (EPR) pairs [12] on a solid state basis [13, 14, 15]. Many exciting quantum phenomena remain to be addressed in experiments; carbon nanotubes may provide a well-suited platform.

This thesis

In this thesis we will focus on

(a) *superconducting electrodes attached to carbon nanotube quantum dots* in order to study the effects of superconducting correlations on quantum systems and

(b) *local gate control of carbon nanotubes* in order to define and control double quantum dot systems in carbon nanotubes. As it turns out, local gates are an important tool for increasing the control over quantum states in nanotubes.

The thesis is structured as follows:

- Chapter 1 gives a brief introduction to the chemical and electronic properties of carbon nanotubes and the experimental procedures necessary for manufacturing electrical devices with single carbon nanotubes.
- In Chapter 2 selected topics of charge transport in mesoscopic systems, such as single and coupled quantum dots, are reviewed.
- In Chapter 3 we present electrical transport measurements through a carbon nanotube coupled to a normal and a superconducting lead - a test system for the exploration of the nature of many-particle correlations.
- Chapter 4 describes how to achieve local gate control over semiconducting carbon nanotubes by adding top-gate electrodes.
- In Chapter 5 double quantum dots are defined and controlled inside a carbon nanotube. The system allows for the observation of molecular states induced by a large tunnel coupling of the dots; an artificial molecule is defined inside a real one.

References

[1] W. Shockley, US Patent 02569347 .

[2] G. Moore, Proc. IEDM 11 (1975).

[3] B. Foeste, MOSFET-The Workhorse of Microelectronics, Talk at the 4. Dresdner Sommerschule Mikroelektronik (2003).

[4] S. Iijima, Nature **354**, 56 (1991).

[5] M. Kastner, Physics Today **46**, 24 (1993).

[6] M. Bockrath *et al.*, Science **275**, 1922 (1997).

[7] L. Kouwenhoven *et al.*, Proceedings of the Advanced Study Institute on Mesoscopic Electron Transport, edited by L.L. Sohn, L.P. Kouwenhoven, G. Schön (Kluwer). (1997).

[8] S. Sahoo *et al.*, Nature Physics **1**, 99 (2005).

[9] M. Buitelaar, T. Nussbaumer, and C. Schönenberger, Phys. Rev. Lett. **89**, 256801 (2002).

[10] M. Buitelaar *et al.*, Phys. Rev. Lett. **91**, 057005 (2003).

[11] D. Loss and D. DiVincenzo, Phys. Rev. A **57**, 120 (1998).

[12] A. Einstein, B. Podolsky, and N. Rosen, Phys. Rev. **47**, 777 (1935).

[13] C. Bena, S. Vishveshwara, L. Balents, and M. Fisher, Phys. Rev. Lett. **89**, 037901 (2002).

[14] V. Bouchiat *et al.*, Nanotechnology **14**, 77 (2003).

[15] P. Recher and D. Loss, Phys. Rev. B **65**, 165327 (2002).

Chapter 1

Carbon nanotubes: Structure, growth and electrical contacts

1.1 Geometry and energy dispersion of nanotubes

There are different manifestations of the element carbon. Besides the well-known graphite and diamond, researchers have discovered two further forms. In 1986 fullerenes were reported, tiny spheres (diameter $\approx$ 1 nm) with all carbon atoms at the surface [1]. Then, in 1991 carbon nanotubes followed, two-dimensional sheets of graphene rolled up into long and thin cylinders [2]. Due to their unique geometries, both fullerenes and nanotubes have attracted an enormous scientific interest. In particular, carbon nanotubes are often considered to be the prime example of a one-dimensional system.

Carbon nanotubes are long cylinders rolled up out of two-dimensional sheets of hexagonally-arranged carbon atoms, so-called graphene. One distinguishes single-walled carbon nanotubes (SWNT) consisting only of one graphene sheet and multi-walled carbon nanotubes (MWNT) with typically 10-20 rolled up sheets. The diameters range from $\approx$ 1 nm for SWNTs to $\approx 10 - 20$ nm in the case of MWNTs. Carbon nanotubes can be fairly long, lengths of up to 4 cm have been reported [3]. A specific carbon nanotube is defined by a vector $\vec{C} = n\vec{a}_1 + m\vec{a}_2$ with $\vec{a}_1$ and $\vec{a}_2$ being the unit vectors of the hexagonal lattice and n,m integers. A pair (n,m) then corresponds to a specific set of tube diameter d and chiral angle ϕ:

$$d = a/\pi\sqrt{(n^2 + m^2 + nm)} \ , \tag{1.1}$$

$$\phi = arccos(\sqrt{3}(n+m)/2\sqrt{(n^2 + m^2 + nm)}) \ . \tag{1.2}$$

Figure 1.1 shows the hexagonal graphene lattice and the corresponding lattice

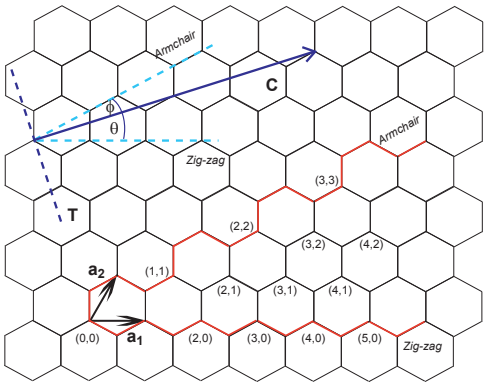

Figure 1.1: Sketch of a graphene sheet. The nearest-neighbor-distance is $a_0 = 1.42$ Å.

vectors $\vec{a}_1$ and $\vec{a}_2$. Axis with special symmetries are the zigzag (n,0) and armchair (n,n) directions named according to the line-shape of a tube circumference following the carbon atoms. There are many possible ways of rolling up a two-dimensional graphene sheet into a nanotube. In general one distinguishes three classes of nanotubes:

- armchair (n,0)
- zig-zag (n,n)
- chiral (n,m)

The structure of these three types of carbon nanotubes and a scanning tunneling microscope image of a chiral SWNT are illustrated in Fig. 1.2.

As it turns out, the wrapping vector finally determines whether the SWNT is semiconducting or metallic. Three out of the four valence electrons of carbon form a strong sp^2 σ-bond with the three nearest neighbors on the hexagonal graphene lattice. The orbitals lie in plane with an included angle of 120°. The remaining, fourth electron resides in a π-orbital extending perpendicular to the graphene plane. Since the π-bonds are much weaker than the σ-bonds the electronic properties of carbon nanotubes are well described taking into account only the π-electrons per unit cell [5, 6, 7]. Note that the unit cell of the hexagonal lattice contains 2 atoms and thus 2 π-electrons.

From the energy dispersion of the π-electrons of a graphene sheet as obtained from a tight-binding calculation [8] it follows that they can be either in a bonding (-) or an anti-bonding (+) band:

$$E(k_x, k_y) = \pm\gamma_0[1 + 4cos(\frac{\sqrt{3}k_x a}{2})cos(\frac{k_y a}{2}) + 4cos^2(\frac{k_y a}{2})]^{1/2} \ . \qquad (1.3)$$

Here $\gamma_0 = 2.5\,eV$ is the energy overlap integral between the nearest neighbours. Figure 1.3 shows a three-dimensional plot of the energy dispersion of graphene. The bonding (conduction) band and the anti-bonding (valence) band meet at

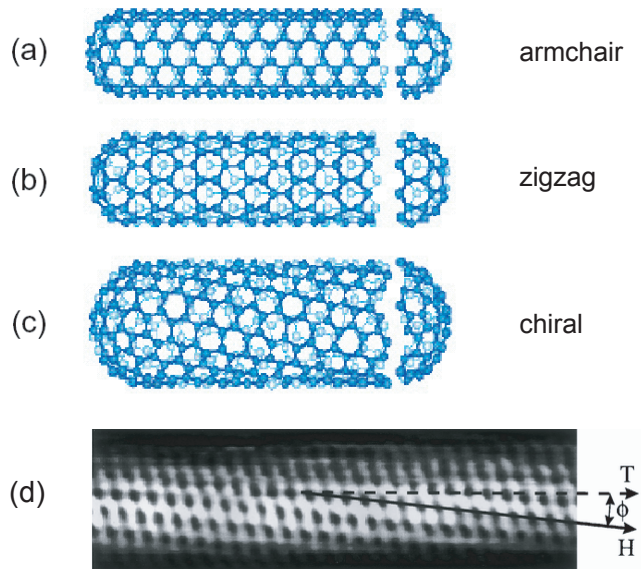

Figure 1.2: Different nanotube structures: (a) A (5,5) armchair tube. (b) A (9,0) zigzag tube. (c) A (10,5) chiral tube. (d) Atomically resolved STM image of an individual SWNT. The diameter was found to be d=1.3 nm and the chiral angle $\phi = 7°$. Adapted from reference [4].

six distinct points corresponding to the corners of the first Brillouin zone. These points are referred to as K-points. Three out of the six K-points are equivalent due to the spatial symmetry of the hexagonal lattice, thus two distinguishable points remain called K and K'.

So far, the discussion has been limited to an infinite, planar graphene sheet. When rolling up such a sheet to a seamless cylinder and forming a nanotube, an additional quantization condition for the wave vector component perpendicular to the tube direction arises. The scalar product of the electronic wave vector $\vec{k}$ and $\vec{C}$ has to be an integer multiple of 2π, resulting in the following quantization for the absolute value of the perpendicular component $\vec{k}_\perp$:

$$\mid \vec{k}_{\perp,p} \mid = 2\pi \frac{(m-n)/3+p}{\pi d} \tag{1.4}$$

where p is an integer and d denotes the tube diameter. This condition is fulfilled in planes perpendicular to the $k_x - k_y$-plane. The energy dispersion for a nanotube thus can be obtained by taking slices through the graphene energy dispersion plotted in Fig. 1.3. One can show that the one-dimensional band

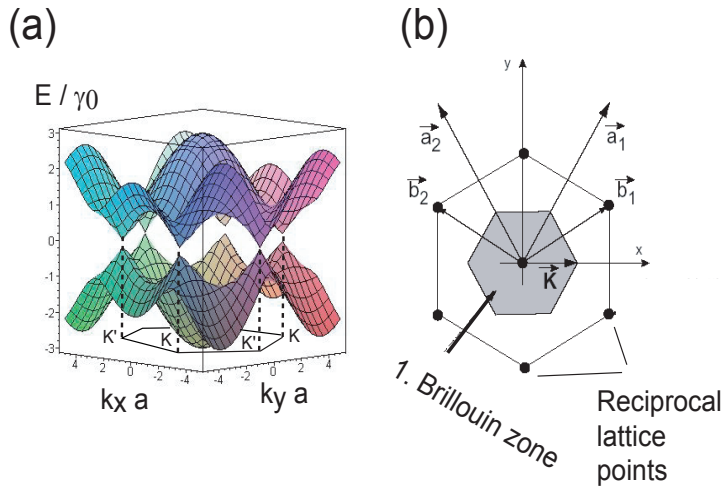

Figure 1.3: (a) Band structure of graphene. The valence and conduction band meet at six points corresponding to the corners of the first Brillouin zone shown in (b). Due to spatial symmetry, two sets of these points, K and K', are inequivalent.

structure of (n,m) carbon nanotubes in the vicinity of the fermi energy is given by [9]:

$$E_p(k_\parallel) = \pm\frac{2hv_F}{d}\sqrt{(\frac{m-n}{3}+p)^2+(\frac{k_\parallel d}{2})^2}\ . \tag{1.5}$$

Here h is Planck's constant and $v_F = 8 \times 10^{-5}$ m/s is the Fermi velocity of graphene. Whether the nanotube is semiconducting or metallic is determined by the first bracket within the square root of Eq. (1.5). If m-n = 3N with N an integer, there will always be an integer $p = -N$ forcing the bracket to equal zero. In this case there will be no energy gap around $k_\parallel = 0$, i.e. the tube will be metallic. Else the tube will be semiconducting. When all (n,m) wrapping vectors are equally probable, 1/3 of all SWNTs are expected to be metallic and 2/3 to be semiconducting. Figure 1.4 shows the energy versus momentum dispersion for a zigzag (5,5) (zigzag tubes are always metallic) and a semiconducting armchair (9,0) nanotube. For a typical nanotube diameter of d = 1.3 nm the energy gap amounts to 0.68 eV.

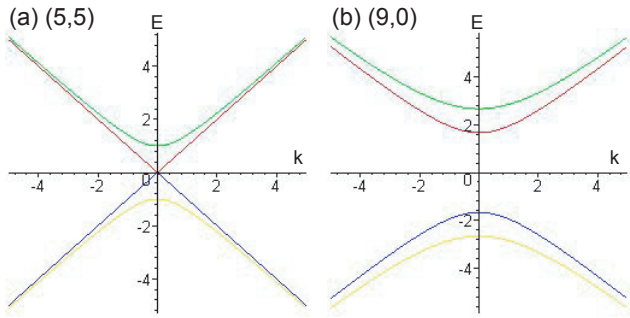

Figure 1.4: (a) Energy dispersion of a metallic (5,5) carbon nanotube. (b) Energy dispersion of a semiconducting (9,0) nanotube. Energy is plotted in units of $E_0 = \frac{2\hbar v_F}{d}$ and k in units of $k_0 = \frac{2}{d}$

.

1.2 Growth by chemical vapor deposition

There are different methods of how to produce carbon nanotubes such as laser ablation [10], arc-discharge, and chemical vapor deposition (CVD) [11]. For the early work within this thesis MWNTs obtained by an arc-discharge process have been used. The MWNTs have been synthesized at L. Forró's group at the EPFL (Lausanne). A large current of the order 100 A is passed through a graphite rod in a He atmosphere. On the graphite cathode a deposit consisting of bundles of MWNTs forms during the process. After removing the deposit, the nanotubes can be stored in chloroform and spread on a substrate. For a more detailed description of nanotube growth by arc-discharge see references [2, 12, 13].

However, using SWNTs has big advantages. First, the system is defined in a much more robust manner, second, the energy scales of SWNTs are roughly a factor ten times bigger than those of MWNTs. Hence, quantum and single-charge effects are accessible at higher temperatures. In the second part of this work experiments thus made use of SWNTs grown in-house using a CVD process. A joined effort was needed in order to finally achieve the successful growth of single (unbundled) single-walled carbon nanotubes.

The principle setup of the CVD apparatus is shown in Fig. 1.5. A substrate (Si/SiO_2) with a catalytic surface is put inside a furnace which then is heated up to 900 - 1000° C whilst maintaining a constant flow of an unreactive carrier gas (Argon). When the final temperature is reached the carrier gas is replaced by a carbon-containing gas (Methane, CH_4) providing the carbon for the formation of the carbon nanotubes. The dissociation of CH_4 is energetically favored on the catalyst surface from where the nanotubes start to form. After a growth

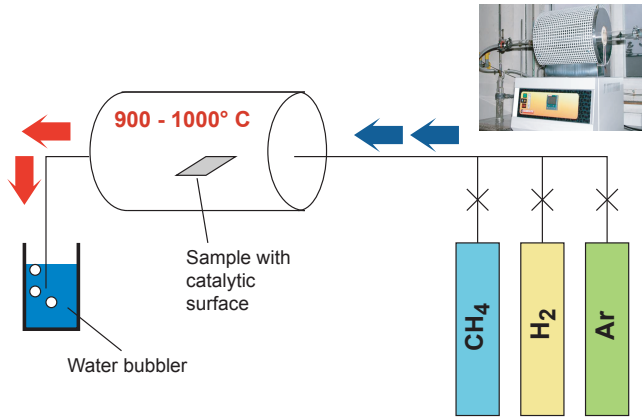

Figure 1.5: Setup of the CVD apparatus. On the top right a photograph of the actual furnace is shown.

.

time of ten minutes the methane flow is stopped while restarting the argon flow through the oven. When the furnace has cooled down sufficiently ($\approx 350°$ C) the argon flow can be stopped and the sample taken out. During the growth process we also added hydrogen to the methane which limits the formation of undesired amorphous carbon on the substrate.

The used catalyst consists of iron nitrate ($Fe(NO_3)_3$-$9H_2O$), molybdenum dioxide dichloride (MoO_2Cl_2) and alumina (Al_2O_3) following the recipe given by Ref [14]. What is the function of the individual components? A detailed description of the growth mechanisms can be found in Ref. [15], summarizing the function of the components as follows (neglecting N and Cl): Mo catalyzes the formation of radicals from the carbon feedstock CH_4 in direct contact with Fe, and the presence of Al prevents the Fe from oxidizing. The hydrogen passed through the oven during the growth process slows down the uncontrolled formation of radicals and etches amorphous carbon deposited on the substrate. The detailed recipe for growing SWNTs on Si/SiO_2 substrates can be found in the Appendix.

1.3 Making nanotube-based electrical devices

In most cases, what one wants to end up with, is a field-effect transistor setup depicted in Fig. 1.6. The carbon nanotube lies on top of a layer of SiO_2 insulating the device from the underlying doped Si substrate which is used as a back-gate electrode. The following section will be devoted to the details on how to get there.

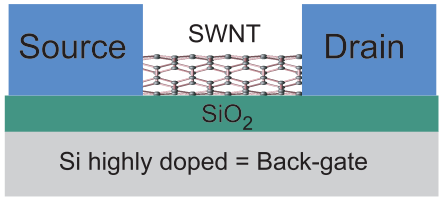

Figure 1.6: The device of interest: A carbon nanotube field effect transistor.

One starts by cleaving a Si 110 wafer covered by typically 400 nm SiO_2 into small pieces of roughly 2 cm $\times$ 2 cm. It is important to clean the substrate thoroughly, in our laboratory this is done by an ultrasonical cleaning in isopropanol for ten minutes, ten minutes cleaning in an O_3-chamber and finally by an oxygen plasma for 20 s. After completing all steps preparations for the growth of SWNTs have to be met. One droplet of the catalyst solved in isopropanol is spun onto the substrate turning at a speed of 4000 rounds per minute (rpm). Then the CVD-growth of the nanotubes is performed, see the recipe in the Appendix. Figure 1.7 (a) shows a typical SEM micrograph of the substrate after CVD-growth of carbon nanotubes.

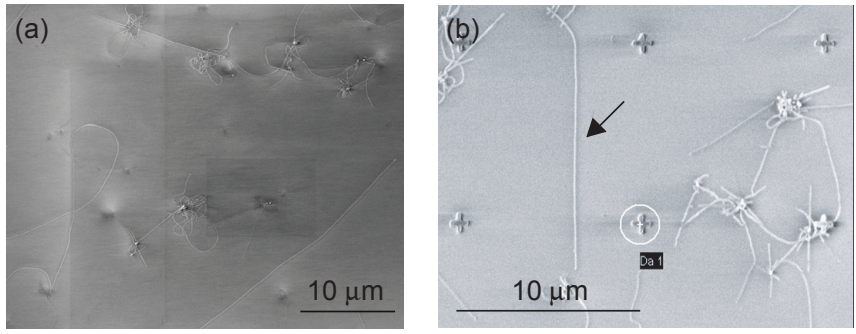

Figure 1.7: (a) Carbon nanotubes on a Si/SiO_2 substrate right after CVD-growth. (b) Nanotubes are localized by using evaporated markers spaced by 10 μm. In this case the vertically lying tube marked by the arrow was selected.

After the growth, markers (see Fig. 1.7 (b)), which are necessary to localize individual nanotubes, and large metal pads for the bond wires are fabricated by electron-beam (e-beam) lithography and electron-gun evaporation (see Fig. 1.8 (b)). For the lithography a resist sensitive to electron-beam radiation

(Polymethyl metacrylate (PMMA) diluted with chlorbenzene) is spun onto the substrate (4000 rpm) and baked at 180° C for 45 minutes. The final PMMA film thickness after baking was chosen to be around 550 nm - 600 nm. E-beam lithography is performed with a JEOL JSM-IC848 scanning electron microscope (SEM) and Proxy-Writer software by Raith. After e-beam lithography one has to develop the PMMA in an MIBK:Isopropanol 1:3 mixture for 90 s. Now the metal films can be evaporated. The substrate is built into a vacuum chamber where the metal deposition takes place at a pressure of $\approx 10^{-6}$ mbar by heating up a target with an electron beam. For the markers and bonding pads the following material layers and corresponding thicknesses are evaporated: 1. 10 nm SiO_2 (prevents from shorts due to long nanotube bundles bridging the bond-pads). 2. 10 nm Ti (Ti partly oxidizes during evaporation and thus serves as an adhesion layer for the following metal layers). 3. 70 nm Au (Au does not oxidize and is thus well-suited as top layer.) After evaporation the remaining PMMA needs to be removed by a lift-off procedure in hot (60° C) acetone.

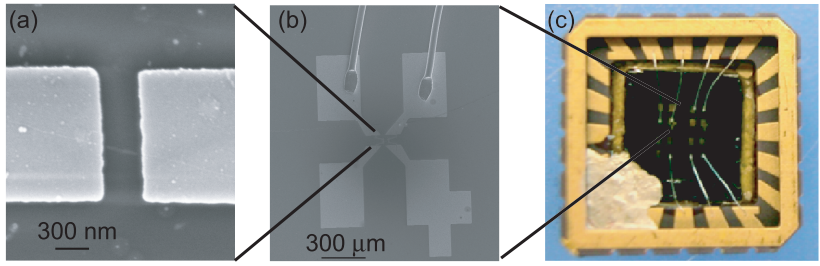

Figure 1.8: (a) Contacted carbon nanotube on chip. (b) Zoom out of (a): Bond pads and Al bond wires. (c) Zoom out of (b): Completed device in a chip carrier. The dimension of the chip carrier is roughly 1 cm × 1 cm. The silver-paint blob at the left bottom corner makes electrical contact to the Si-substrate, being used as back-gate.

Now we are able to look for the carbon nanotubes we would like to use for the electrical devices. The localization is done with an SEM (LEO SUPRA 35). It has been shown that all nanotubes that can be resolved by an atomic force microscope (AFM) can be resolved with the LEO SEM as well [15]. In addition localizing nanotubes with an SEM is much quicker than with an AFM. The position of the nanotubes one intends to contact is determined with respect to the alignment markers placed randomly on the substrate. After localizing the tubes a second e-beam lithography and metal-deposition process is needed in order to place electrodes on top of the nanotube chosen. The processing steps are identical to the lithography of the markers and bond pads, however, by using the markers the substrate has to be carefully aligned in-situ for the lithography procedure. For the deposition of the electrodes Pd has become the standard material, since Pd has good wetting properties on nanotubes. For

the experiments on MWNTs also Au and Ti/Au or Au/Al bilayers were used. Figure 1.8 (a) shows a contacted SWNT. The whole process is almost identical for both MWNTs from a solution and CVD-grown SWNTs. The only major difference is that CVD-tubes are grown before placing markers and bond pads on the Si substrate whereas the MWNTs from solution are spread after markers and bond-pads have already been patterned.

After the lift-off the substrates are glued onto a chip carrier with 20 contacts. The bond-pads on-chip are then connected to these contacts by thin Aluminum bonding wires. Care has to be taken not to damage the insulating SiO_2 layer on the chip when using a too high power during the ultrasonical bonding process. Figure 1.8 (c) shows a photograph of a completed device inside the chip carrier.

References

[1] H. Kroto *et al.*, Nature **318**, 162 (1985).

[2] S. Iijima, Nature **354**, 56 (1991).

[3] L. Zheng *et al.*, Nature Materials **3**, 673 (2004).

[4] J. Wildöer *et al.*, Nature **391**, 59 (1998).

[5] J. Mintmire, B. Dunlap, and C. White, Phys. Rev. Lett. **68**, 631 (1992).

[6] N. Hamada, S. Sawada, and A. Oshiyama, Phys. Rev. Lett. **68**, 1579 (1992).

[7] R. Saito, M. Fujita, G. Dresselhaus, and M. Dresselhaus, Appl. Phys. Lett. **60**, 2204 (1992).

[8] P. Wallace, Phys. Rev. **71**, 622 (1947).

[9] L. Forró and C. Schönenberger, Carbon Nanotubes: Synthesis, Structure, Properties, and Applications edited by M.S. Dresselhaus, G. Dresselhaus, and Ph. Avouris (Springer) 59 (2001).

[10] J. Liu *et al.*, Science **280**, 1253 (1998).

[11] H. Dai, Acc. Chem. Res. **35**, 1035 (2002).

[12] T. Ebbesen and P. Ajayan, Nature **358**, 220 (1992).

[13] J. Bonnard *et al.*, Advanced Materials **9**, 827 (1997).

[14] J. Kong *et al.*, Nature **395**, 878 (1998).

[15] J. Furer, *PhD Thesis* (unpublished, University of Basel, 2005).

Chapter 2

Charge transport in mesoscopic systems

2.1 A few remarks

In this chapter selected topics of charge transport in mesoscopic systems relevant to this thesis are reviewed. In particular, we will briefly discuss the key results of the Landauer-Büttiker formalism and interference effects with reference to experimental evidence of both. Additional important ingredients of this work are quantum dot behavior and single charge tunneling, which will be discussed in section 2.3. We then go over to the mechanisms governing electronic transport at (mesoscopic) normal-superconductor interfaces and will finish this chapter with a brief introduction to double quantum dot physics. As this chapter can only give a small flavor of the field of mesoscopic physics, the interested reader is asked to refer to, e.g. "Electronic Transport in Mesoscopic Systems" by S. Datta [1], "Mesoscopic Physics and Electronics" by T. Ando [2], and "Single Charge Tunneling - Coulomb Blockade Phenomena in Nanostructures" edited by H. Grabert and M.H. Devoret [3].

2.2 Conductance, transmission and interference

With the advent of micro- and nano-structuring fabrication techniques it has become possible to study physics in an intermediate regime between the atomic scale and the macroscopic one, the so-called mesoscopic regime. In this regime charge carriers may have a quantum-mechanically coherent history, and behave according to the particle-wave duality. Here, the de Broglie wavelength and the momentum at the Fermi energy, λ_f and k_f are related by $\lambda_f = 2\,\pi/k_f = \sqrt{2\pi\,n_s}$, with n_s being the density of electrons. Quantization effects are expected when the dimensions of the system are of the order of λ_f, resulting in a discrete energy spectrum.

In mesoscopic systems electronic transport is often described as a scattering problem, i.e. a moving electron hits a certain barrier and gets transmitted with a probability T or reflected with a probablity $1 - T$. From this picture it becomes clear that conductance through a system can be viewed as transmission of the charge carriers through it. When the scattering processes are elastic, the conductance G through a conductor (quantum wire) with M non spin-degenerate modes with transmission T can be expressed using the Landauer-Büttiker formalism as [4, 5]:

$$G = \frac{e^2}{h} \sum_i^M T_i \ , \tag{2.1}$$

where $e^2/h \approx 38\,\mu$S corresponding to the inverse of the resistance quantum $R_Q = 25.8$ kΩ. R_Q was first observed as quantized Hall resistance in the quantum Hall effect [6]. Later, conductance quantization in quantum point contacts, narrow constrictions defined inside a two-dimensional electron gas (2-DEG) were reported by van Wees et al. [7]. In metals, where k_f is much shorter, conductance quantization was observed in atomic-scale contacts accessible by STM [8] or mechanically-controllable break junction techniques [9]. Frank et al. reported a quantized conductance in an experiment in which multi-walled carbon nanotubes (MWNTs) were used as an STM tip and then lowered into liquid mercury [10]. In all these experiments the observed quantized change of conductance could be attributed to single modes entering or leaving the system.

Eq.(2.1) implies that, even in the case of a ballistic conductor perfectly attached to electron reservoirs ($T = 1$), there is a finite resistance. The voltage drop involved then occurs at the contacts and a four-point measurement of the resistance of the ballistic conductor yields zero , as was observed experimentally in Ref. [11]. For an ideal metallic nanotube, i.e. ballistic and undoped, one expects a two-terminal conductance of $G = 4\,e^2/h$, where we took into account the two degenerate bands at $\pm k_f$ (see chapter 2), each of them two-fold spin-degenerate.

The wave character of electrons in mesoscopic systems is reflected in interference effects observed in numerous experiments. Probably the most prominent is the solid-state analog of the double-slit experiment, the Aharonov-Bohm effect. In a 1985 experiment Webb et al. passed a current through a submicron-diameter Au ring and measured periodic oscillations of the conductance when varying a magnetic flux applied perpendicular to the ring [12]. These results can be interpreted as the interference between the two paths an electron can take in order to propagate through the ring. A necessary condition is that the electron path through the ring is shorter than the phase coherence length l_Φ. If this is not the case, the electron will lose its phase information in between and will not be able to interfere. Aharonov-Bohm oscillations have been observed not only in metal rings, but also in rings defined in 2-DEGs [13] and in MWNTs [14].

Other well-known interference effects in mesoscopic systems are weak localization [15] and universal conductance fluctuations (UCF) [1]. In disordered,

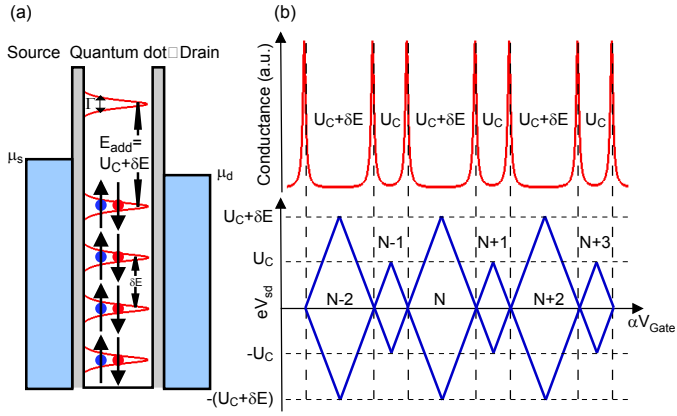

Figure 2.1: (a) Schematics of a quantum dot tunnel-coupled to metallic electrodes. (b) Conductance through a quantum dot versus gate voltage (top) and corresponding stability diagram, exhibiting so-called Coulomb diamonds (bottom).

phase-coherent samples the probability for backscattering is enhanced due to the constructive interference of such time-reversed (backscattered) trajectories. By applying a perpendicular magnetic field the enhanced backscattering is suppressed as the magnetic flux leads to a phase difference between the two backscattered paths. The enhanced backscattering at zero magnetic field is referred to as weak localization. UCF are random sample to sample fluctuations of the conductance in diffusive, phase-coherent systems. They are universal in the sense that the amplitude of the conductance fluctuations is of the order e^2/h irrespective of sample size and degree of disorder. In carbon nanotubes, both weak localization and UCF have been studied extensively [16, 17].

2.3 Quantum dots

As described above, in mesoscopic physics particles can be described as extended objects with wave character. When the wavelength of the particles becomes comparable to the system dimensions, the energy spectrum (the density of states) is modified. Such finite-size effects lead to a quantization of the wave vector in the confined direction. The system is referred to as quantum dot when the particle is confined in all spatial directions and reduces to a zero-dimensional problem, where the energy eigenvalues are quantized. The energy difference between two allowed energy eigenvalues is called level spacing or orbital energy. In fact, quantum dots are an experimental realization of the quantum-mechanics

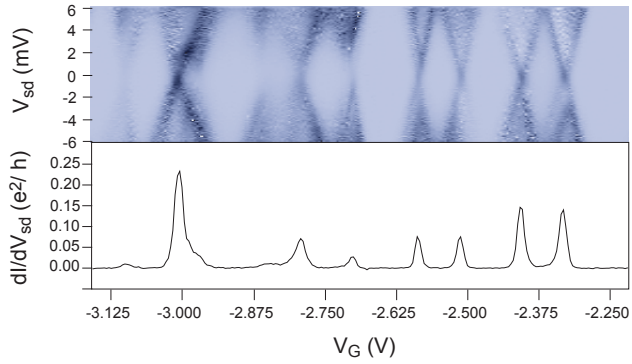

Figure 2.2: Grayscale plot of the differential conductance (dark = more conductive) and trace of the linear conductance through a SWNT at 4.2 K.

textbook example of a particle in a box. The analogy to atomic orbitals has led to the alternative name "artificial atoms" [18].

Whereas spectroscopy experiments on real atoms have mainly made use of light, attaching leads to artificial atoms provides a novel way of accessing the properties of quantum-mechanical states by means of electronic transport. In addition, due to the small size of quantum dots, another, completely classical, energy scale enters the game. This energy scale is the single-electron charging energy, also referred to as the on-site repulsion. A typical quantum dot consists of an island which is coupled to leads via tunnel barriers. Classically, a tunnel barrier can be represented simply as a capacitor with a certain capacitance C. The energy it takes to add an electron charge e on the capacitor is given by $U_C = e^2/2C$ [3, 19]. In the case of nano-structured tunnel-barriers the capacitance can become very small resulting in a significant single-electron charging energy U_C of the order 1 to a few K. In order to enable transport of electrons through the system this energy has to be provided, either by a bias voltage or by a change of the gate voltage. In the regime $k_B T < U_C$ single electron charging phenomena thus allow for the control of the number of charge carriers residing on the system.

The coupling to the attached leads is characterized by the tunneling rates Γ_S and Γ_D. As a consequence of the finite tunnel-coupling to the leads the discrete energy state gets smeared out and has a width given by the Γs. From the Heisenberg uncertainty principle $\Delta E\, \Delta t \approx h$ the life time of the state can be deduced. Figure 2.1 (a) shows the schematics of a quantum dot coupled to metallic source and drain electrodes. We assume only spin-degeneracy, i.e. each energy level can be occupied by two electrons. The orbital energy is denoted δE. If a level is occupied by only one electron, one will have to pay an addition

energy of U_C, the single-electron charging energy, for adding another electron. If, however, a level is already occupied by two electrons, the additional electron will have to be put into the next higher orbital state. The addition energy in such a case is then given by $U_C + \delta E$. With capacitively coupled gate electrodes the levels on the dot can be moved linearly, i.e. the quantum dot can be filled or emptied subsequently. How do the transport characteristics of such a system look? In the linear regime ($V_{sd} = 0$) charge carriers can tunnel through the dot when an empty state on the dot is lined up with the chemical potentials of source and drain. One thus expects a sharp resonance of conductance every time the necessary addition energy is provided by the gate voltage. Since there are different addition energies for an odd or an even occupancy of the dot one expects two different spacings in between the resonances of conductance: See the top of figure 2.1 (b).

The charge stability diagram of a quantum dot can be obtained by sweeping both the source-drain voltage and the gate voltage, see the bottom of figure 2.1 (b). The drawn lines correspond to the conditions $V_{sd} = \pm\alpha(V_G - V_{G0})$ where $\alpha = C_G/(C_S + C_D + C_G) = C_G/C_\Sigma$ is the coupling factor of the gate electrode and V_{G0} is the gate voltage position of the conductance resonance, i.e. where a dot level is aligned with the chemical potential of source and drain. Connecting the intersects of the lines results in a pattern often referred to as Coulomb diamonds. Inside each of the diamonds the quantum dot is stable against fluctuations of its charge. Sweeping the gate voltage to more positive values subsequently fills electrons on the dot whereas sweeping the gate to more negative values pushes electrons out of it. The two different addition energies result in two different sizes of diamonds. Coulomb diamonds are also present for a single-electron-transistor (SET), however, in contrast to quantum dots there are no single quantum levels involved. Thus the addition energy is constant and all Coulomb diamonds are expected to have the same size.

For a nanotube with effective length L the wave vector in the direction of the tube axis is quantized. The quantization of the wave vector leads to a quantization of the energy spectrum. In the vicinity of the Fermi level, the orbital energy δE of an ideal metallic nanotube yields $\delta E = hv_F/2L$ where the Fermi velocity $v_F = 8 \cdot 10^5$ m/s. For a typical length of 1 μm the level spacing follows to be $\delta E = 1.7$ meV which corresponds to a temperature of roughly 20 K. For SWNTs the charging energy U_C is of the same order. In MWNTs, both δE and U_C are about one order of magnitude smaller. Figure 2.2 shows the stability diagram and the linear differential conductance through a SWNT quantum dot with a contact spacing of 300 nm and $U_C \approx \delta E \approx 6$ meV measured at 4.2 K. Note, for an ideal nanotube one expects a four-fold degeneracy of the levels due to the band structure which is symmetric around $k = 0$, see Chapter 1.

The discussion on nanotube quantum dots so far has been limited to the case of Coulomb-blockaded islands. However, when $G \geq e^2/h$, single-electron charging effects become less pronounced. Instead, interference phenomena, with amplitudes depending sensitively on the transmission of barriers, take place in the nanotube wave-guide, similar to Fabry-Perot interferences in optical cavities

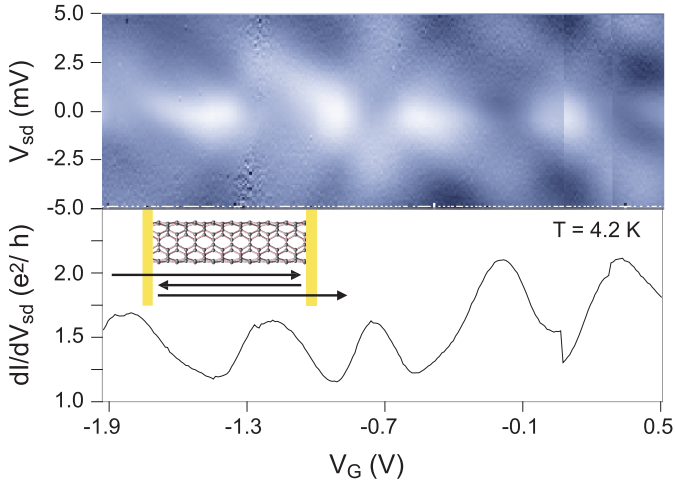

Figure 2.3: Colorscale plot of the differential conductance (dark blue = more conductive) and trace of the linear conductance through a fairly open SWNT at 4.2 K. We attribute the modulation of the conductance with gate voltage to quantum interference processes. The kink at $V_G \approx 0$ V is due to a random, occasionally occurring jump of the gate potential.

[20]. Figure 2.3 shows a colorscale plot of the differential conductance through an open nanotube device at 4.2 K. In contrast to Coulomb oscillations, the amplitude of the conductance modulations is only about 1/3 of the signal and the conductance in the valley is still greater than e^2/h. In an intermediate regime, where both, fairly transparent tunnel barriers and Coulomb blockade are present, the lead-dot system may exhibit Kondo correlations [21]. The Kondo effect and its interplay with a superconducting electrode will be the subject of Chapter 3.

2.4 Transport through a normal-superconductor junction

Chapter 3 of this thesis deals with the transport properties of a carbon nanotube coupled to a normal and a superconducting electrode. It is thus important to understand the physics governing charge transfer processes at a normal-superconducting (N-S) interface. Conventional superconductivity is explained within the framework of the so-called BCS theory [22] by a phonon-mediated attractive interaction between electrons around the Fermi edge. Due to this interaction an energy gap Δ arises in the quasiparticle density of states. Inside

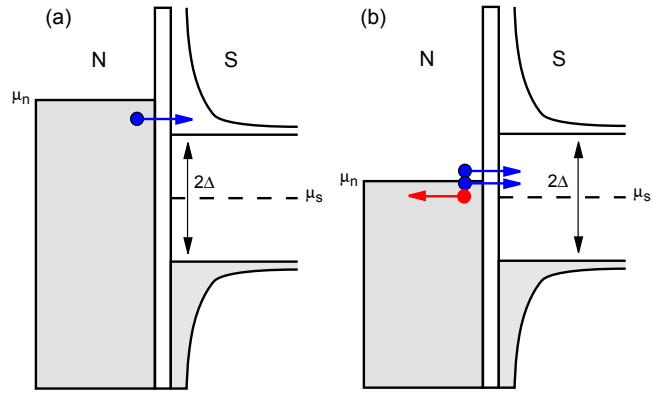

Figure 2.4: Illustration of a normal-superconducting interface at a an applied bias $\mid eV_sd \mid > \Delta$ in (a) and $\mid eV_sd \mid < \Delta$ in (b). In (b) transport at zero temperature is only carried by Andreev reflections.

the energy gap electrons condense into so-called Cooper pairs, outside the gap electrons are unpaired with a modified quasiparticle density of states $N(E)$, given by [23]:

$$\frac{N(E)}{N_0} = \begin{cases} \frac{E}{\sqrt{E^2-\Delta^2}} & |E| \geq \Delta \\ 0 & |E| < \Delta \end{cases} , \tag{2.2}$$

where N_0 is the normal density of states which can be treated as a constant around the Fermi energy.

From these first considerations it becomes clear that transport at an N-S boundary strongly depends on whether the applied bias voltage across the junction is smaller or bigger than the BCS gap. When $\mid eV_{sd} \mid > \Delta$ quasiparticle transport is possible, when $\mid eV_{sd} \mid < \Delta$ two electrons from the normal metal have to form a Cooper pair in order to enable transport. Since two electrons are involved, the probability of such a process goes with T^2 where $0 < T < 1$ is the transmission probability of a single electron through the N-S interface. The underlying processes are so-called Andreev reflections, where, in order to conserve spin and charge, in addition to the original electron, a second electron enters the superconductor and a hole is reflected back into the normal region [24]. Figure 2.4 illustrates the charge transfer processes at an N-S interface.

Electrical transport through an N-S interface characterized by a certain transmission has been described quantitatively by references [25] and [26]. Figure 2.5 shows the differential conductance dI/dV_{sd} for various values of the transmission T. In the case of low transmission values (tunnel barriers), the differential conductance directly reflects the BCS quasiparticle density of states since Andreev processes are strongly suppressed. For an increasingly transparent junction the probability of Andreev processes increases enabling transport

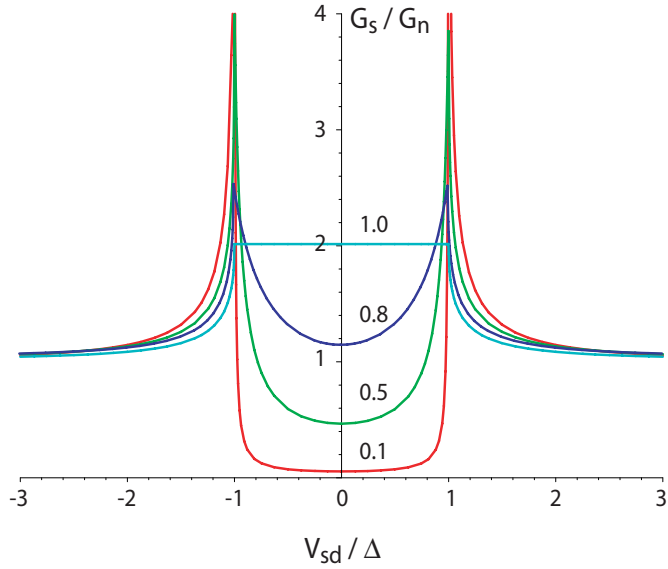

Figure 2.5: Differential conductance at zero temperature versus applied bias voltage through a normal-superconducting interface for various transmissions $T = 0.1, 0.5, 0.8, 1.0$.

within the superconducting gap. In the extreme case of $T = 1$ the differential conductance inside the superconducting gap is twice as big as that in the normal state due to the back-reflected hole originating from the Andreev process. However, keep in mind that in this picture of a normal-superconductor-junction we have neglected any energy-dependence of the barrier transmission. In mesoscopic systems, however, the wave-nature of charge-carriers and charging effects often lead to resonant transport, i.e. strongly energy-dependent transmissions. Transport through a resonant N-S-junction has been described by Khlus et al. [27], whose model will be used in Chapter 3 to analyze our data.

2.5 Double quantum dots

In section 2.3 the electrical transport properties of quantum dots, so-called artificial atoms, are discussed. Soon after the first realized single quantum dots, the idea of coupled quantum dots, so-called artificial molecules arose, and was realized, see [28] and references therein. In such structures it is possible to study the fundamentals of molecular physics. That is, probing and controlling the interaction between two artificial atoms. The interaction can be electrostatic, due to an inter-dot mutual capacitance, or quantum-mechanical, induced by a

tunnel coupling due to a finite overlap of the dot wavefunctions. In Fig. 2.6(a) a double quantum dot connected to leads and gate electrodes, controlling the individual dots, is illustrated.

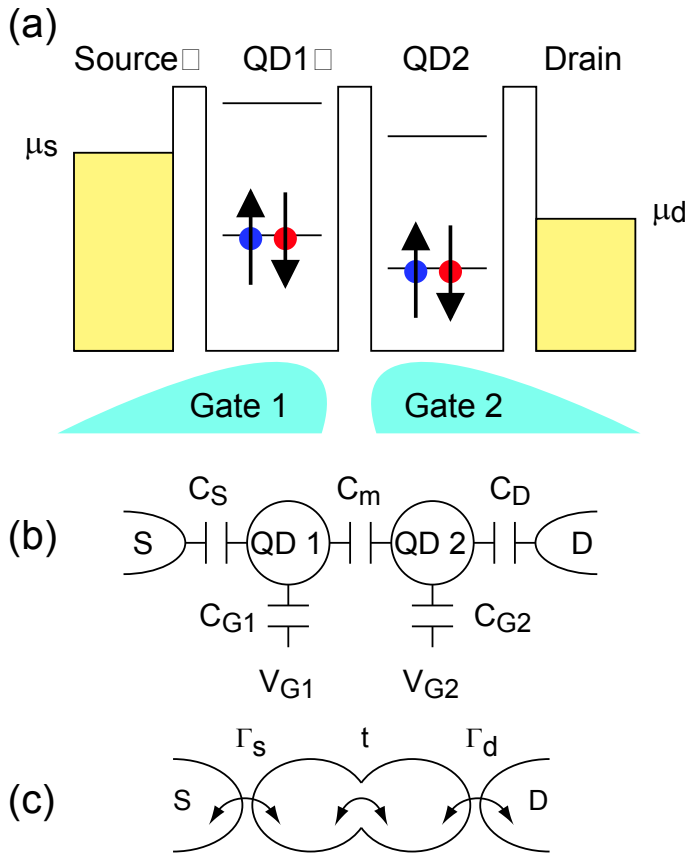

Figure 2.6: (a) Schematics of a double quantum dot connected to leads. Gates 1 and 2 control the chemical potentials of dots 1 and 2, respectively. (b) Electrostatic model of a double quantum dot. (c) Illustration of a double quantum dot with molecular states induced by a tunnel coupling t.

In order to gain an understanding of the transport properties of coupled quantum dots we will first neglect a tunnel-coupling between the dots and consider double dots with a purely electrostatic interaction, see Fig. 2.6(b). How does the charge stability diagram in terms of the gate voltages V_{G1} and V_{G2} look? Let us first assume very decoupled dots, i.e. electrical transport through one dot is independent of the other one. In order to enable transport through

one dot, the single-electron addition energy E_{add} has to be provided by the corresponding gate voltage. In order to enable transport through the whole system, this condition has to be fulfilled for the second dot as well. The charge stability diagram of the system is thus a rectangular pattern with transport allowed only at the intersection points labelled with blue in Fig. 2.7(a). Introducing a finite electrostatic interaction, the degeneracy at these points is partially lifted. Two possible charge transfer processes for, say moving an electron from the left to the right lead are:

- (n+1,m) → (n,m+1) → (n,m) → (n+1,m) or
- (n+1,m) → (n,m+1) → (n+1,m+1) → (n+1,m).

Despite the fact that both sequences start and end at the same charge configuration, their intermediate energies are non-degenerate for fixed gate voltages $V_{G1,G2}$. Due to the electrostatic nearest-neighbor interaction it actually makes a difference energetically whether the system follows the sequence to the (n,m+1) charge configuration via the (n+1,m+1) or via the (n,m) one. The resulting two points, where transport according to the two processes listed above is enabled, are referred to as triple points. The spacing between these triple points is a measure of the electrostatic nearest-neighbor interaction U', mediated by a mutual capacitance C_m. For finite U' the formerly rectangular stability diagram transforms into a hexagonal pattern, the so-called honeycomb pattern, see Fig.2.7(b).

We can now continue our previous considerations concerning the electrostatic coupling of the two dots. At some point, while continuously increasing the electrostatic coupling of the dots, the two dots will merge into a single one. Charge transport is possible when the addition energy for an electron is provided by the two gate voltages, i.e. the condition $\alpha(V_{G1} + V_{G2}) = E_{add}(N)$ needs to be fulfilled. Here N denotes the number of charges residing on the dot. This is the case at diagonal lines $V_{G1} = -V_{G2} + E_{add}(N)/\alpha$, as illustrated in Fig.2.7(c). Note that here we assumed an equal coupling α (identical gate capacitance) of the two gates, resulting in a slope of the line of -1.

Now, in order to be more quantitative, we can write down the double dot energy of the (n+1,m+1) configuration:

$$E_{n+1,m+1} = E_{n,m} + E_1 + E_2 + U' \ , \tag{2.3}$$

with $E_{n,m}$ being (up to a constant offset independent of of n,m)

$$E_{n,m} = \frac{U}{2}(n(n-1) + m(m-1)) + V_1 n + V_2 m + U' nm \ , \tag{2.4}$$

and with the energies E_1 and E_2:

$$E_1 = V_1 + Un + U'm \ , \tag{2.5}$$

$$E_2 = V_2 + Um + U'n \ . \tag{2.6}$$

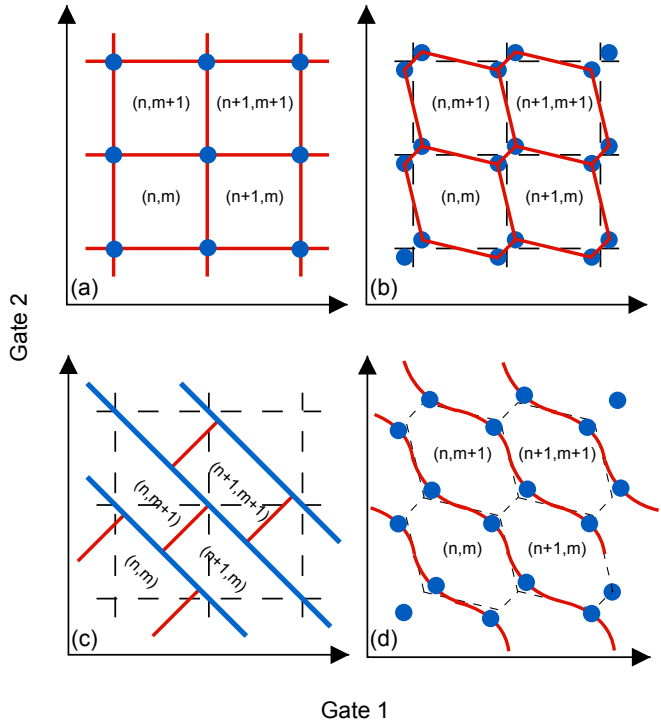

Figure 2.7: Charge stability diagram for an increasing electrostatic coupling from (a) to (c): Points / lines where transport is enabled are colored in blue, borders of stable charge regions in red. (a) Two decoupled dots. (b) Intermediate coupling: Splitting of the charge transport points. Honeycomb lattice. (c) The two dots have merged into a single dot with two gates. Charge transport is possible along diagonal lines. (d) Honeycomb pattern in the presence of a finite tunnel coupling t. The spacing of the triple points is enlarged compared to (b) and the honeycomb edges exhibit a curvature in the vicinity of the triple points. Note that transport is partly possible at these edges due to the presence of molecular states.

Here, U is the on-site repulsion of the two dots (for simplicity assumed to be identical), and V_i is the single particle energy of dot i provided by the gate voltages V_{G1} and V_{G2}.

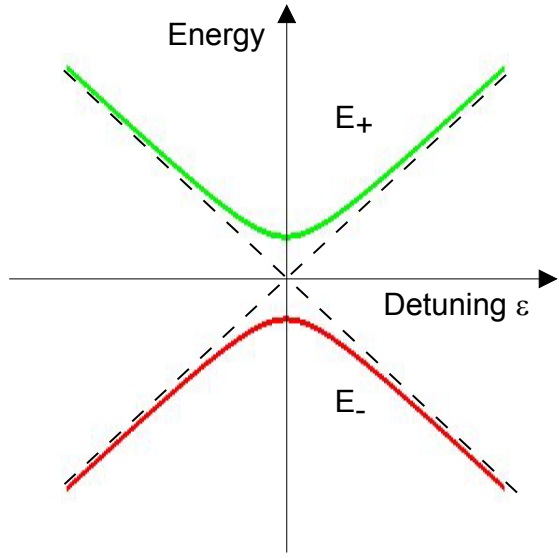

Figure 2.8: Energies E_+ and E_- versus detuning. When a tunnel coupling is absent, the two levels intersect in the origin. The perturbation induced by the tunnel coupling results in a level anti-crossing. In this plot, Δ is set to 0.

As the next step we now describe a system such as the one depicted in Fig. 2.6(c) and take into account a tunnel coupling t. First, we neglect the electrostatic nearest-neighbor interaction between the two dots. A tunnel coupling arises from an overlap of the wave functions of the two dots. In quantum mechanics such overlap of degenerate states generally results in an anti-crossing of the energy levels due to a mixing of the states. In fact, the tunnel coupling can be seen as a perturbation modifying the Hamiltonian, its eigenvalues and eigenfunctions. In order to quantify this effect we follow the description of a quantum two-level system given by Cohen-Tannoudji [29]. We start with two well-separated dots not tunnel-coupled. The eigenstates $|\phi_1\rangle$ and $|\phi_1\rangle$ of dot 1 and dot 2 then solve the Schrödinger equation with the Hamilton operator H_0 and the eigenvalues E_1 and E_2:

$$H_0|\phi_1\rangle = E_1|\phi_1\rangle \ , \tag{2.7}$$

$$H_0|\phi_2\rangle = E_2|\phi_2\rangle \ . \tag{2.8}$$

Next, the tunnel coupling can be taken into account by a hermitian matrix

T with only off-diagonal elements for the sake of simplicity.

$$\mathbf{T} = \begin{pmatrix} 0 & t_{12} \\ t_{21} & 0 \end{pmatrix} , \tag{2.9}$$

where $t_{12} = t_{21}^*$. In the $(|\phi_1\rangle, |\phi_2\rangle)$ basis the matrix of the Hamilton operator H is then given by:

$$\mathbf{H} = \mathbf{H_0} + \mathbf{T} = \begin{pmatrix} E_1 & t_{12} \\ t_{21} & E_2 \end{pmatrix} . \tag{2.10}$$

This matrix can be diagonalized and the eigenvalues are:

$$E_\pm = \frac{1}{2}(E_1 + E_2) \mp \frac{1}{2}\sqrt{(E_1 - E_2)^2 + 4 \mid t_{12} \mid^2} . \tag{2.11}$$

We can now set $\Delta = \frac{1}{\sqrt{2}}(E_1 + E_2)$, $\epsilon = \frac{1}{\sqrt{2}}(E_1 - E_2)$, $\mid t_{12} \mid^2 = t^2$ and rewrite Eq.(2.11):

$$E_\pm = \frac{1}{\sqrt{2}}(\Delta \mp \sqrt{\epsilon^2 + 2\,t^2}) . \tag{2.12}$$

E_+ is the energy of the bonding state, which is the ground state of the system. We can now plot the two energies E_+ and E_- versus the so-called detuning ϵ, which is a measure of the energy difference of the two states, see Fig. 2.8. When $\epsilon = 0$ the effect of level-repulsion reaches it maximum. The asymptotes of the unperturbed energy levels ($\mid \epsilon \mid >> 0$) intersect in the origin of the plot. The corresponding wave functions of the perturbed system $|\Psi\rangle$ with $H\,|\Psi^\pm\rangle = E_\pm\,|\Psi^\pm\rangle$ are linear superpositions of $|\phi_1\rangle$ and $|\phi_2\rangle$ and are either bonding (E_+) or anti-bonding (E_-). Consequently, a tunnel coupling leads to a delocalization of the electrons or holes trapped in a double-dot system.

In real double quantum dots one typically has both an electrostatic nearest-neighbor interaction U' and a tunnel coupling t. Both phenomena result in an increased spacing of the triple points, however only tunneling will lead to a curvature of the energy levels. For strong tunneling, the honeycomb pattern will be similar to the one sketched in Fig. 2.7(d). In particular, transport is partly enabled on the honeycomb edges, as electrons can be transferred via tunnel-coupled, molecular states $|\Psi\rangle$. An allowed charge transfer processes is then:

- $|n, m\rangle \rightarrow |\Psi\rangle = \alpha\,|n, m+1\rangle + \beta\,|n+1, m\rangle \rightarrow |n, m\rangle$

where α and β are the coefficients of the linear combination of the unperturbed, single-dot wave functions. The exact expressions for these coefficients are:

$$\mid \alpha^\pm(\epsilon) \mid^2 = \frac{2t^2}{2t^2 + (\epsilon \pm \sqrt{\epsilon^2 + 2t^2})^2} , \tag{2.13}$$

$$\mid \beta^\pm(\epsilon) \mid^2 = 1 - \mid \alpha^\pm(\epsilon) \mid^2 . \tag{2.14}$$

In Chapter 5 the measured stability diagram of a carbon nanotube double quantum dot is presented. There, the spacing of the two high-conductance wings in

the vicinity of two triple points will be used in order to precisely extract t. In the following we will thus deduce a convenient expression for the spacing of the two wings.

First, we include the lower-lying charge states on the dot and U'. The energy of the coupled state $|E_\pm\rangle$, with one excess particle relative to $|m,n\rangle$ is then given by:

$$E^{\pm}_{(\Delta,\epsilon)} = E_{n,m}(\Delta,\epsilon) + \frac{1}{\sqrt{2}}(\Delta \mp \sqrt{\epsilon^2 + 2\,t^2}) \ . \tag{2.15}$$

The energy of the state $|m+1,n+1\rangle$ follows from Eq.(2.3) to be:

$$E_{n+1,m+1}(\Delta,\epsilon) = E_{n,m}(\Delta,\epsilon) + \sqrt{2}\Delta + U' \ . \tag{2.16}$$

The two high-conductance wings one observes in the double-dot stability diagram now correspond to energy-conserving transitions from (a) the $|n+1,m+1\rangle$ state to the bonding state $|E_+\rangle$ and (b) from $|E_+\rangle$ to $|n,m\rangle$. We can now write the conditions for these transitions:

$$\mu = \frac{\Delta E}{\Delta N} = E_{n+1,m+1}(\Delta,\epsilon) - E^{+}(\Delta,\epsilon) = U' + \frac{1}{\sqrt{2}}(\Delta + \sqrt{\epsilon^2 + 2\,t^2}) \ , \tag{2.17}$$

$$\mu = \frac{\Delta E}{\Delta N} = E^{+}(\Delta + E_\Delta,\epsilon) - E_{n,m}(\Delta + E_\Delta,\epsilon) = +\frac{1}{\sqrt{2}}(\Delta + E_\Delta - \sqrt{\epsilon^2 + 2\,t^2}) \ . \tag{2.18}$$

By setting Eq.(2.17) and Eq.(2.18) equal we can now determine the spacing in the Δ-direction, E_Δ, of the two wings:

$$E_\Delta = \sqrt{2}U' + \sqrt{4\epsilon^2 + 8t^2} \ . \tag{2.19}$$

Additionally, in Chapter 5 we will make use of the fact that the differential conductance along the wings is proportional to $|\ \alpha\beta\ |^2$. With the help of Eq.(2.13) we are then able to directly extract the coefficients of the superposed wavefunction and map it.

References

[1] S. Datta, *Electronic Transport in Mesoscopic Systems* (Cambridge University Press, Cambridge, 1995).

[2] T. Ando *et al.*, *Mesoscopic Physics and Electronics* (Springer, Berlin, 1998).

[3] H. Grabert and M. D. (Editors), *Single Charge Tunneling* (Plenum Press, New York, New York, 1992).

[4] R. Landauer, IBM J. Res. Dev. **1**, 223 (1957).

[5] M. Büttiker, Phys. Rev. Lett. **57**, 1761 (1986).

[6] K. v. Klitzing, G. Dorda, and M. Pepper, Phys. Rev. Lett. **45**, 494 (1980).

[7] B. van Wees *et al.*, Phys. Rev. B **38**, 3625 (1988).

[8] J. Gimzewski and R. Möller, Phys. Rev. B **36**, 1284 (1987).

[9] C. Muller, J. van Ruitenbeek, and L. de Jongh, Phys. Rev. Lett. **69**, 140 (1992).

[10] S. Frank, P. Poncharal, Z. Wang, and W. de Heer, Science **280**, 1744 (1998).

[11] R. de Picciotto *et al.*, Nature **411**, 51 (2001).

[12] R. Webb, S. Washburn, C. Umbach, and R. Laibowitz, Phys. Rev. Lett. **54**, 2696 (1985).

[13] W. van der Wiel *et al.*, Science **289**, 2105 (2000).

[14] A. Bachthold *et al.*, Nature **397**, 673 (1999).

[15] G. Bergmann, Phys. Rep. **107**, 1 (1984).

[16] C. Schönenberger, A. Bachthold, J.-P. Salvetat, and L. Forró, Appl. Phys. A **69**, 283 (1999).

[17] M. Buitelaar, *PhD Thesis* (unpublished, University of Basel, 2002).

[18] M. Kastner, Physics Today **46**, 24 (1993).

[19] L. Kouwenhoven *et al.*, Proceedings of the Advanced Study Institute on Mesoscopic Electron Transport, edited by L.L. Sohn, L.P. Kouwenhoven, G. Schön (Kluwer). (1997).

[20] W. Liang *et al.*, Nature **411**, 665 (2001).

[21] L. Kouwenhoven and L. Glazman, Phys. World **14**, 33 (2001).

[22] J. Bardeen, L. Cooper, and J. Schrieffer, Phys. Rev. **108**, 1175 (1957).

[23] M. Tinkham, *Introduction to Superconductivity* (McGraw-Hill, New York, 1996).

[24] A. Andreev, Sov. Phys. JETP **19**, 1228 (1964).

[25] G. Blonder, M. Tinkham, and T. Klapwijk, Phys. Rev. B **25**, 4515 (1982).

[26] J. Cuevas, A. Martín-Rodero, and A. Yeyati, Phys. Rev. B **54**, 7366 (1996).

[27] V. Khlus, A. Dyomin, and A. Zazunov, Physica C **214**, 413 (1993).

[28] W. van der Wiel *et al.*, Rev. Mod. Phys. **75**, (2003).

[29] C. Cohen-Tannoudji, B. Diu, and F. Laloë, *Quantum Mechanics* (de Gruyter, Berlin, New York, 1997).

Chapter 3

Quantum dot coupled to a normal and a superconducting lead

3.1 Motivation

In Chapter 2 we have seen that, at low temperatures, carbon nanotubes can act as quantum dots. Different transport regimes, depending on the transparency of the contacts, such as Coulomb blockade and Kondo effect have been realized [1, 2]. Recently it has also been possible to couple a carbon nanotube quantum dot in the Kondo regime to superconducting leads, demonstrating a rich interplay of these two many particle phenomena [3]. In this chapter we consider a slightly different geometry, namely a quantum dot connected to both a normal and a superconducting lead. These hybrid systems are interesting for two reasons. First, the interplay of the Kondo effect and superconductivity can be examined on a different basis. Various predictions have been made for this scenario, e.g. suppression or enhancement of the conductance [4], side-peaks in the density of states at the position of the superconducting gap [5] and excess Kondo resonances [6]. Second, the structure mentioned above is the basic building block of proposed Andreev entanglers making use of either the 0-dimensional quantum dot charging energy U_C [7] or the 1-dimensional Luttinger repulsion energy of a nanotube in order to spatially separate pairs of entangled electrons [8, 9, 10]. In the following we will focus on the interplay of the Kondo effect and the superconducting lead.

3.2 Sample fabrication and measurement

The device we consider consists of a multi-walled carbon nanotube (MWNT) coupled to a normal metal on one side and to a superconductor on the other.

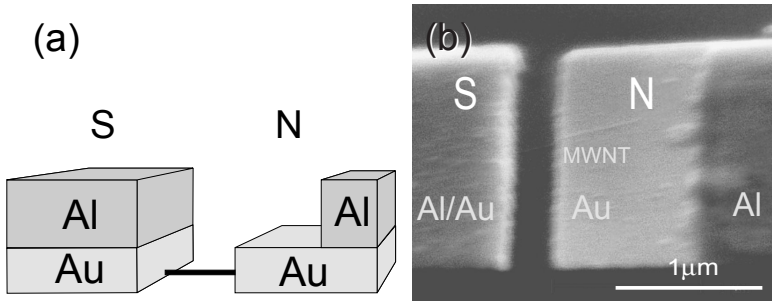

Figure 3.1: (a) Schematics of the device. (b) SEM micrograph of the sample.

The sample preparation involves the following steps. First MWNTs are spread on a degenerately doped silicon substrate, in the experiment serving as a back-gate, which is covered by a 400 nm thick insulating layer of SiO_2. Single nanotubes are then contacted by means of electron-beam-lithography and e-gun-evaporation, see Chapter 1. Similar to reference [3] the superconducting contact is a 45 nm Au/ 160 nm Al proximity bilayer. However, by using tilt-angle-evaporation for the Al layer one obtains a structure such as the one sketched in Fig. 3.1(a). Whereas the left-hand side of the MWNT is coupled to the superconducting Au/Al bilayer, the right-hand electrode is formed simply by the 45 nm gold layer. There will also be Al deposited on this side, but the spatial separation of the nanotube-gold-contact and the Al film is fairly long (approximately 1 μm). To check quantitatively whether also on this side of the sample proximity effects have to be taken into account one can estimate the Thoules energy [11]. The Thoules energy represents an upper limit in energy for observing superconducting correlations (assuming perfect barriers). One obtains $E_T = \hbar D/L^2 \approx 3\,\mu\text{eV} \approx 10\,\text{mK}$ using a gold diffusion constant $D = 5 \times 10^{-3}$ m^2/s (corresponding to an estimated Au mean free path of 10 nm) and a spatial separation $L \approx 1$ μm. The experiment is performed at 90 mK, hence, kT is bigger than the estimated E_T and any proximity induced superconductivity on the right sample contact can be safely neglected. Consequently the sample geometry represents a S-QD-N structure. Figure 3.1(b) shows an SEM (Scanning Electron Microscope) micrograph of the sample. Electrical transport measurements were performed in a Kelvinox dilution refrigerator.

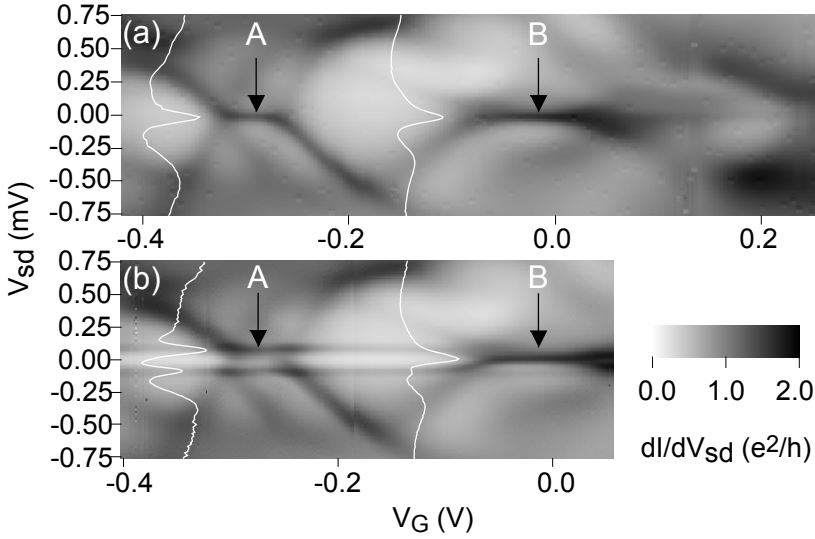

Figure 3.2: (a) Grayscale representation of the normal state conductance at 90 mK and B = 25 mT (dark = more conductive). The white curve on the left (right) shows the differential conductance versus the applied source-drain voltage at the position of the left (right) arrow. The two Kondo ridges are labelled "A" and "B". (b) Grayscale representation of the conductance in the superconducting state at 90 mK and B = 0 mT.

3.3 Kondo regime

By applying a small perpendicular magnetic field of 25 mT the superconducting electrode is driven into the normal state and the sample can be characterized in the N-QD-N configuration. This is possible because the magnetic field is bigger than the Aluminum critical field but still small in terms of the Zeeman shift of the nanotube energy levels ($E_{Zeeman} = g\mu_B B$ where g ≈ 2 is the gyromagnetic ratio and μ_B the Bohr magneton). Figure 3.2(a) shows a grayscale representation of the differential conductance through the device at $T = 90$ mK and $B = 25$ mT with varying back-gate and source-drain voltage. Despite some degree of disorder clear signs of Coulomb blockade diamonds and the Kondo effect as manifest in the high conductance ridges at zero bias voltage labelled "A" and "B" are visible. From the size of the diamonds one can deduce a charging energy $U_C = e^2/2C \approx 0.3$ meV and a level spacing energy $\Delta E \approx 0.3$ meV. The coupling C/C_{Gate} is of order 250. The Kondo effect occurs when the number of electrons on the dot is odd and it thus acts as a localized magnetic moment

with spin 1/2. Below the Kondo temperature T_K the spins of the leads try to screen the localized spin, i.e. change its spin expectation value to zero. In quantum dots this happens via fast spin-flip processes allowed only on a short timescale within the Heisenberg uncertainty principle. As a result of these processes between each lead and the dot a resonance of the dot spectral density at the chemical potential of the lead occurs which finally also causes a resonance of the conductance at zero bias. In the so-called unitary limit, corresponding to $T << T_K$ [12], a perfectly transmitting transport channel opens up and the many-particle phenomenon Kondo effect reduces effectively to a completely non-interacting problem [13].

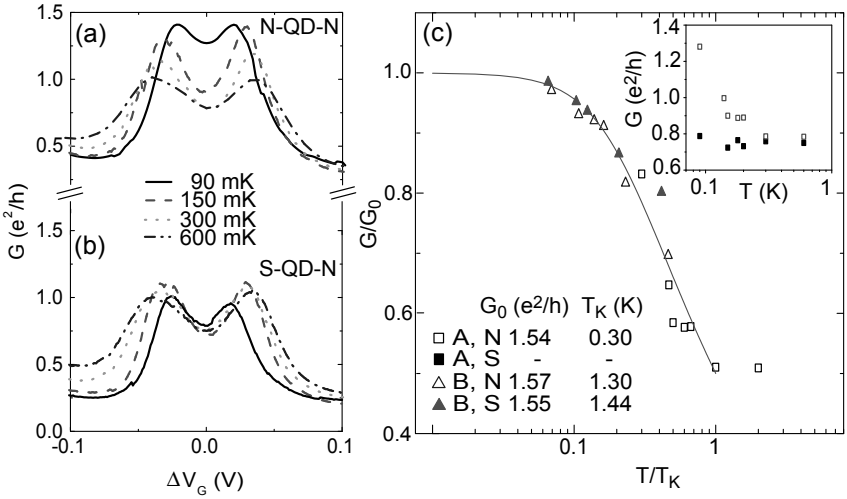

Figure 3.3: (a) Linear response conduction of ridge "A" for different temperatures in the normal state (B = 25 mT). Labels indicate the temperature in mK. (b) Like (a), but in the superconducting state (B = 0 mT). (c) Scaling plot of the maximum Kondo conductance for ridge "A" and "B" in the normal and ridge "B" in the superconducting state. The inset shows the temperature dependence of the conductance at the center of ridge "A" in the normal (upper data) and superconducting (lower data) state.

Figure 3.3(a) shows the gate dependence of the linear conductance of ridge "A" for various temperatures in the normal state. T_K can be determined by examining the temperature dependence of the linear conductance $G(T)$ on the Kondo ridge, i.e. exactly in the middle of the two adjacent Coulomb peaks. As for the 'classical' Kondo effect one finds a logarithmic temperature dependence. In order to determine T_K we used the empirical relation $G(T) = G_0/(1+(2^{1/s}-1)(T/T_K)^2)^s$ where s=0.22 for a spin 1/2 system and the maximum conductance $G_0 = 2\,e^2/h$ in the case of symmetric coupling [14]. Best fits to our data yield

$T_{K,A} = 0.3$ K, $T_{K,B} = 1.3$ K, $G_{0,A} = 1.54\, e^2/h$ and $G_{0,B} = 1.57\, e^2/h$. When plotting the normalized conductance G/G_0 over the reduced temperature T/T_K the normal state data of ridges "A" and "B" collapse on a universal locus, as seen in Fig. 3.3(c). A further rough estimate of the Kondo temperature is obtained by the width of the resonant conductance peak yielding 0.6 meV (≈ 0.72 K) and 0.1 meV (≈ 1.2 K) for ridges "A" and "B", respectively.

When one of the two electrodes enters the superconducting state the Kondo effect is modified. As was shown in [3] the Kondo effect is suppressed by superconductivity only when the superconducting gap Δ is bigger than $k_B T_K$. A crossover is expected for $\Delta \approx k_B T_K$. However, in contrast to an S-QD-S geometry here one faces an asymmetric situation and one has to distinguish the nature of coupling between the dot and the normal lead on one side and between the dot and the superconducting lead on the other. Whereas the Kondo processes between the normal lead and dot remain unaffected, two different scenarios are possible for the superconducting lead-dot-coupling. In the first case, when $k_B T_K$ is bigger than Δ one expects the Kondo resonance to persist since quasiparticle states in the superconducting electrode can participate in the Kondo spin-flip processes. If, however, $k_B T_K$ is smaller than Δ these states will be missing and the Kondo coupling between the dot and the superconducting lead will be strongly suppressed. Yet, a resonance of the dot spectral density with a renormalized Kondo temperature (Kondo resonance width) $T_K^* < T_K$ remains, which is caused by the Kondo processes between the normal lead and the dot. Whether one actually sees an enhancement of zero-bias conductance at temperatures below T_K^* will now depend on the relevant dot energy scales such as the charging energy U_C (suppresses Andreev reflections at the dot-superconductor interface) and the coupling strength on both sides Γ_S and Γ_N. In certain parameter regimes it thus should also be possible to enhance the conductance up to $4\, e^2/h$, which is the maximum value for a single perfectly-transmitting channel [15].

Figure 3.2(b) shows the conductance through our device in a grayscale representation for the superconducting state at T = 90 mK and B = 0 mT. The magnitude of the superconducting gap can be deduced from the horizontal feature at $eV_{sd} = \Delta \approx 0.09$ meV in good agreement with [3], yielding a transition temperature $T_C \approx 1$ K. For the energy scales of our quantum dot we thus obtain $\Delta E \approx U_C \approx 3\Delta$. We now focus on the two Kondo regions in the superconducting case. In the case of ridge "B" with the width of the Kondo resonance being bigger than the superconducting gap ($k_B T_K/\Delta \approx 1.3$) both the grayscale representation of the Kondo conductance and its temperature dependence remain almost identical to the normal state, i.e. a strong zero-bias conductance resonance and a logarithmic temperature dependence at low temperatures. However, for temperatures approaching the transition temperature T_C the conductance in the S-QD-N case is slightly higher than in the N-QD-N case, similar to what one would expect for a channel with constant transmission in the BTK model [16]. When fitting the temperature dependence with the same formula as above one obtains a slightly enhanced Kondo temperature of $T_K = 1.44$ K and a slightly reduced maximum conductance of $G_0 = 1.55\, e^2/h$.

For this fit we only considered temperatures sufficiently below T_C in order to exclude the BTK-like conductance enhancement mentioned above. The data also collapse on the universal Kondo locus, see Fig. 3.3(c).

The resonance of ridge "B" remains in the superconducting state, but its conductance is not increased. At first sight this behavior seems surprising, since resonances indicate a high effective transmission for which a doubling in conductance is expected in the unitary limit. This, however, only holds for a symmetrically coupled junction. Our observation is in quantitative agreement with the theoretically expected conductance if we account for the asymmetry. We consider the unitary limit for which the results for non-interacting electrons should hold. The maximum conductance (at resonance) of a transport channel between two normal electrodes is given by

$$G_{NN} = (2\,e^2/h)\,\frac{4\Gamma_L\Gamma_R}{(\Gamma_L+\Gamma_R)^2}\,. \tag{3.1}$$

From our data we obtain $G_0 = 1.57\ e^2/h$ and thus a relative asymmetry of the lead coupling of $\Gamma_L/\Gamma_R = 0.37$ (or the inverse). Between a normal and a superconducting lead the maximum Andreev conductance follows this expression derived by Beenakker [15]:

$$G_{NS} = (4\,e^2/h)\,(\frac{2\Gamma_N\Gamma_S}{(\Gamma_N^2+\Gamma_S^2)})^2\,. \tag{3.2}$$

Using the Γ-ratio determined before one obtains for the resonance conductance in the superconducting state $G_0 = 1.69\ e^2/h$. This value is only slightly higher than the one in the normal state and therefore explains our experimental observation.

In the case of ridge "A" the scenario is different ($k_B T_K/\Delta \approx 0.3$). The superconducting electrode results in a suppression of the zero bias Kondo conductance enhancement but high conducting side ridges at the position of the gap occur. This can be understood when taking a look at Fig. 3.4 where the electronic spectrum of the quantum dot and of the leads is depicted. The remaining Kondo coupling between the normal lead and the dot results in a resonance of the dot spectral density pinned to the normal lead chemical potential μ_N. At a bias of $V_{sd} = \Delta/e$ the superconductor quasiparticle spectrum and the normal lead chemical potential (and thus the Kondo resonant level) are lined up and resonant transport occurs. The linear conduction of ridge "A" in the superconducting state versus gate voltage is shown for various temperatures in Fig. 3.3(b). In the inset of Fig. 3.3(c) the conductance at the center of ridge "A" is plotted versus temperature for both the normal and the superconducting state. Whereas there is an increase of conductance below $T_K \approx 0.3$ K for the normal state data, the conductance remains more or less constant in the superconducting case. Thus we were not able to perform a fit in order to determine the renormalized Kondo temperature T_K^*. However, we suspect T_K^* to be of the order of 100 mK since the 90 mK data show an increase of conductance. The temperature dependence of the conductance on the Δ-side-peaks (data not

shown) does not show logarithmic behavior down to our lowest temperatures either, but similar to the linear response conductance an enhancement for the 90 mK data. This might indicate Kondo coupling at non-zero bias between the quasiparticles in the superconducting and the normal lead.

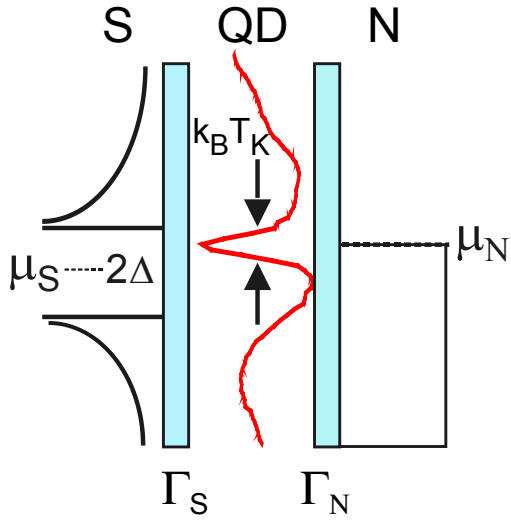

Figure 3.4: Simplified schematics of a quantum dot coupled to a normal and a superconducting lead in the Kondo regime. When $\Delta > k_B T_K$ the Kondo resonance remains pinned to the normal lead chemical potential μ_N.

3.4 Modelling the data

The I-V characteristics of a normal-superconductor interface are usually well described within the so-called BTK model as proposed by Blonder, Tinkham and Klapwijk [16]. This model treats the transport through an N-S interface by solving the Bogoliubov equations, see e.g. Ref. [17], for a δ-shaped interface potential with an arbitrary transmission. However, this model assumes an energy-independent transmission coefficient and is thus not applicable to describe transport through highly-resonant systems such as quantum dots. In the following we compare our data with two simple pictures: On the one hand a model of resonant tunneling through an N-S interface and on the other a tunneling model taking into account quasiparticle transport only.

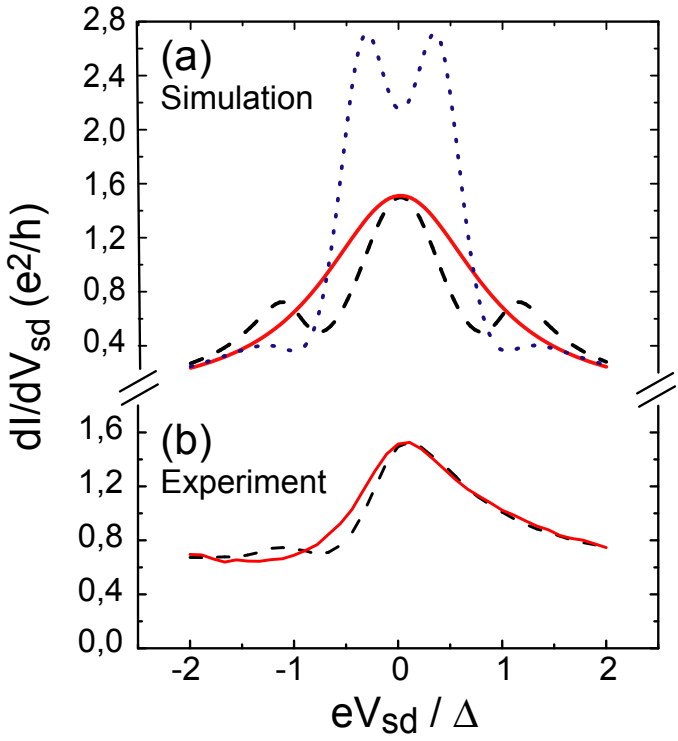

Figure 3.5: (a) Resonant tunneling through an S-N interface: Calculated differential conductance versus source-drain voltage at $k_BT = 0.1\Delta$. The solid curve represents the normal state with $\Gamma_{L/R} = 0.60$ and $\Gamma_{R/L} = 0.37{*}0.6 = 0.22$. The dashed (dotted) curve corresponds to the superconducting state and $\Gamma_{S(N)} = 0.22$ and $\Gamma_{N(S)} = 0.6$. (b) Measured differential conductance at T = 90 mK in the normal (solid line) and superconducting (dashed line) state at the center of Kondo ridge "B".

Resonant tunneling through an SN interface

In the case of $k_B T_K > \Delta$ we were able to determine the coupling asymmetry of the nanotube quantum dot by using the model of a non-interacting resonant level in the linear regime. Quite remarkably, extending the SN resonant picture to finite bias allows us to determine not only the asymmetry of the two couplings Γ_S and Γ_N but also which one of the two dominates. In order to do so we follow the approach to resonant tunneling in a normal metal-superconductor interface as given by Khlus et al. [18]. Similar to the BTK-model the Bogoliubov equations are solved by matching the wave functions in the normal and the superconducting region. However, in addition, localized states inside the barrier are taken into account by implementing an energy-dependent transmission coefficient T_{res} given by:

$$T_{res} = \frac{4\Gamma_R\Gamma_L}{(E-E_0)^2 + (\Gamma_R+\Gamma_L)^2} \; . \tag{3.3}$$

Here E_0 denotes the energy of the level and Γ_R and Γ_L the coupling energies to the right and the left lead, respectively. The conductance for transport through a single level then turns out to be:

$$G(V) = \frac{2e^2}{h}\int_{-\infty}^{+\infty} dE\; (-\frac{\partial f(E-V)}{\partial E})[2A(E)+T(E)] \; . \tag{3.4}$$

Here $f(E)$ denotes the Fermi function and $A(E)$ and $T(E)$ the probabilities for Andreev and quasiparticle contribution to the current, respectively. These probabilities are given by:

$$A(E) = \frac{16u^2v^2(\Gamma_S\Gamma_N)^2}{W(E)} \; . \tag{3.5}$$

$$T(E) = C(E) + D(E) \; . \tag{3.6}$$

$$C(E) = 4\Gamma_R\Gamma_L \frac{u(E)(u(E)-v(E))[(E+E_0)^2 + (\Gamma_N+\Gamma_S)^2]}{W(E)} \; . \tag{3.7}$$

$$D(E) = 4\Gamma_R\Gamma_L \frac{v(E)(u(E)-v(E))[(E+E_0)^2 + (\Gamma_S-\Gamma_N)^2]}{W(E)} \; . \tag{3.8}$$

$$u^2(E) = \begin{cases} \frac{1}{2}(1+\frac{\sqrt{E^2-\Delta^2}}{|E|}) & |E| \geq \Delta \\ \frac{1}{2}(1+i\frac{\sqrt{E^2-\Delta^2}}{|E|}) & |E| < \Delta \; . \end{cases} \tag{3.9}$$

$$v^2(E) = \begin{cases} \frac{1}{2}(1-\frac{\sqrt{E^2-\Delta^2}}{|E|}) & |E| \geq \Delta \\ \frac{1}{2}(1-i\frac{\sqrt{E^2-\Delta^2}}{|E|}) & |E| < \Delta \; . \end{cases} \tag{3.10}$$

$$W(E) = |u(E)(E - E_0 + i(\Gamma_S + \Gamma_N))(E + E_0 + i(\Gamma_S + \Gamma_N)) - v(E)(E - E_0 - i(\Gamma_S - \Gamma_N))(E + E_0 - i(\Gamma_S - \Gamma_N))|^2 \,. \quad (3.11)$$

In the limiting case of very low temperatures and low voltages only Andreev processes carry current. From Eq.(3.4) one can then read the linear conductance to be $2A(0)$. In this limit one recovers Eq.(3.2). In the following we set $E_0 = 0$ assuming the Kondo resonance is pinned to the normal lead chemical potential.

Figure 3.5(a) shows the results of the simulation where finite temperature is taken into account by setting $k_B T = 0.1\,\Delta$. The solid line represents the normal state conductance resonance for $\Gamma_{L/R} = 0.60$ and $\Gamma_{R/L} = 0.37 \times 0.60 = 0.22$ as obtained from the asymmetry and a rough match of the peak width. The dotted curve represents the resonance in the superconducting state with a stronger coupling to the superconductor, i.e. $\Gamma_S = 0.60$ and $\Gamma_N = 0.22$. In this case the simulation data show two pronounced conductance resonances at $V_{sd} \approx \pm\Delta/2e$ with a maximum conductance of approximately $2.7\ e^2/h$. The features are smeared out by finite temperature, hence resulting in a linear conductance bigger than the zero-temperature limit $G = 1.69\, e^2/h$, depending only on the relative asymmetry. The dashed line shows the second possible scenario in which the normal lead has a stronger coupling to the quantum dot, thus $\Gamma_N = 0.60$ and $\Gamma_S = 0.22$. Here the maximum conductance of order $1.6\ e^2/h$ is reached in the linear-response regime, while additional structures occur at the position of the gap. Let us now compare the simulation to the experimental data. Figure 3.5(b) shows the measured differential conductance of ridge "B" at 90 mK plotted versus the applied source-drain voltage for the normal (solid line) and superconducting (dashed line) case. Indeed the calculated conductance assuming a bigger coupling to the normal conductor and the measured conductance agree quite well. Both peak height and the feature at $V_{sd} = -\Delta/e$ can be reproduced. The corresponding feature for positive source-drain voltages, though, is washed out by the asymmetric shape of the measured Kondo resonance. Yet we are able to conclude that for our sample the normal lead exhibits a better coupling to the dot than the superconducting lead with an asymmetry of $\Gamma_S \approx 0.37\,\Gamma_N$.

Tunneling model

The behavior of ridge "A" can find a simple explanation by assuming a strong suppression of the Kondo coupling between the dot and the superconducting lead lowering the effective transmission T_{eff} of this interface to values comparable to tunnel barriers. The current through our device in the superconducting state is then given by [17]:

$$I = 2e/hT_{eff} \int_{-\infty}^{\infty} N_{Dot}(E) N_S(E + eV)(f(E) - f(E + eV))dE \quad (3.12)$$

with $N_S(E)$ being the BCS density of states in the superconducting lead, $N_{Dot}(E) = Re(iw(E+iw)^{-1})$ the QD local density of states of the resonant level with width

w, $f(E)$ the Fermi function and $T_S << 1$ the transmission of the barrier. Similar to [19] we included a broadening γ of the BCS density of states which we attribute to the additional Au layer separating tube and Al layer. In Fig. 3.6 we plot the conductance of ridge "A" in the superconducting state normalized by that in the normal state from both our experimental data and simulations. Best agreements are obtained with $w = 0.3\,\Delta$, $T_{eff} = 0.15$ and $\gamma = 0.05\,\Delta$. Finite temperature is taken into account by setting $k_B T = 0.1\Delta$. In the normal state we approximated the Kondo conductance peak as a Lorentzian. Comparison with our experimental data yields for the width of the Lorentzian $0.6\,\Delta$, a maximum conductance of $1.35\,e^2/h$ and a background conductance of $0.75\,e^2/h$. The proposed model clearly reproduces the main features of the experimental data, however a precise quantitative agreement remains difficult. A possible explanation of e.g. the bigger width of the Δ-peaks is an energy-dependent transmission matrix element (which we assumed to be constant) of increasing magnitude as the applied bias approaches Δ/e due to Kondo coupling between the normal lead, the dot and the superconducting quasiparticles.

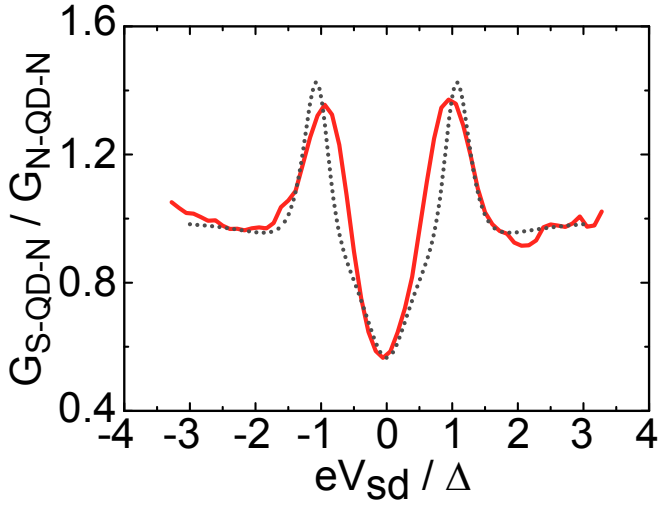

Figure 3.6: Solid line: Superconducting conductance of ridge "A" versus source-drain voltage at 90 mK normalized by the normal state conductance. Dashed line: Simulation using the tunneling model with the parameters given in the text.

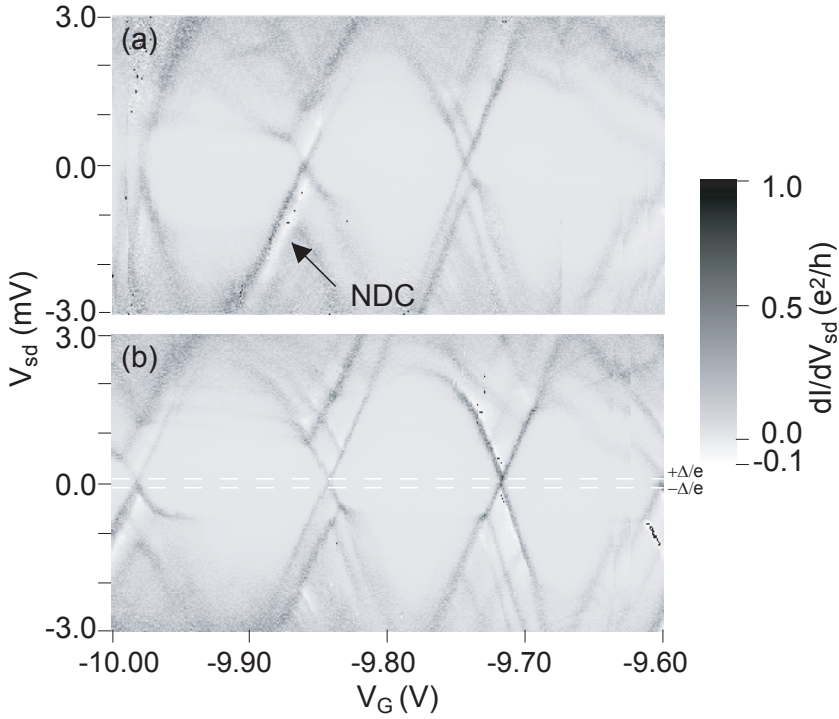

Figure 3.7: (a) Grayscale representation of the differential conductance in the low-transparent regime at T = 90 mk and B = 25 mT in the normal state. (b) Same as a) but in the superconducting state with B = 0 mT.

3.5 Coulomb blockade regime

When changing the back-gate electrode to a lower potential the sample exhibits a low-transparent Coulomb blockade behavior. Figure 3.7 shows the differential linear conductance through the device in a grayscale representation in the normal state at a temperature of 90 mK and a magnetic field of 25 mT. There is a striking difference when comparing the data with that from the Kondo regime. The energy scale of the diamond structures is of the order 3 meV, i.e. about a factor 10 bigger. We thus conclude that this is rather a different quantum dot than the same dot in a different regime. Possible explanations are either inner shells of the MWNT or a quantum dot defined by impurities inside the nanotube. The occurrence of lines of negative differential conductance (NDC) at the borders of the Coulomb diamonds suggests spin effects, possibly in a serial multi-dot structure. Figure 3.7(b) shows the differential conductance in the superconducting state. A barely visible feature at the position of the superconducting gap Δ can be seen. However, as expected from the fact that $U_C >> \Delta$ Andreev processes are suppressed strongly.

3.6 Summary

In this chapter we studied a carbon nanotube quantum dot in the Kondo regime coupled to a superconducting and a normal lead. In the case of $k_B T_K < \Delta$ the Kondo ridge at zero bias disappears and peaks at the position of the gap occur. For this scenario we proposed a simple tunnelling model explaining all significant features of the conductance curves. In the case $k_B T_K > \Delta$ the Kondo resonance persists but does not show an enhancement of the conductance compared to the normal state at the lowest temperatures accessible in our experiment. This behavior could be explained within a model of resonant transport at an SN-interface [18]. Future experiments will have to

(a) clarify whether the Kondo resonance can actually be enhanced in presence of the superconducting electrode by tuning the coupling asymmetry Γ_S/Γ_N and

(b) explore the possibility of generating pairs of entangled electrons by making use of nanotubes coupled to normal and superconducting leads [8, 9, 10].

References

[1] J. Nygard, H. Cobden, and P. Lindelof, Nature **408**, 342 (2000).

[2] M. Buitelaar *et al.*, Phys. Rev. Lett. **88**, 156801 (2002).

[3] M. Buitelaar, T. Nussbaumer, and C. Schönenberger, Phys. Rev. Lett. **89**, 256801 (2002).

[4] J. Cuevas, A. L. Yeyati, and A. Martín-Rodero, Phys. Rev. B **63**, 094515 (2001).

[5] A. Clerk, V. Ambegaokar, and S. Hershfield, Phys. Rev. B **61**, 3555 (2000).

[6] Q. Sun, H. Guo, and T. Lin, Phys. Rev. Lett. **87**, 176601 (2001).

[7] P. Recher and D. Loss, Phys. Rev. B **63**, 165314 (2001).

[8] P. Recher and D. Loss, Phys. Rev. B **65**, 165327 (2002).

[9] C. Bena, S. Vishveshwara, L. Balents, and M. Fisher, Phys. Rev. Lett. **89**, 037901 (2002).

[10] V. Bouchiat *et al.*, Nanotechnology **14**, 77 (2003).

[11] S. Guéron *et al.*, Phys. Rev. Lett. **77**, 3025 (1996).

[12] W. van der Wiel *et al.*, Science **289**, 2105 (2000).

[13] L. Kouwenhoven and L. Glazman, Phys. World **14**, 33 (2001).

[14] D. Goldhaber-Gordon *et al.*, Phys. Rev. Lett. **81**, 5225 (1998).

[15] C. Beenakker, Phys. Rev. B **46**, 12841 (1992).

[16] G. Blonder, M. Tinkham, and T. Klapwijk, Phys. Rev. B **25**, 4515 (1982).

[17] M. Tinkham, *Introduction to Superconductivity* (McGraw-Hill, New York, 1996).

[18] V. Khlus, A. Dyomin, and A. Zazunov, Physica C **214**, 413 (1993).

[19] M. Buitelaar *et al.*, Phys. Rev. Lett. **91**, 057005 (2003).

Chapter 4

Local gating of carbon nanotubes

4.1 Motivation

In the previous chapters we have seen that at low temperatures carbon nanotubes can provide a platform well-suited for studying quantum dot physics. In fact, new physical phenomena such as superconducting correlations or spin injection into quantum dots can be studied in carbon nanotube quantum dots, see e.g. Ref. [1, 2, 3] and Chapter 3 of this thesis. Up to now ferromagnetic and superconducting electrodes have not been accessible in semiconductor-based quantum dots. However, the major drawback of carbon nanotube quantum dots is the missing degree of control over the dot properties such as the tunnel-coupling Γ to the leads. In contrast, dots defined in two-dimensional electron gases allow for a precise tuning of the Γs by energizing locally acting gate electrodes, see e.g. [4] and references therein. Additionally, center gates can be used in order to define double quantum dot structures with a tunable inter-dot coupling. This tunability is an essential ingredient for further experiments exploring the quantum nature of electronic states in carbon nanotubes - or, even more ambitious, for realizing quantum electronic devices such as spin- or charge-based quantum bits [5, 6, 7]. Local gates could lead to an enhanced control over the electric properties of carbon nanotubes [8, 9, 10, 11]. The following chapter will be devoted to the fabrication process and the electrical characterization of novel carbon nanotube devices with local top-gate electrodes in addition to the standard back-gate.

4.2 Experimental

The experimental challenge was to find a way to reliably manufacture local gate electrodes on carbon nanotubes. A first question to ask is how many electron-

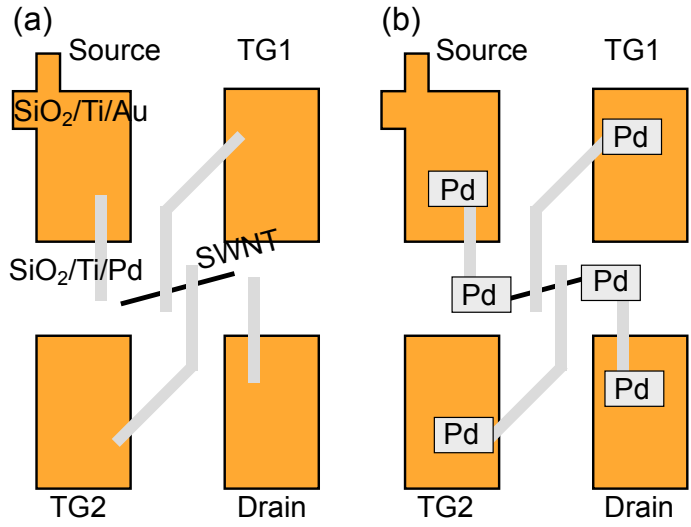

Figure 4.1: (a) After the fabrication of SiO_2/Ti/Au bond pads (orange boxes, real dimensions 200 × 300 μm) and markers (not shown), the top-gates and parts of the source/drain electrodes are defined in a second lithography and metal deposition process. (b) In a third step electrical contacts to the tube (real length few μm) and to the large pads are made. Note: In order to be more illustrative, scales are not correct.

beam-lithography and evaporation processes are needed to do so. Every additional process step may (and mostly does) lead to a lower yield of successfully operating devices. Different approaches are thinkable for manufacturing top-gates on carbon nanotubes. In a first approach tilted-angle evaporation could be used in order to define top-gates and source and drain electrodes within the same processing step. However, in this case often problems occur during the lift-off procedure of the remaining PMMA after the evaporation, see Chapter 1 for a more detailed description of the lithography process. For this reason a different method was chosen, defining gates and source / drain electrodes in two subsequent steps. In the following we will now describe the processing steps in detail:

After the initial preparation of SiO_2/Ti/Au bond pads and alignment markers, single-walled carbon nanotubes (SWNTs) were localized with a scanning electron microscope (SEM). In the following step gates and connection lines for the source-drain electrodes were defined by e-beam-lithography, see figure 4.1 (a). Electron-gun-evaporation of SiO_2 as gate-oxide, Ti as gate-metal, and Pd serving as anti-oxidant cover layer followed. The gate-oxide film thickness

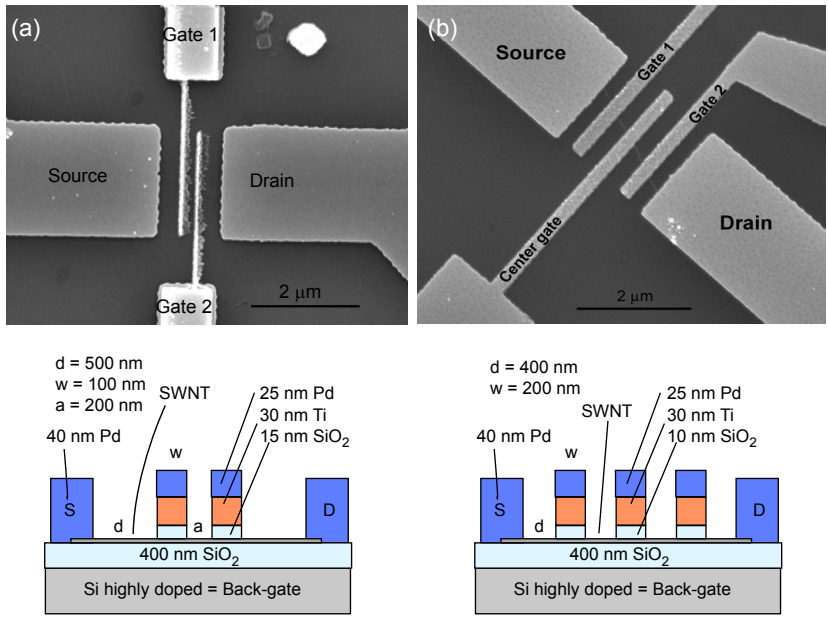

Figure 4.2: (a) SEM micrograph of a nanotube device with two top-gates. (b) SEM micrograph of a nanotube device with three top-gates. The illustrations at the bottom give dimensions and materials used for these samples.

was chosen to be either 10 nm or 15 nm, the Ti film thickness 30 nm, and the Pd one 25 nm. The materials were evaporated at a pressure of $\approx 10^{-7}$ mbar. By defining not only the top-gates, but also long connecting parts of the source-drain-electrodes with SiO_2 underneath, electrical shorts caused by long (tens-hundreds of μm) carbon nanotube bundles bridging the electrodes in parallel to the sample were practically eliminated.

Then, in a final e-beam-lithography step the source and drain electrodes of the nanotube and contacts to the large bond pads were defined, see Fig. 4.1(b). In the final e-gun-evaporation a 40 nm thick film of Pd was evaporated in order to provide good electrical contact. The evaporation conditions were the same as described above, except the substrate was kept at a constant temperature of $\approx 0°$ C by liquid nitrogen cooling of the sample holder inside the evaporation chamber. In general, the liquid nitrogen cooling reduces outgasing effects of materials inside the vacuum chamber due to heating effects during the evaporation. After removing the remaining PMMA in hot acetone, the samples were then glued into a 20-lead chip carrier and bonded.

Figures 4.2(a) and (b) show scanning electron micrographs and side-view schematics of fabricated SWNT devices with either two or three top-gates in

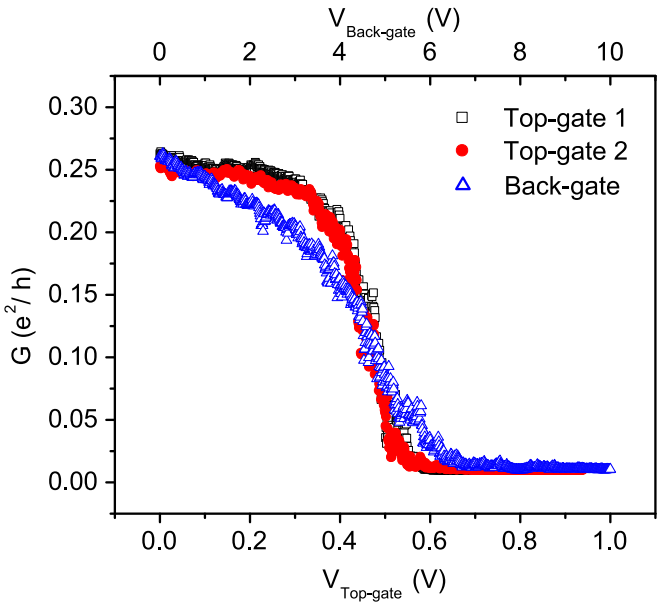

Figure 4.3: Linear conductance G for a device with two top-gate electrodes (oxide thickness 15 nm) versus top-gate- and back-gate-voltage. The gates non swept are connected to ground potential.

addition to the source and drain electrode. The spacing between source and drain electrode amounts to 1.4 μm in (a) and 2.2 μm in (b). The oxide thickness was chosen to be 15 nm in (a) and 10 nm in (b) and width of the gates 100 nm and 200 nm, respectively. Wider gates and thinner gate oxides increase the gate capacitance, since, in a simple model of a plane capacitor, $C \propto A/d$, where A denotes the area and d the spacing of the two planes. The back-gate oxide has a commonly used thickness of 400 nm.

4.3 Local gating at room temperature

Gate response

After verifying that there are no shorts from any gate to the source or drain electrode, or to any other gate, the electrical properties of the nanotube can be studied at room temperature. Figure 4.3 shows a plot of the linear conductance versus the applied voltage at either of the two top-gates (lower axis) and at the back-gate (upper axis). At a voltage of roughly 0.6 V applied to either of the two top-gates the conductance through the device is suppressed indicating the

chemical potential is shifted locally into the semiconducting gap of the SWNT. When comparing to the Si back-gate the top-gates have a much a stronger coupling $\alpha = C_{gate}/C_{\Sigma}$ where C_{Σ} is the sum of all gate and contact capacitances. For the back-gate an applied voltage of about 7 V is needed in order to reach the energy gap of the nanotube. On the one hand this rather low coupling of the back-gate is due to the thicker gate oxide (400 nm), on the other hand there are also electrostatic screening effects due to the additional metal top-gate electrodes covering parts of the tube. The screening effect of the metallic top-gates is illustrated in Fig. 4.4 which shows a colorscale plot of the calculated electrical potential in our device for an applied back-gate voltage of 10 V.

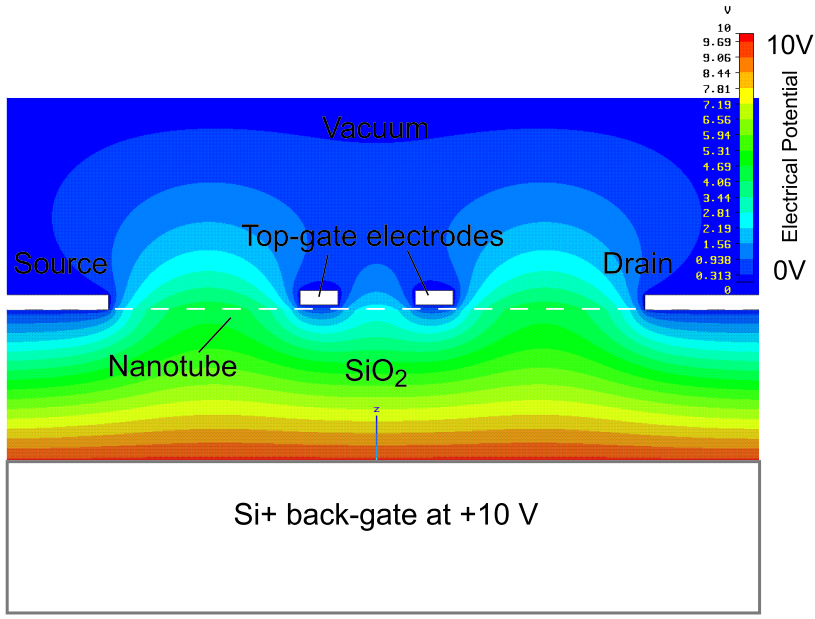

Figure 4.4: Colorscale plot of the electrical potential calculated for the two top-gate device. The back-gate is energized to +10 V, source, drain and top-gates are kept at 0 V. Screening effects are apparent underneath the top-gates and in vicinity of the source and drain electrode. Calculation by S. Feigh, TU Darmstadt.

In Fig. 4.5 the linear conductance versus gate voltage of a semiconducting SWNT device with three top-gate electrodes with a gate-oxide thickness of 10 nm is plotted. The gate-dependence is similar to the device discussed above, however, after a decrease of conductance for increasing gate voltage, the conductance rises again for more positive gate voltages. This behavior is explained by the band diagram sketched at the bottom of Fig. 4.5.

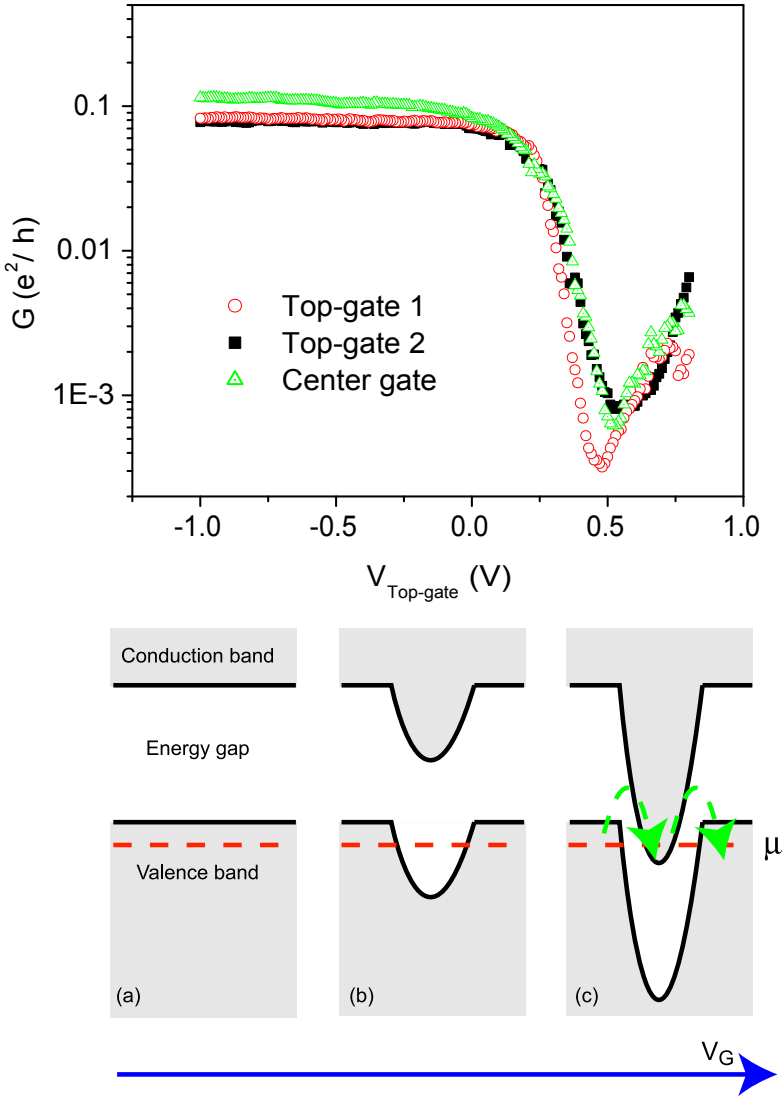

Figure 4.5: Top: Linear conductance G on a logarithmic scale for a device with three top-gate electrodes (oxide thickness 10 nm) versus top-gate-voltage. The gates non swept are connected to ground potential. Bottom: (a) - (c) illustrate the band structure for increasing top-gate voltage.

Intrinsically the tube is p-doped and the chemical potential μ resides in the valence band (a). For increasing voltage at the top-gate the potential landscape is changed locally and just below the gate μ lies within the energy gap (b). In this scenario the conductance through the nanotube reaches its minimum. With this technique it should thus be possible to create local barriers inside a carbon nanotube, allowing one to create artificial potential landscapes. If the gate voltage is increased even more, the lower edge of the conduction band will eventually reach the upper edge of the valence band (c). Now thermally activated band-to-band processes indicated by the green arrows are possible and the conductance increases again. Within this work such behavior has only been seen at 300 K indicating the high energy scales involved in band-to-band charge transfer processes.

Hysteretic gate-responses

A further important topic to address are the hysteretic characteristics of a nanotube field effect transistor. At room temperature, devices which are only back-gate controlled often suffer from strong hysteretic shifts in the gate response. For nanotube applications, such as for sensing purposes [12], no or only little hysteretic behavior is desired. Figure 4.6 compares the gate response of a semiconducting device with three top-gates when sweeping up and down either one of the top-gates (gate 2) or the back-gate. Hysteretic effects are strongly reduced in the case of the top-gate, but are prominent for the back-gate. Hysteretic behavior is mainly due to jumps of trapped charge states, e.g. in the SiO_2 underneath. The bigger the applied electrical field, the bigger the probability of such jumps. In fact, the electrical field is strongly enhanced in the vicinity of source and drain contact, due to the electrostatic bending of the field lines. Our result confirms that hysteresis effects in the conductance are related to effects occurring in the vicinity of the source and drain contact. Whereas the back-gate affects these contact regions and is hysteretic, the top-gate acts locally on the SWNT and consequently has a less hysteretic behavior.

4.4 Local gating at low temperatures

A device with two top-gates

From typical energy scales of carbon nanotube quantum dots one expects single-electron charging phenomena and finite-size effects to become important for charge-transport at low temperatures. Figure 4.7 shows colorscale plots of the differential conductance through a device with two top-gates versus the two top-gate voltages at temperatures of 77 K and 4.2 K. At 77 K, there are no pronounced features in the plot and the overall variation of the conductance is small. Regions of similar conductance are separated by diagonal lines with a slope of roughly -1. This in fact corresponds to the condition $V_{G1}+V_{G2} = const.$ where we assumed an identical coupling of gates 1 and 2, as is the case when the gate capacitances C_{G1} and C_{G2} are equal. The diagonal features indicate

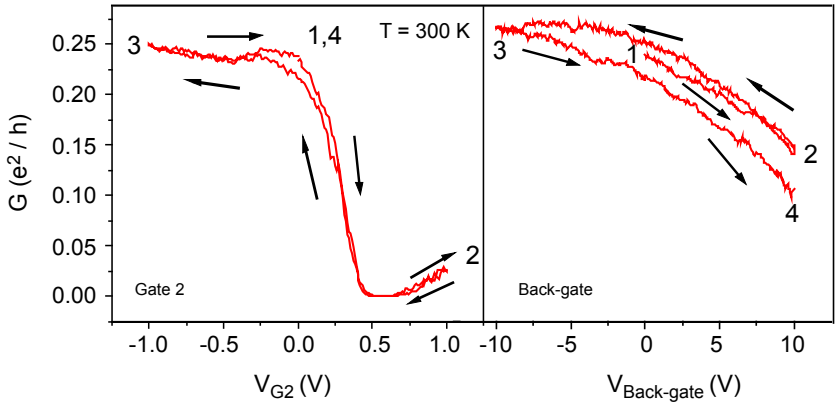

Figure 4.6: Conductance through a sample with three top-gates versus (top)-gate 2 (left) and back-gate (right). Hysteresis effects are strongly suppressed when sweeping the top-gate. Gates are swept from position 1 to 2 to 3 to 4. Gates non swept are connected to ground potential. The difference in maximum conductance is due to hysteretic behavior of the back-gate.

that both gates act equivalently and additively on the same region. At a lower temperature of 4.2 K the pattern changes dramatically towards a chessboard-like and the overall conductance decreases. The behavior inside the shown gate voltage window is not uniform. When $V_{G2}, V_{G1} < 0$ diagonal lines with a negative slope $V_{G1} = -\alpha V_{G2}$ are the most prominent features. These lines indicate a rather open state of the device, i.e. wave functions are extended along the whole nanotube and the top-gates act more or less globally. When, however, $V_{G2}, V_{G1} > 0.2$ V, the pattern exhibits rather square-like structures. This behavior suggests the formation of gate-defined, isolated islands on the nanotube.

Consequently, the following measurements of this two top-gate device were devoted to the question whether nanotubes with gates evaporated on top still can act as clean quantum dots. As an example, a region exhibiting regular Coulomb oscillations at an applied back-gate voltage between 4.2 and 5.0 V was probed. Regular Coulomb blockade diamonds with a charging energy of roughly 10 meV were observed, see the top part of Fig. 4.8. Due to the uniformity of the diamonds a single dot picture still seems a reasonable assumption in this gate voltage range. Additionally, as we will point out, the following data taken in this region allow for a rough estimate of the capacitance of the top-gate electrodes relative to that of the back-gate.

The bottom of Fig. 4.8 shows the linear conductance through the device versus back-gate voltage for four different voltages applied at gate 2, V_{G2}=0,

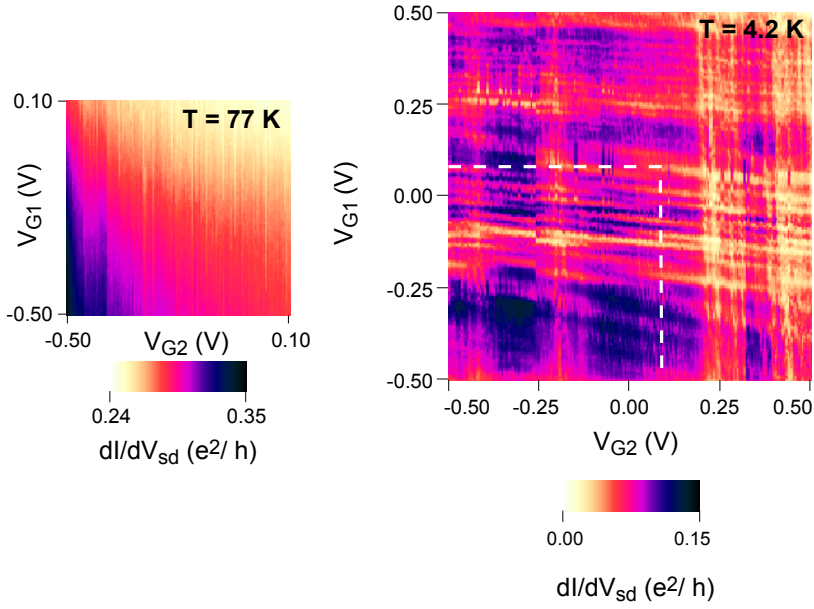

Figure 4.7: Right: Colorscale plot of the linear differential conductance at 4.2 K at a back-gate voltage of 0 V. Left: Linear differential conductance of the dashed region in the right plot at 77 K. Note the different colorscale of the two plots.

0.01, 0.02 and 0.03 V. Gate 1 was kept at a constant voltage of $V_{G1} = 0$ V. When energizing gate 2 to more positive potentials the position of the peaks in differential conductance shifts to lower values of the back-gate voltage indicating a resonance condition $\alpha_{Back-gate} V_{Back-gate} + \alpha_{G2} V_{G2} = const.$ is fulfilled. Here the α's denote the coupling C_{gate}/C_Σ of the respective gate electrode, with C_Σ being the sum of all capacitances of the device. Note, however, that such behavior assumes that the top-gates either act globally as does the back-gate or that transport through the device is mainly governed by a small region affected by the top-gate. In fact, the data show that this assumption holds only partially. Whereas some of the conductance peaks show up in all four traces (shifted to smaller back-gate voltages), others dramatically transform. The double-peaked structure around $V_{Back-gate} = 4.4$ V, for example, finally transforms into a single peak at $V_{G2} = 0.03$ V. Still we can get a rough estimate of the top-gate coupling from the slope of the dashed traces following the shift of the peaks which yields $C_{G2} \approx 3\, C_{Back-gate}$.

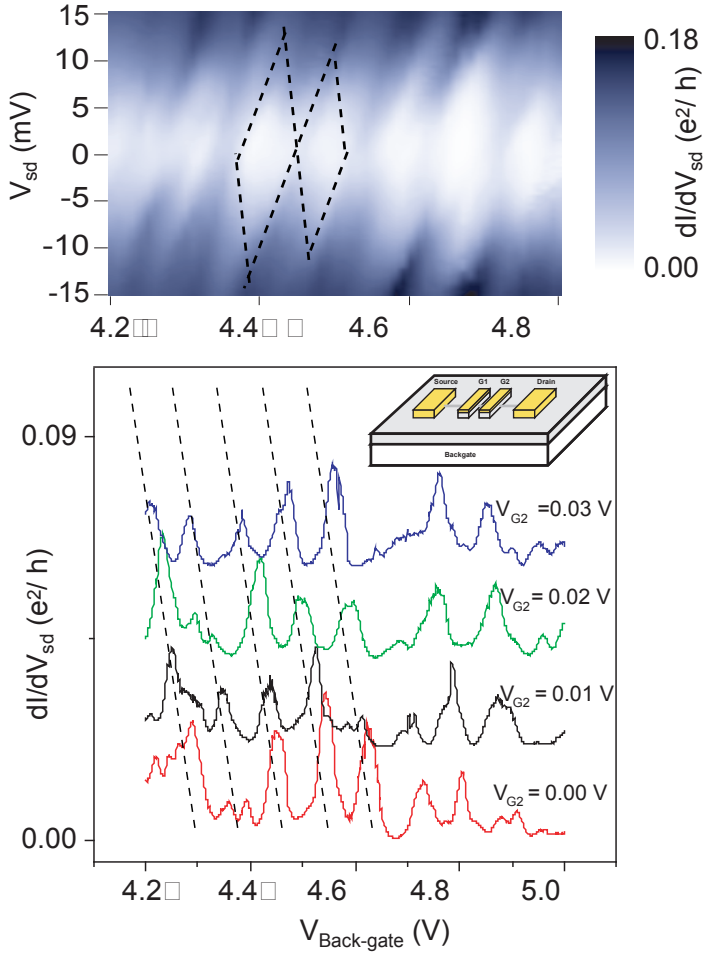

Figure 4.8: Top: Colorscale plot of the differential conductance versus source-drain bias voltage and back-gate. Bottom: Trace of the linear differential conductance for the same range of back-gate voltage. Traces for different values of V_{G2} are offset by 0.02 e^2/h for clarity. V_{G1}=0 for all traces.

A device with three top-gates

Also devices with three top-gate electrodes were measured at 4.2 K. In Fig. 4.9(a) the linear differential conductance is plotted versus voltages applied at the top-gates 1 and 2 for a constant center-gate voltage of $V_{Center} = -1$ V. At top-gate voltages of around 0.5 V the chemical potential is shifted into the energy gap of the nanotube and electrical transport is suppressed. The pattern mostly shows high-conductance lines with a small slope and turns into a more square-like one when approaching the energy gap. Figure 4.9(b) shows a zoom for such a region exhibiting a square-like pattern. In fact, taking into account features are strongly smeared out by temperature, the stability diagram resembles a honeycomb pattern characteristic for a double quantum dot. In principle the dimensions of the cells obtained correspond to the charging energy of the dots. However, a precise value is difficult to extract as these dimensions vary strongly. A more careful analysis of double quantum dots defined in devices with three top-gates will be the focus of the following chapter of this thesis. The main difference, as compared to the device with two top-gates, is the electrostatic screening of the center gate. The outermost gates act more locally and less additively, resulting in more rectangular patterns of the stability diagram.

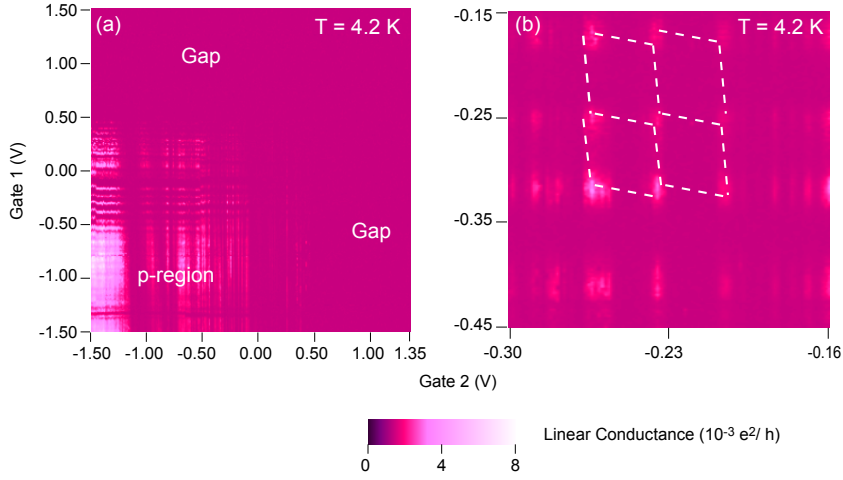

Figure 4.9: (a) Colorscale plot of the conductance versus gate 1 and gate 2 for constant center-gate voltage at 4.2 K. (b) Zoom of a region exhibiting a regular pattern.

References

[1] M. Buitelaar, T. Nussbaumer, and C. Schönenberger, Phys. Rev. Lett. **89**, 256801 (2002).

[2] M. Buitelaar *et al.*, Phys. Rev. Lett. **91**, 057005 (2003).

[3] S. Sahoo *et al.*, Nature Physics **1**, 99 (2005).

[4] L. Kouwenhoven *et al.*, Proceedings of the Advanced Study Institute on Mesoscopic Electron Transport, edited by L.L. Sohn, L.P. Kouwenhoven, G. Schön (Kluwer). (1997).

[5] G. Burkard, D. Loss, and D. P. DiVincenzo, Phys. Rev. B **59**, 2070 (1999).

[6] D. Loss and D. DiVincenzo, Phys. Rev. A **57**, 120 (1998).

[7] A. Shnirman and G. Schön, Phys. Rev. B **57**, 15400 (1998).

[8] J. Appenzeller, Y.-M. Lin, J. Knoch, and P. Avouris, Phys. Rev. Lett. **93**, 196805 (2004).

[9] M. Biercuk, N. Mason, and C. Marcus, Nano Letters **4**, 1 (2004).

[10] M. Biercuk, N. Mason, J. Chow, and C. Marcus, Nano Letters **4**, 2499 (2004).

[11] M. Biercuk *et al.*, Nano Letters **5**, 1267 (2005).

[12] A. Star *et al.*, Nano Letters **3**, 1421 (2003).

Chapter 5

Carbon nanotube double quantum dots

5.1 Motivation

The interference of quantum states is one of the most striking features of nature enabling the formation of molecular bonds. In fact, quantum interference is the glue that keeps matter together. Coupled quantum dots are engineered model systems in which the interplay between quantum interference and interactions of electrons can be studied in regimes that are not accessible in true molecules. For example, such devices have allowed for probing and controlling quantum-mechanically superposed states in terms of the electron charge and spin [1, 2, 3, 4, 5]. Additionally, being a quantum two-level system, these so-called artificial molecules have been proposed as coupled spin quantum bits for future applications in information technology [6]. Whereas most electrical transport experiments on coupled quantum dots so far have investigated GaAs-based semiconductor quantum dots (see [7] and references therein), only recently such structures have been realized in carbon nanotubes and semiconducting nanowires [8, 9, 10]. These materials are attractive not just for the relative ease in production, but also for the fact that superconducting and ferromagnetic contacts have been demonstrated [11, 12, 13], opening up a road for various kinds of novel quantum devices [14]. In addition the effect of reduced hyperfine interactions on spin dephasing times may be probed in carbon nanotube coupled quantum dots, as the nuclear spin of the dominant isotope ^{12}C is zero.

In this Chapter electrical transport measurements through a semiconducting single-walled carbon nanotube (SWNT) with source and drain electrodes and three additional top-gates are described. In specific gate voltage ranges the system acts as a double quantum dot with large inter-dot tunnel coupling t allowing for the observation of a quantum-mechanical superposition of $|n, m+1\rangle$ and $|n+1, m\rangle$ states where n and m denote the number of charges on the

left and right dot, respectively. Using an effective single particle picture we precisely determine the tunnel coupling and identify molecular-like states with wave functions extending over the whole nanotube double dot.

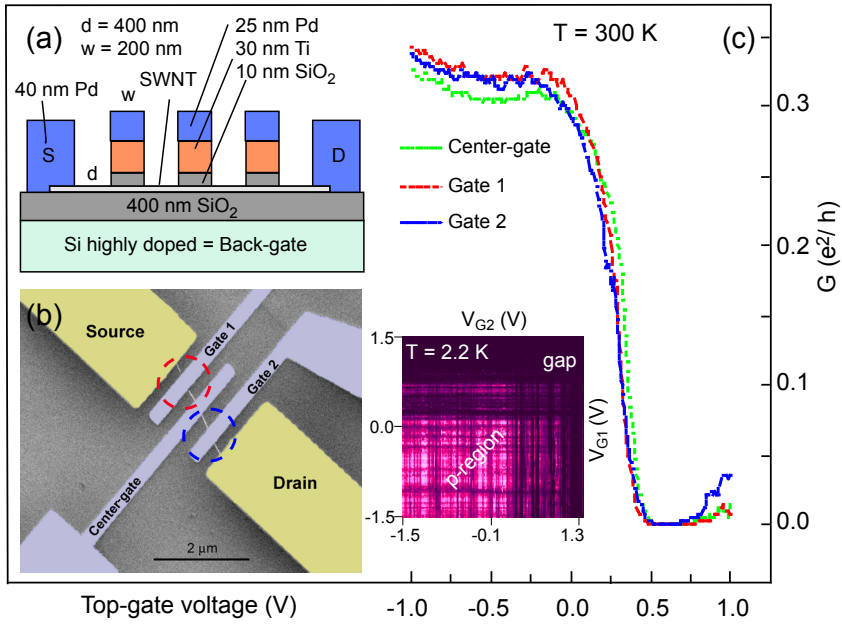

Figure 5.1: (a) Schematic representation of the fabricated device. The three top-gates are labelled gate 1, center gate and gate 2 (from source to drain). (b) Scanning electron micrograph of a sample fabricated identically to the one measured. The distance from source to drain is 2.2 μm. Dashed circles denote the regions affected by gates 1 and 2. (c) Conductance G through the device at T = 300 K plotted versus top-gate voltage. All gates not swept are connected to ground. Note: Differences between the individual gate scans at 0 V arise from slightly hysteretic gate responses. Inset: Colorscale plot of the linear conductance versus gate 1 and gate 2 for fixed V_{Center} = -1 V at 2.2 K. Bright corresponds to 0.4 e^2/h, dark to 0 e^2/h.

5.2 Sample preparation and characterization

Single-walled carbon nanotubes were grown by means of chemical vapor deposition on a highly doped Si substrate covered by an insulating layer of 400 nm SiO_2. Details of the SWNT growth can be found in Chapter 1 and in Ref. [15]. Single nanotubes were selected using a scanning electron microscope. Three 200 nm wide local gates equally spaced by 400 nm were then defined by means of

standard electron beam lithography and e-gun evaporation of SiO_2, Ti and Pd. The fabrication of the top-gate electrodes followed the recipes given in Chapter 4, the gate oxide thickness was chosen to be 10 nm. Finally Pd source and drain contacts were fabricated. Figure 5.1(a) shows a schematic of the device, the materials used, and corresponding film thicknesses. A scanning electron micrograph of a device fabricated identically to the one measured is shown in Fig. 5.1(b).

Room temperature characterization identifies the semiconducting nature and an intrinsic p-doping state of the nanotube. Figure 5.1(c) shows the linear conductance through the device as a function of the three top-gate voltages and the back-gate voltage. At a top-gate voltage of roughly 0.4 V conductance is suppressed indicating the chemical potential is shifted into the energy gap of the semiconducting tube. We attribute the conductance increase at more positive voltages to band-to-band-tunneling effects, as reported in previous studies of semiconducting SWNT with top-gates [16]. Five identically prepared devices were tested at room temperature and showed the same behavior. The inset of Fig. 5.1(c) shows a colorscale plot of the linear conductance versus gates 1 and 2 for a constant center gate voltage at 2.2 K. Again, applying positive voltages of the order 1 V to any of the top-gates locally shifts the chemical potential into the energy gap of the intrinsically p-doped SWNT and thus suppresses electrical transport.

Low-temperature measurements were performed in a ^{3}He cryostat with a base temperature of 290 mK. Differential conductance dI/dV_{sd} was measured using standard lock-in techniques with an excitation voltage of typically 7.5 μV at a frequency of 327.7 Hz and an I/V converter with a gain of 10^7 V/A. For the measurements presented in the following center gate and back-gate were kept at constant voltages V_{Center}=-0.1 V, V_{Back}=0 V, and no magnetic field was applied. A detailed description of the electrical setup is given in the Appendix.

5.3 Double quantum dot behavior

Sweeping gate 1 and gate 2 leads to pronounced oscillations of the conductance due to single electron charging phenomena and finite size effects of the nanotube. A colorscale plot of the differential conductance dI/dV_{sd} is depicted in Fig. 5.2(a) exhibiting the so-called "honeycomb" stability diagram characteristic for double quantum dots. Within each cell of the pattern the number of holes (n,m) on each of the two dots is constant. Energizing gate 1 (2) to more negative voltages successively fills holes into dot 1 (2) whereas a more positive voltage pushes holes out of the dot. Two identical devices were measured at low temperatures and both exhibited a honeycomb pattern. In a third sample, with shorter source-drain spacing and smaller width of the gates, a double dot could be defined, too. Data from the second sample are presented in Sections 5.7 and 5.8, from the third one in Section 5.9.

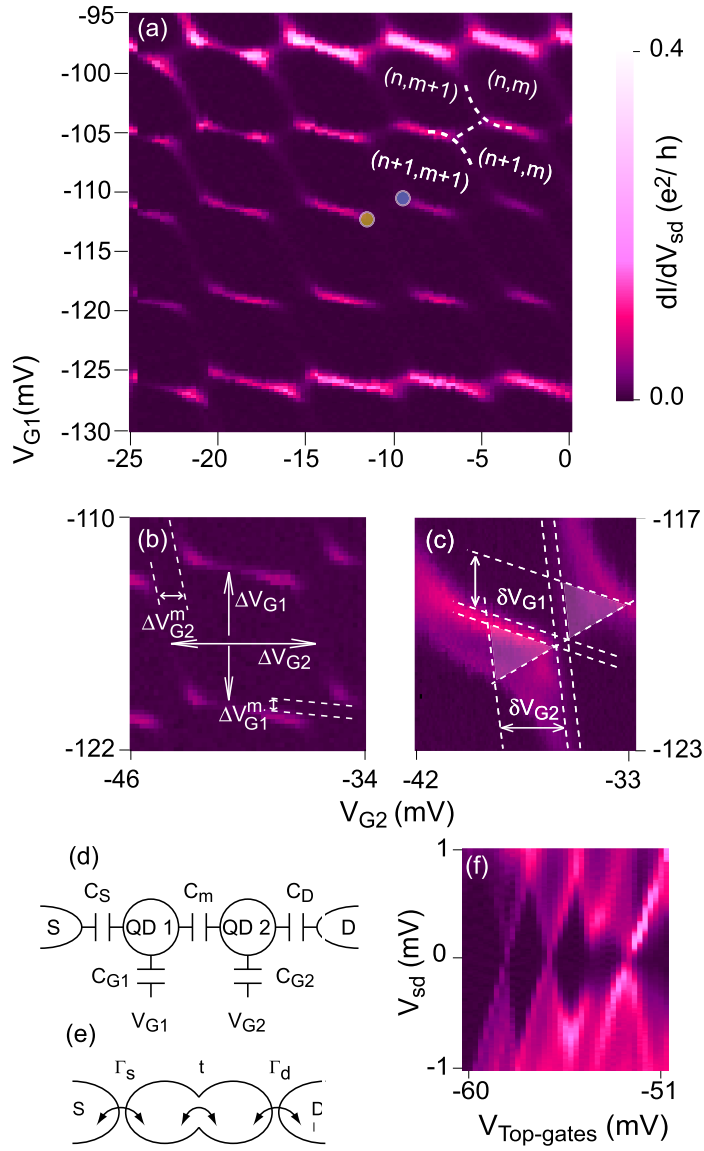

Figure 5.2: (a) Colorscale plot of the conductance at a temperature of T=290 mK and $V_{sd} = -128$ μV. The resulting honeycomb pattern represents the charge stability diagram of coupled double quantum dots. Two triple points (located at the degeneracy point of three stable charge configurations) are marked by a yellow and a blue dot for clarity. Dashed lines are guide to the eye. (b) Close-up of a single honeycomb cell. (c) Vicinity of the triple points at a source-drain bias voltage of 391 μV. (d) Capacitive model of a double quantum dot device. (e) Schematics of a double quantum dot with molecular eigenstates coupled to source and drain. (f) Colorscale plot of the conductance versus source-drain and top-gate voltage (all three top-gates connected in parallel): Coulomb diamonds.

The stability diagram allows for a quantitative determination of dot and gate capacitances (see Fig. 5.2(d)) of the device [7]. From the dimensions of a single cell as depicted in Fig. 5.2(b) and $\Delta V_{G1,2} =\mid e \mid /C_{G1,2}$ one obtains gate capacitances C_{G1}=23 aF and C_{G2}=21 aF. Applying a finite source-drain bias voltage V_{sd} results in a broadening of the triple points at the honeycomb edges into triangular-shaped regions, see Fig. 5.2(c). In our device the triangles are less clear defined due to finite temperature and the strong tunnel coupling between the dots which we will discuss in the following paragraphs. Using the relation $C_{G1,2}/C_{1,2} =\mid V_{sd} \mid /\delta V_{G1,2}$ the capacitances $C_1 = C_S + C_{G1} + C_m$ and $C_2 = C_D + C_{G2} + C_m$ follow to be 84 aF and 145 aF, respectively. On-site charging energies of both dots then yield $U_{C,1} = e^2/C_1 \approx 1{,}9$ meV and $U_{C,2} = e^2/C_2 \approx 1.1$ meV in satisfactory agreement with the dimensions of the Coulomb blockade diamonds at finite bias, see Fig. 5.2(f).

In order to estimate the mutual capacitance C_m in between the two dots we first neglect a finite tunnel coupling and assume a purely electrostatic interaction. From the triple-point spacing given in Fig. 5.2(b) and $\Delta V^m_{G1,2} =\mid e \mid C_m/(C_{G1,2}\, C_{2,1})$ one then determines $C_m \approx 15$ aF. Note, that in an electrostatic model one typically overestimates C_m and that this value is an upper bound. In Fig. 5.2(a), electrical transport is enabled on the edges of the honeycomb cells and the high-conductive features exhibit , despite the applied bias of $128\,\mu$V partially washing out this feature, a strong curvature close to the triple points. These two features suggest a significant (quantum-mechanical) tunnel coupling in addition to the (classical) electrostatic interaction between the charges on the two dots.

5.4 Extracting the tunnel coupling

In order to gain a deeper insight into the system and to evaluate t we adopt a model Hamiltonian of the form $H = H_C + H_T + H_L$ which describes the system depicted in Fig. 5.2(e) [17]. Here, H_C describes the orbital and Coulomb energies of the double dot system, H_T describes the tunnel-coupling between the two dots and H_L the coupling of each dot to the leads. We assume a simple model for the Coulomb interaction, including only on-site (U) and nearest-neighbor (U') charging energies. In this case, states with a fixed number of charges on each dot are eigenstates of H_C: $H_C|m,n\rangle = E_{mn}|m,n\rangle$ where $E_{mn} = E^{orb}_{mn} + \frac{U}{2}\,[m(m-1)+n(n-1)]+U'mn+E_1m+E_2n$. E^{orb}_{mn} is the total orbital energy of the $|m,n\rangle$ charge configuration, and $E_{1(2)}$ is the single-particle energy of the left (right) dot, supplied by the gate voltages $V_{G1,2}$. In a simple picture of sequential tunneling through H_C-eigenstates (neglecting H_T to leading order), one would expect nonzero conductance only at the triple points. It is only at these points that sequential tunneling processes of the kind $|m,n\rangle \rightarrow |m,n+1\rangle \rightarrow |m+1,n\rangle \rightarrow |m,n\rangle$ can lead to charge transport through the double dot from, in this case, the right lead to the left (blue sequence in the inset of Fig. 5.3(b)). However, if we allow for superposed double dot states of the form $\alpha|m,n+1\rangle + \beta|m+1,n\rangle$, having one excess hole relative to $|n,m\rangle$, sequential transport

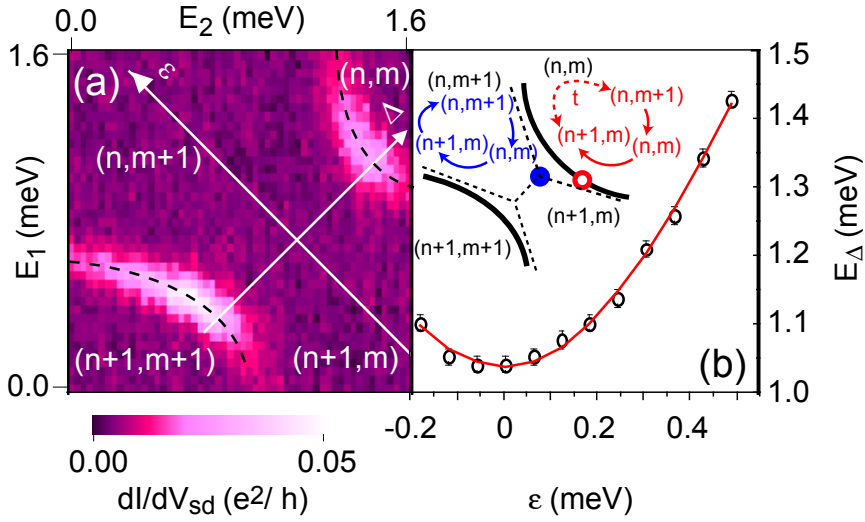

Figure 5.3: (a) Colorscale plot of the differential conductance (V_{sd}=20μV, T=290 mK) in the vicinity of the two triple points in the bottom right corner of Fig. 5.2(b). Dashed lines are guides to the eye. (b) Spacing E_Δ (see Eq. (5.2)) of the two wings with respect to the Δ-direction versus detuning ϵ. Inset: Schematics of sequential tunnel processes allowed at the triple points (blue dot) and at the honeycomb edges (red circle) via molecular states.

is possible along the honeycomb edges as well (red sequence in the inset of Fig. 5.3(b)). Such superposed states are induced by a tunneling term of the form $H_T = t\,(|m, n+1\rangle\langle m+1, n| + \text{h.c.})$. The sequential transport then proceeds through the eigenstates $|E\rangle$ of $H_C + H_T$. For spinless holes and assuming that only a single eigenstate $|E\rangle$ participates in transport, we find that the stationary current is given by

$$I = |e|\,\Gamma\,|\alpha\beta|^2\,[f_1(\mu_{mol}) - f_2(\mu_{mol})]\,. \tag{5.1}$$

Here, $f_l(\mu_{mol}) = 1/\left(\exp\left[(\mu_{mol} - \mu_l)/kT\right] + 1\right)$ is a Fermi function at temperature T, μ_l ($l = 1(2)$) the chemical potential of the source (drain) leads, and Γ the dot-lead tunneling rate. The chemical potential of the molecular level μ_{mol} depends on whether sequential tunneling occurs at $|n, m\rangle \leftrightarrow |E\rangle$ (right branch in the inset of Fig. 5.3(b)), or at $|n+1, m+1\rangle \leftrightarrow |E\rangle$ (left branch): $\mu_{mol} = E - E_{nm}$ for the former and $E_{n+1,m+1} - E$ for the latter. Note that in a spinless description we exclude the possibility of e.g. spin-blockade, which, in our experiment, has not been observed.

With the help of Eq. (5.1), the data allow for a precise quantitative analysis of the tunnel coupling t between the dots. Fig. 5.3(a) shows a colorscale plot (linear

scale) of the differential conductance at $V_{sd} = 20\mu\text{V} \approx kT$ in the vicinity of a triple point region. As expected in the presence of tunnel-coupled eigenstates transport is possible not only at the triple points but also on the wings extending from the triple points. The two gate voltages V_{G1} and V_{G2} are converted into energies E_1 and E_2 by multiplying them with the conversion factors $\alpha_1 = 0.42e$ and $\alpha_2 = 0.29e$, which we obtain from the splitting of a differential conductance resonance at finite bias voltage, as will be discussed in the context of Fig. 5.4. We then change variables to $\epsilon = (E_1 - E_2)/\sqrt{2}$ and $\Delta = (E_1 + E_2)/\sqrt{2}$. In terms of these new variables, the double-dot molecular eigenenergies are (up to a constant offset) $E^{\pm}(\Delta, \epsilon) = E_{mn}(\Delta, \epsilon) + \left(\Delta \mp \sqrt{\epsilon^2 + 2t^2}\right)/\sqrt{2}$. When the bias and temperature are smaller than the double-dot level spacing (i.e., $V_{sd}, kT < E^- - E^+$), transport occurs only through the ground-state $|E^+\rangle$. For small bias, we set $\mu_1 = \mu_2 = \mu$, then transport is due to energy-conserving transitions between the state $|E^+\rangle$ and either $|m, n\rangle$ (when $E^+ - E_{mn} = \mu$) or $|m+1, n+1\rangle$ (when $E_{m+1,n+1} - E^+ = \mu$). These conditions are fulfilled at the two high-conductance wings. The separation of the wings in the Δ-direction (E_Δ) is given by:

$$E_\Delta = \sqrt{2}U' + \sqrt{4\epsilon^2 + 8t^2}. \tag{5.2}$$

In Fig. 5.3(b) the spacing of the two wings E_Δ is plotted versus the detuning ϵ and fitted to Eq. (5.2). Satisfactory fits to the data yield a tunnel coupling of $t = 310 \ldots 370\,\mu\text{eV}$ and $U' \leq 100\,\mu\text{eV}$. The fit plotted yields $t = 358\,\mu\text{eV}$ and $U' = 16\,\mu eV$. One can relate U' to the capacitances of the double-dot: $U' = \frac{2e^2 C_m}{C_1 C_2 - C_m^2}$ [18]. Evaluating for $U' \leq 100\,\mu\text{eV}$ one obtains a mutual capacitance $C_m \leq 4\,\text{aF}$ consistent with the electrostatic estimate yielding an upper bound of 15 aF. We conclude that the triple-point spacing $E_\Delta(\epsilon = 0)$ at this specific position in gate-voltage is predominantly due to coherent tunneling between the dots and only by a much smaller extent to the electrostatic interaction U', which is possibly screened by the metallic center gate.

5.5 Molecular states

Figure 5.4 shows a map of the differential conductance in the vicinity of the two triple points (same region as Fig. 5.3) for three different source-drain voltages. On the right side, traces of the differential conductance with respect to gate 1 are extracted at the same position of gate 2 (dashed line) well separated from the triple points. In Fig. 5.4(a) the conductance trace has a single peak. In the finite-bias cases (b) and (c) the single peak splits into two peaks which are separated by the applied bias voltage. Due to the linear dependence of the peak splitting on bias, see the inset of Fig. 5.4(a), the entrance of the second peak does not indicate an additional level entering the bias window. To understand this feature, we consider our conductance measurements in greater detail. In our setup, differential conductance is measured by modulating the source voltage (μ_1), keeping the drain voltage (μ_2) and all other gate voltages fixed.

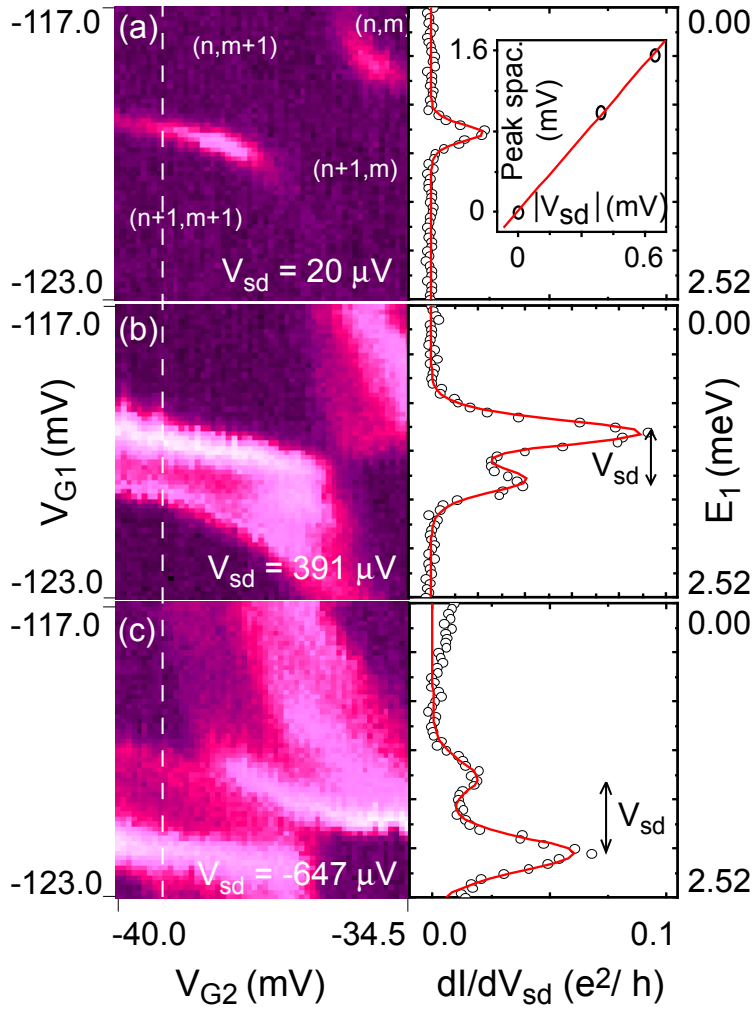

Figure 5.4: Colorscale plot of the differential conductance in the vicinity of the same triple point as in Fig. 3 for three different bias voltage: (a) V_{sd}=20μV, (b) V_{sd}=391μV and (c) $V_{sd} = -647\mu$V. Dark corresponds to 0 e^2/h and bright to 0.1 e^2/h. On the right open circles denote traces of the differential conductance taken at the position of the dashed line. Solid lines represent fits to the line shape given by Eq. (5.3). Left-hand scale: Voltage applied to gate 1. Right-hand scale: Voltage applied to gate 1 converted into energy.

Capacitive coupling of the source lead to the double-dot levels results in a simultaneous modulation of the molecular level μ_{mol}, albeit with an amplitude reduced by the factor $r = \partial\mu_{mol}/\partial\mu_1 = C_S/C_\Sigma$, where $C_\Sigma \approx C_S + C_D + C_{G1} + C_{G2}$. Here, it is assumed that the mean double-dot charge is fixed during modulation. From Eq. (5.1) the differential conductance for our setup is then given by

$$\frac{dI}{d\mu_1} = -|e|\,\Gamma\,|\alpha\beta|^2\,[(1-r)\,f_1'(\mu_{mol}) + r f_2'(\mu_{mol})]\,, \tag{5.3}$$

where $f_l'(x) = \frac{d}{dx} f_l(x)$. Thus, we expect a double-peaked structure like that in Fig. 5.4, with peaks separated by the bias, consistent with the above observations. In fact we can use the peak-splitting in order to convert top-gate voltages into energy more precisely than by using the finite-bias triangles and obtain the conversion factors given above. For our device, we have $C_S \approx 65\,\mathrm{aF}$, $C_\Sigma \approx C_S + C_D + C_{G1} + C_{G2} \approx 230\,\mathrm{aF}$, which gives $r \approx 0.3$. According to this model the relative height of the two differential conductance peaks should be roughly $\frac{r}{1-r} \approx 0.5$. This value is consistent with the data shown in Fig. 5.4 (with ratios of 0.42 in (b) and 0.28 in (c)). Additionally, we find that the asymmetry of the peaks switches from positive (b) to negative (c) bias, as is expected from Eq. (5.3).

The data in Fig. 5.4(a) can be fit to Eq. (5.3) yielding a peak width of 49 μeV. Note that in this case $V_{sd} \approx kT$ and the peak thus does not split. Subtracting the bias of 20 μeV one obtains an effective temperature of the electrons of 29 μeV $\approx$ 335 mK. Fitting Fig. 4(b) and 4(c) to Eq. (5.3), one obtains a bigger peak width corresponding to temperatures of 866 mK and 1180 mK, respectively, which we attribute to Joule heating at finite bias. The excellent agreement of the sequential tunneling fits is an additional indication of the molecular double-dot system. We emphasize the sequential nature of the charge transport far off the triple points and outside the finite-bias triangles in contrast to transport attributed to co-tunneling at the honeycomb edges in absence of molecular states.

5.6 Temperature dependence

A further tool to probe the quantum states of the artificial molecule is their temperature dependence. For electrical transport through eigenstates one expects resonant behavior, i.e. an increasing conductance for decreasing temperatures. In particular, in Eq.(5.3) the peak differential conductance is proportional to $1/T$. In the case of co-tunneling, however, a T^λ power law dependence of the differential conductance is expected, with $\lambda > 0$ [19].

Figure 5.5(a) shows the differential conductance through the double dot versus the voltage applied at gate 1 at different temperatures. The potential of gate 2 is kept constant, $V_{G2} = -18.5$ mV. The trace corresponds to a vertical cut through the bottom left triple point of the honeycomb cell depicted in the inset of Fig. 5.5(b).

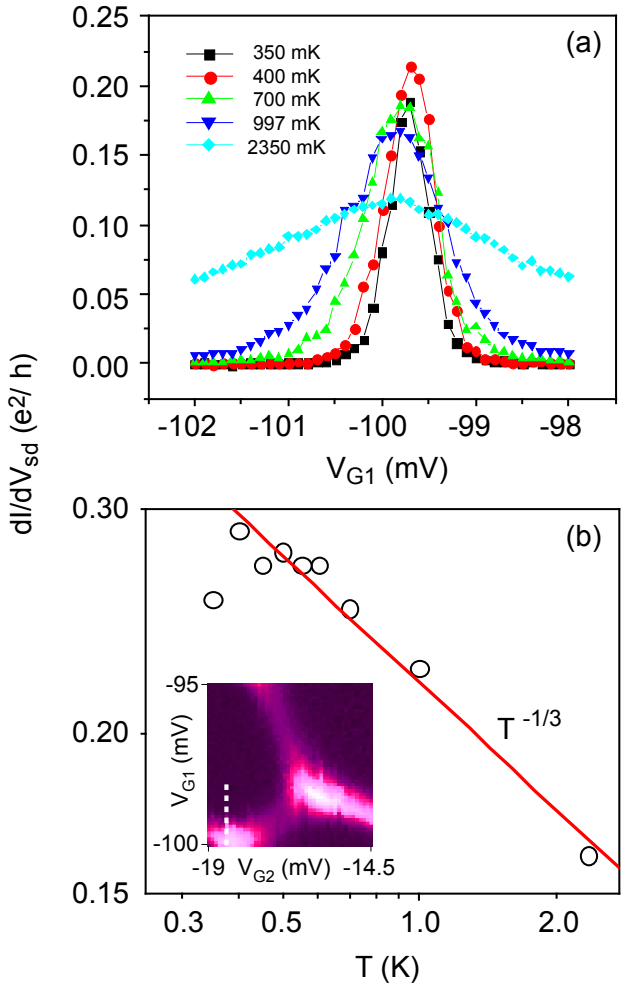

Figure 5.5: (a) Differential conductance versus V_{G1} at fixed $V_{G2} = -18.5$ mV for five different temperatures, T = 350, 400, 700, 997 and 2350 mK. (b) Peak conductance versus temperature on a double logarithmic scale. The inset shows the top left honeycomb cell from Fig. 5.2(a). The dashed line denotes the position the scans were taken at.

The width of the peaks decreases with temperature, we are thus in the regime $kT > \Gamma$. For temperatures down to 400 mK the peak height increases with temperature, as is the case for resonant tunneling. The 350 mK data, however, show a decrease of the maximum conductance. The peak height is plotted versus temperature on a double logarithmic scale in Fig. 5.5(b). A linear fit (not taking into account the 350 mK data) yields a slope of -1/3, consequently the peak conductance is proportional to $T^{-1/3}$. The exponent is surprising, as it is different from the $1/T$ scaling discussed above. A possible explanation is a combination of coherent, sequential tunneling and some amount of co-tunneling, both taking place at this position in the stability diagram. The data is taken at an applied bias of $V_{sd} = -128\,\mu$V, therefore inelastic processes such as electron-phonon scattering possibly affect transport as well. An explanation for the conductance-decrease at 350 mK could be an additional energy scale entering, such as exchange, orbital energy, or even Kondo correlations. Recalling that Mason et al. reported an unconventional temperature dependence of transport through a more decoupled nanotube double dot as well [8], this issue remains to be fully understood.

5.7 Control experiment with a second device

In the previous sections of this chapter we have described the local gate control of a double quantum dot in a carbon nanotube. A natural question arising is whether this is an intrinsic double quantum dot, e.g. defined by a scatterer in the nanotube, or whether the double dot is gate-defined. In order to check this, a second, identically fabricated sample was measured. Room temperature behavior was found to be very similar to the first sample, also identifying a semiconducting SWNT and an intrinsic p-doping. Unfortunately in this sample gate 2 was not working properly at low temperatures, the gate coupling was about two orders of magnitude too low. Such behavior can be explained by, e.g. a broken connection line on chip close to the device or a loose contact. However, still double quantum dot behavior could be probed by sweeping gate 1 and the center gate. The occurrence of double quantum dots in two independent samples strongly suggests that they are indeed gate-defined and not intrinsic ones.

In contrast to the data where gate 1 and gate 2 are swept, the center gate acts on both dots as it is not screened by a metal gate electrode in between. We would thus expect a bigger cross capacitance. A bigger cross capacitance leads to a more diagonal honeycomb pattern as compared to a smaller one. In Fig. 5.6 the honeycomb stability diagram of the double dot is evident in a colorscale plot of the differential conductance versus gate 1 and center gate. Indeed the honeycomb pattern is more diagonal than in case of Fig. 5.2(a), consistent with our expectations. Figure 5.6(b) shows a zoom of a triple point region at a bias of $V_{sd} = -550\,\mu$V. Here, the triangles at finite bias are well resolved indicating a smaller tunnel coupling in between the two dots. In analogy to Section 5.3 we can evaluate the double dot capacitances in an electrostatic model. The capacitances yield: $C_{G1} \approx 25$ aF, $C_{CG} \approx 60$ aF, $C_1 \approx 90$ aF,

$C_2 \approx 270$ aF, and $C_m \approx 50$ aF. In our notation, C_2 is the total capacitance of the dot controlled by the center gate. Differently-sized honeycomb cells suggest an estimate of the orbital energy of dot 2, $\Delta E_2 \approx 2.5 \times U_{C,2} \approx 0.8$ meV. Here $U_{C,2} = e^2/2C \approx 0.3$ meV denotes the on-site repulsion energy of dot 2.

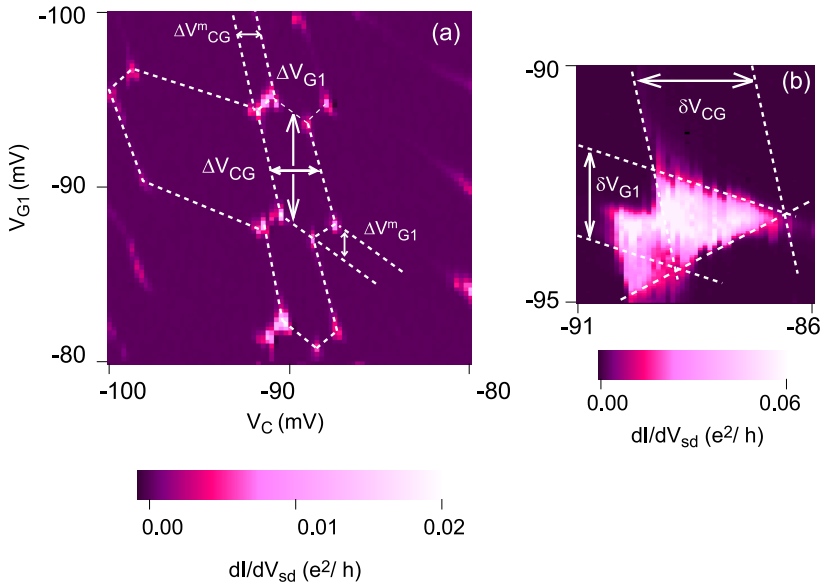

Figure 5.6: (a) Colorscale plot of the differential conductance versus gate 1 and center gate for the second sample, exhibiting a honeycomb pattern. (b) Zoom of a triple point region at an applied bias of $V_{sd} = -550\,\mu$V. The finite bias triangles overlap. All data is taken at base temperature of our dilution refrigerator, $T_{el} \approx 50$ mK, see Appendix.

5.8 DC measurements

The measurements presented in this chapter so far were taken using lock-in amplifying techniques and a small excitation voltage $V_{ac} \leq kT$. In Section 5.5 this AC technique has led, as one directly probes the differential conductance dI/dV_{sd}, to the occurrence of a double-peak structure in the charge-stability diagram at finite bias. If one probed the dc current I_{dc} flowing through the double dot rather than dI/dV_{sd}, this double-peak structure should not be present. Figure 5.7(a) and (b) show a colorscale representation of the dc current through the second sample at base temperature of our dilution refrigerator. The applied

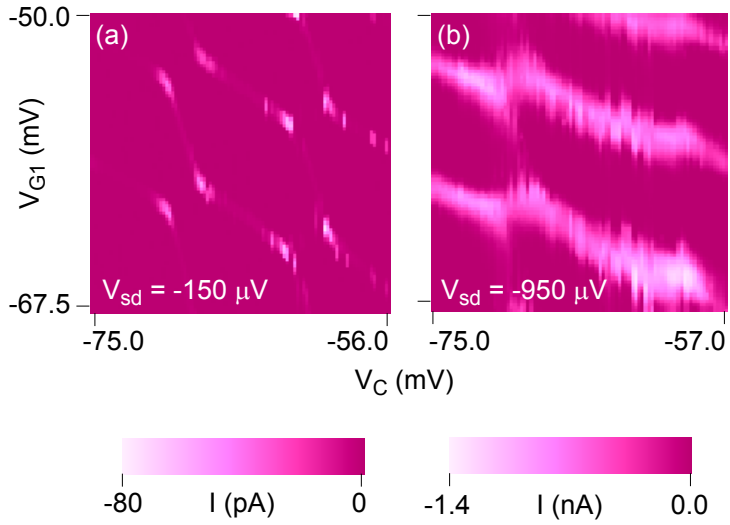

Figure 5.7: Colorscale plot of the current through a nanotube double quantum dot for two different source-drain voltages: (a) $V_{sd} = -150\,\mu$V (b) $V_{sd} = -950\,\mu$V.

bias voltage is 150 μV in (a) and 950 μV in (b). The honeycomb pattern typical for double quantum dots can be observed in the current as well. In (b) the bias leads to a significant broadening of the features and to fluctuations of the top-gate potentials. As expected for a measurement of the dc current, the bias-broadened honeycomb edges do not show a double-peaked structure, which, if present, should still be observable despite the fluctuations. This result confirms the model we have used in order to analyze the measurements of differential conductance through the nanotube double quantum dot.

5.9 Mapping the molecular wavefunctions

In order to obtain an even better understanding of artificial molecules gate-defined in SWNTs, a third device with a slightly different geometry was prepared. In this sample the distance from source to drain was only 1.2 μm in contrast to 2.2 μm in the case of the first two devices described in this chapter. Also, the width of the top-gates was scaled down to 100 nm, see the top right part of Fig. 5.8. Instead of using only Pd for source and drain contacts, a 12 nm layer of Pd followed by a 60 nm layer of Al were evaporated. Although intended, the bilayer did not become superconducting at low temperatures, and remained in the normal state. Confirming the previous results, this third device again

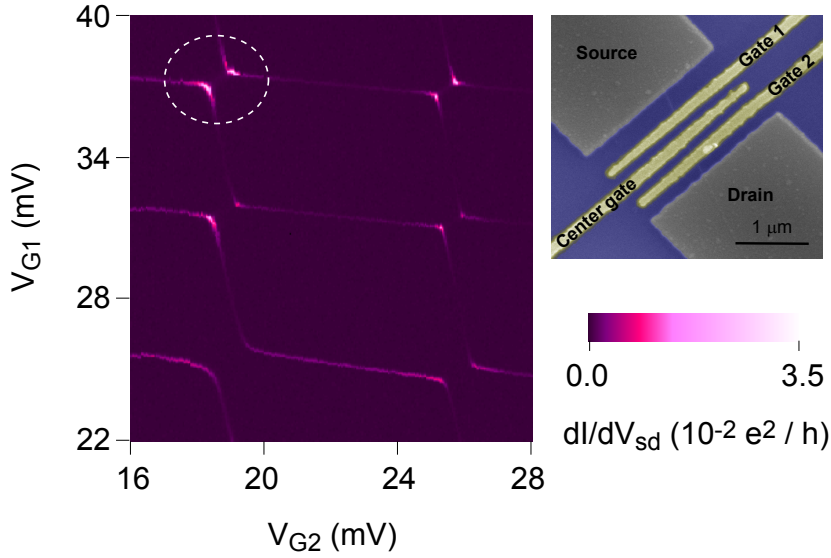

Figure 5.8: Colorscale plot of the differential conductance (linear scale) versus gate 1 and gate 2 for the third device, exhibiting a honeycomb pattern. Data are taken at base temperature of our dilution refrigerator, $T_{el} \approx 50$ mK. On the top right, an SEM micrograph of a device identical to the one measured is shown.

acts a double quantum dot. Figure 5.8 shows a colorscale plot of the differential conductance of the device versus gates 1 and 2 at a center gate voltage of 0 V, a back-gate voltage of 0 V, and a bias of $V_{sd} = 20\mu$V. The honeycomb edges exhibit a strong curvature in the vicinity of the triple point regions and transport is enabled on the edges as well. As pointed out before, both features indicate the formation of coherent, molecular states in the system. We will now focus on the upper left triple point region shown in Fig. 5.8, marked by a dashed circle.

Figure 5.9(a) shows a colorscale plot of the conductance of this region versus single particle energies E_1 and E_2. The conversion from gate voltages to energies has been carried out using the width of the honeycomb edges at finite bias yielding the conversion factors $\alpha_1 = 0.65\,e$ and $\alpha_2 = 0.6\,e$. From the spacing of the two high-conductance wings and Eq.(5.2) we determine a tunnel coupling $t \approx 200\,\mu$eV $\gg U'$. The spacing E_Δ versus detuning and the corresponding fit (parameters are $t = 217\,\mu$eV, $U' = 0$) are shown on the right-hand side of Fig. 5.9(a).

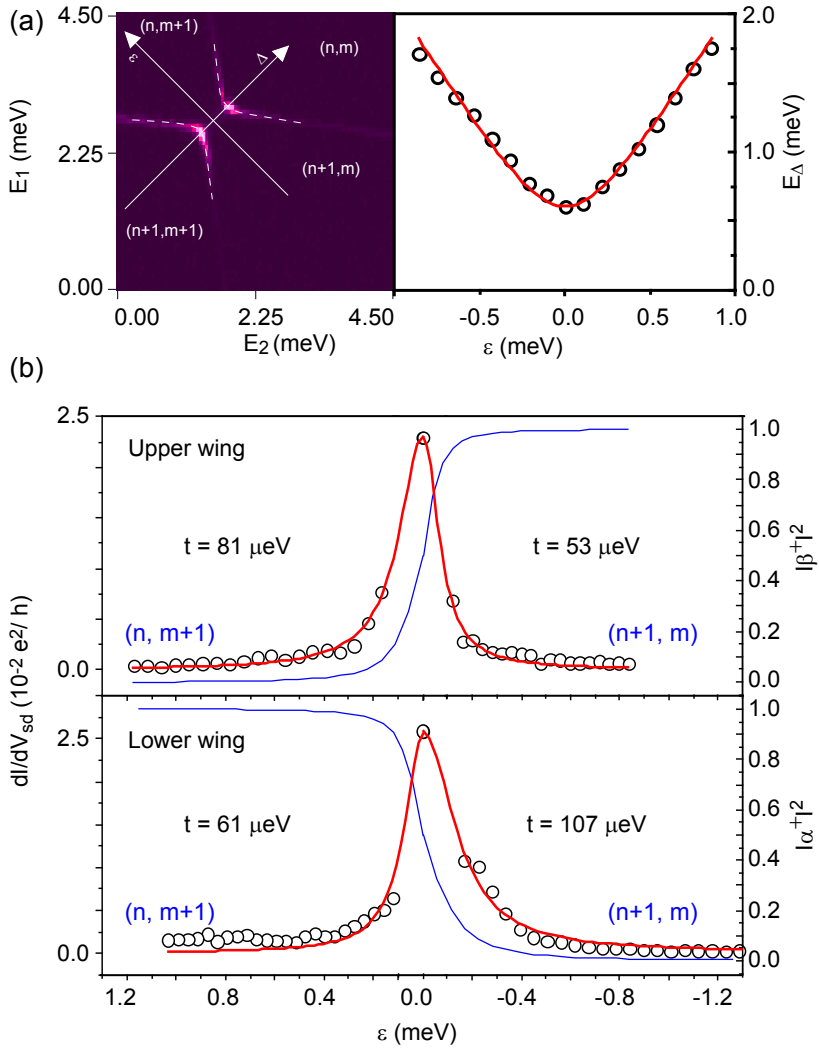

Figure 5.9: (a) Colorscale plot of the differential conductance in a triple point region versus energies E_1 and E_2, exhibiting a tunnel-induced anti-crossing. Dark corresponds to 0, bright to $0.035\, e^2/h$. (b) Conductance traces dI/dV_{sd} (left-hand vertical scale) and corresponding fits according to Eq.(5.6) versus detuning ϵ for the upper and the lower wing of (a). Right-hand vertical scale: Coefficients α^+ or β^+, calculated with the given values of t, obtained from the fit. Due to the strong curvature of the wings, it is difficult to extract more data points with a precise value of ϵ for the center of the peaks. At the maximum of differential conductance, ϵ was set 0.

The conductance through the molecular eigenstates along the wings is expected to reach its maximum when the detuning $\epsilon = 0$. From Eq.(5.3) one sees that the differential conductance falls off with $\mid \alpha\beta \mid^2$, where

$$\mid \alpha^{\pm}(\epsilon) \mid^2 = \frac{2t^2}{2t^2 + (\epsilon \pm \sqrt{\epsilon^2 + 2t^2})^2} \tag{5.4}$$

$$\mid \beta^{\pm}(\epsilon) \mid^2 = 1 - \mid \alpha^{\pm}(\epsilon) \mid^2 \tag{5.5}$$

are the coefficients of the superposed wavefunction $|\Psi\rangle = \alpha\,|n, m+1\rangle + \beta\,|n+1, m\rangle$, as given in Chapter 2. The ground state (bonding state), through which transport occurs at low bias, is denoted by '+'. In Fig. 5.9(b) the conductance versus detuning is extracted for the upper and lower wing. Here, the upper wing is the one adjacent to (n,m) and the lower wing is the one adjacent to (n+1,m+1). The conductance traces are fit to

$$dI/dV_{sd}(\epsilon) = const \times \mid \alpha(\epsilon)\beta(\epsilon) \mid^2 \tag{5.6}$$

independently for positive and negative detuning. The coefficients $\mid \alpha \mid^2$ and $\mid \beta \mid^2$ follow consequently and are added in Fig. 5.9(b) (blue line, right-hand vertical scale). This can be considered a mapping of the molecular wavefunction. The fits yield tunnel couplings about a factor 2-4 smaller than obtained by fitting the curvature of the two wings. The obtained values of t are noted in Fig. 5.9(b), next to the corresponding conductance trace. It is difficult to estimate the uncertainty of t, satisfactory fits are obtainable within a range of roughly $t \pm t/5$. Additionally, the tunnel couplings obtained for positive and negative detuning are not symmetric. We can only speculate about the origin of the deviations. A dependence of the tunnel coupling on the detuning can be excluded as explanation, as such behavior would show up in the spacing of the two wings as well. Taking into account the fitting curves are mainly determined by their tails, co-tunneling processes taking place at these positions could have an influence on the conductance trace. We emphasize, however, that these measurements are taken at a very low temperatures of the order 50 mK and at small source-drain bias. Hence, we expect co-tunneling processes to be strongly suppressed. Recalling the deviations from $1/T$-scaling of the temperature dependence of the differential conductance, see Section 5.6, our simple model of spinless transport through a single molecular level cannot fully capture quantitatively the conductance through the system.

5.10 Summary

In this Chapter local top-gate electrodes were used in order to define double quantum dots in SWNTs. Measurements of three devices strongly suggest that the double dots are indeed gate-defined and not intrinsic to the nanotube. In a detailed analysis we were able to trace tunnel-coupled, molecular eigenstates of the double dot and precisely quantify the tunnel coupling t. Carbon nanotube

artificial molecules are unique, in that the tunnel coupling t can strongly exceed the electrostatic nearest-neighbor interaction between the artificial atoms. To our knowledge, this is the first time that such molecular states have been measured and carefully analyzed in carbon nanotube double quantum dots. In our analysis we have restricted ourselves to the charge degree of freedom. Future experiments, possibly in the few electron or hole regime, will have to address superposed spin states and spin lifetimes. Using spin-injection and superconducting proximity, both of which have been demonstrated in carbon nanotube devices, new functionality may be added to double quantum dot devices.

Due to their unique properties and their experimental ease, carbon nanotube double quantum dot systems help to address fundamental issues of quantum mechanics and may play an important role in future information technology.

References

[1] C. Livermore *et al.*, Science **274**, 1332 (1996).

[2] R. Blick *et al.*, Phys. Rev. Lett. **80**, 4032 (1997).

[3] A. Holleitner *et al.*, Science **297**, 70 (2002).

[4] J. Petta *et al.*, Science **309**, 2180 (2005).

[5] J. Elzermann *et al.*, Phys. Rev. B **67**, 161308 (2003).

[6] G. Burkard, D. Loss, and D. P. DiVincenzo, Phys. Rev. B **59**, 2070 (1999).

[7] W. van der Wiel *et al.*, Rev. Mod. Phys. **75**, (2003).

[8] N. Mason, M. Biercuk, and C. Marcus, Science **303**, 655 (2004).

[9] M. Biercuk *et al.*, Nano Letters **5**, 1267 (2005).

[10] C. Fasth, A. Fuhrer, M. Björk, and L. Samuelson, Nano Letters **5**, 1487 (2005).

[11] S. Sahoo *et al.*, Nature Physics **1**, 99 (2005).

[12] M. Buitelaar, T. Nussbaumer, and C. Schönenberger, Phys. Rev. Lett. **89**, 256801 (2002).

[13] Y.-J. Doh *et al.*, Science **309**, 272 (2005).

[14] M.-S. Choi, C. Bruder, and D. Loss, Phys. Rev. B **62**, 13569 (2000).

[15] J. Furer, *PhD Thesis* (unpublished, University of Basel, 2005).

[16] J. Appenzeller, Y.-M. Lin, J. Knoch, and P. Avouris, Phys. Rev. Lett. **93**, 196805 (2004).

[17] V. Golovach and D. Loss, Phys. Rev. B **69**, 245327 (2004).

[18] R. Ziegler, C. Bruder, and H. Schoeller, Phys. Rev. B **62**, 1961 (2000).

[19] K. Matveev, L. Glazman, and H. Baranger, Phys. Rev. B **54**, 5637 (1996).

Appendix A

Electrical measurements and cryostats

A.1 Measurement setup

A typical setup for our electrical transport measurements is illustrated in Fig. A.1. Mostly, a lock-in technique was used with excitation voltages ≈ 10 μV. Best results were obtained when using an I/V-converter (gain $10^7 - 10^9$) and a so-called ground loop killer (gain 10), which breaks low-impedance ground loops. An essential ingredient is the filtering incorporated which is needed to ensure an electronic temperature somewhat similar to the phononic bath temperature. In our setup, there are two stages of filtering.

1. π-filters at room temperature: A π-filter is a combination of two capacitors and an inductor which gets its name from the resemblance of the equivalent circuit to the symbol 'π'. The filters used provide a damping of 40-60 dB for frequencies ≥ 0.3 MHz [1].

2. Microcoax filters at base temperature: These are thin, ≈ 1 m long, coaxial cables consisting of a central conductor (resistive wire with a resistivity of 1.32 $\mu\Omega$m, coated with insulating varnish), and an outer jacket (stainless steel, resistivity 0.71 $\mu\Omega$m). Due to the skin effect the losses in such coaxial cable go with $\sqrt{\omega}$. Ref. [2] gives an attenuation per unit length of ≈ 60 dB/m at 1 GHz and ≈ 200 dB/m at 10 GHz for such a geometry.

The wiring in between the two filtering stages from 300 K to base temperature is done with constantan (Cu55/Ni45) wires (Kelvinox) and either phosphorbronze (Cu94/Sn6) or manganin (Cu84/Ni4/Mn12) wires (He3).

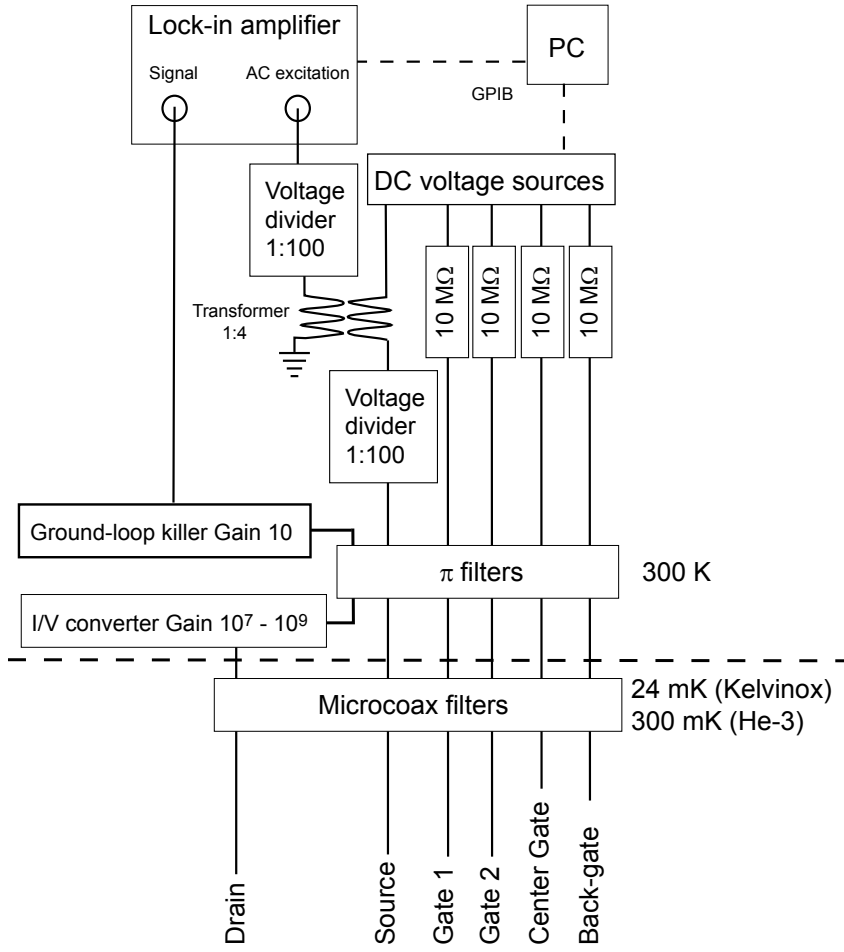

Figure A.1: Schematic of the electrical setup used for measurements of carbon nanotube double quantum dot devices.

A.2 Electronic temperature

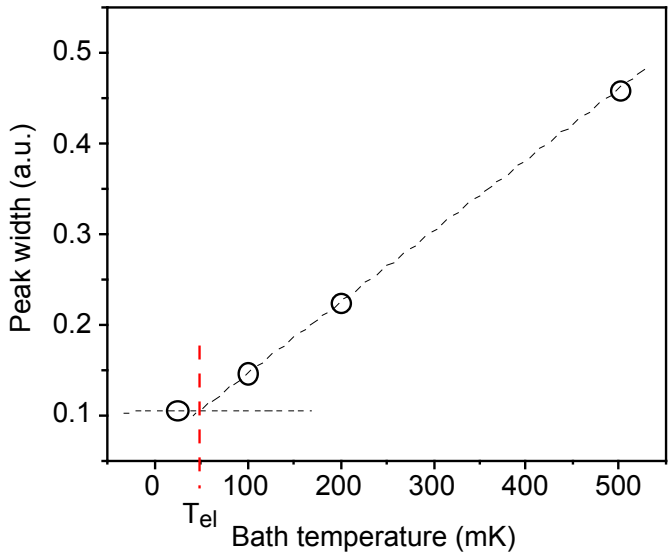

Figure A.2: Width of measured Coulomb peaks in a carbon nanotube double quantum dot versus bath temperature.

In Fig. A.2 the width of measured Coulomb peaks in a carbon nanotube double quantum dot is plotted versus the bath temperature of our Kelvinox dilution refrigerator. For temperatures higher than 100 mK the peak-width is proportional to the bath temperature. The peak-width at base temperature (24 mK), however, does not lie on the line defined by the other temperatures. From the intersect of this line and a horizontal one through the base-temperature data one obtains an effective electronic temperature of $T_{el} \approx 50$ mK.

A.3 Cryostats

Within this work the following cryostats have been used:

- ^{4}He storage dewar, T = 4.2 K.
- ^{4}He cryostat, base temperature 1.7 K.
- ^{3}He cryostat, base temperature 300 mK.
- Kelvinox ^{3}He/^4He dilution refrigerator, base temperature 25 mK.

Whereas the dewar and a dip-stick represent the simplest possible refrigerator and will not be further discussed here, both the ^{4}He and the ^{3}He-cryostat of our group have been described elsewhere [1, 3]. As during my Ph.D. work we had to face quite a few problems with the Kelvinox dilution refrigerator, the system is very briefly discussed in the following.

The principle of operation of a dilution refrigerator is that a mixture of the two isotopes ^{3}He and ^{4}He separates into two phases below a critical temperature (T_{cr} = 0.86 K). The concentrated, lighter phase (rich in ^{3}He, $\approx$ 90 %) then floats on top of the heavier dilute phase (typically 6-7 % ^{3}He). According to the unique phase diagram of ^{3}He/^{4}He mixtures, the dilute phase is superfluid, i.e. a quantum fluid, the concentrated phase, however, remains a normal liquid. When now the concentrated phase is transferred (pumped) into the dilute (superfluid) one it will be in an 'excited' state, which costs energy. The environment provides this energy and gets cooled, consequently.

Figure A.3 shows the operation diagram of a Kelvinox dilution refrigerator. The phase boundary is located (ideally) inside the mixing chamber, which the coldest part of the refrigerator. If the phase boundary is not located in there, but for example in the small tubes connecting to the still stage, the cooling power will be drastically reduced. The position of the phase boundary can be controlled by the amount of ^{3}He in the mixture. Our current mixture contains 7.5 l ^{3}He and 36 l^{4}He. Due to osmotic pressure the dilute phase goes up to the still and is evaporated there by an applied heating power of, in our case $\approx$ 3-5 mW. The evaporated phase is again rich in ^{3}He, gets pumped through the ^{3}He pump outside the fridge and finally recondensed in the condenser (cooled by the 1-K pot at a temperature of $\approx$ 1.5 K). After it has been cooled in the heat exchangers by the outgoing dilute phase, the concentrated phase is then introduced into the mixing chamber and the cycle starts over. In our dilution refrigerator, the cooling power ($\approx$ 5 μW) was much less than the specified one of 100 μW at 100 mK. In addition the base temperature was only of the order 50-100 mK. Most likely, there was a crossover-leak, located somewhere in the heat exchangers. There is almost no way of detecting such a crossover-leak, as the mixture still remains in a closed cycle. However, only parts of the concentrated phase are transferred through the mixing chamber. Instead a big amount of it takes a bypass through the crossover-leak located in the heat exchangers. After the heat exchangers were exchanged, the system operated fully according to its specifications and reached a base temperature of 18 mK (without sample holder).

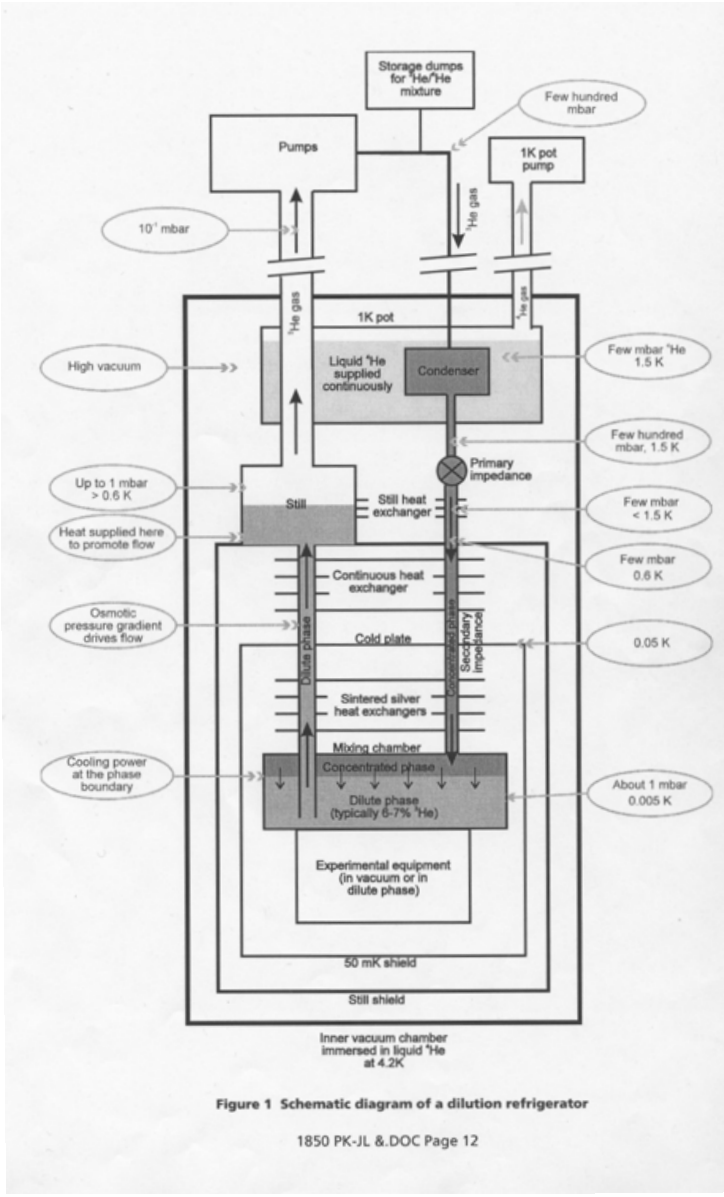

Figure A.3: Schematic of a dilution refrigerator. Taken from the Kelvinox manual [4]

Appendix B

Additional data

B.1 Approaching the few-hole regime

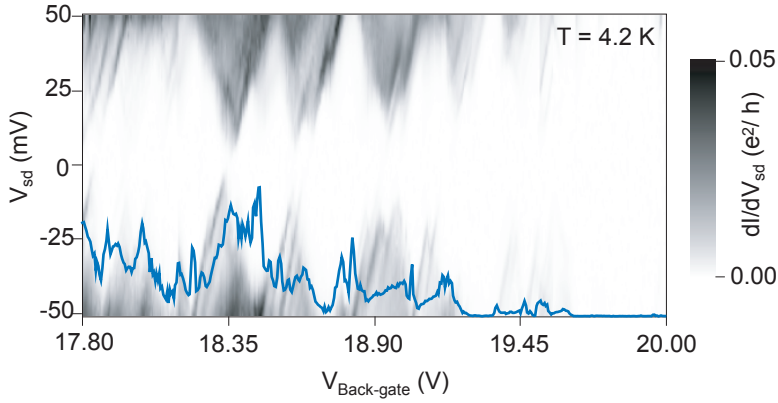

Figure B.1: Colorscale plot of the differential conductance versus source-drain bias voltage and back-gate. Trace of the linear differential conductance at V_{sd}=-50 mV.

Figure B.1 shows a colorscale plot of the differential conductance at 4.2 K through a nanotube device with 2 top-gates (for this measurement kept at 0 V, same device as described in Chapter 4) for high back-gate voltages, i.e. when approaching the energy gap of the semiconducting tube. Different energy scales are evident from differently-sized Coulomb diamonds, suggesting that more than a single quantum dot is involved in transport. Close to the gap, the charging energy increases dramatically up to more than $\approx$ 50 meV. This is in agreement

with the first measurement of the few electron / hole regime in SWNT [5]. However, extracting the precise number of holes residing on the dot(s) is not possible from our data.

B.2 Influence of the center gate on the dot-dot coupling

Figure B.2(a) and (b) show the same region of the first double-dot sample described in Chapter 5 for two different voltages applied at the center gate. For a more positive voltage (b), the honeycomb pattern looks more rectangular, i.e. the dots are more decoupled.

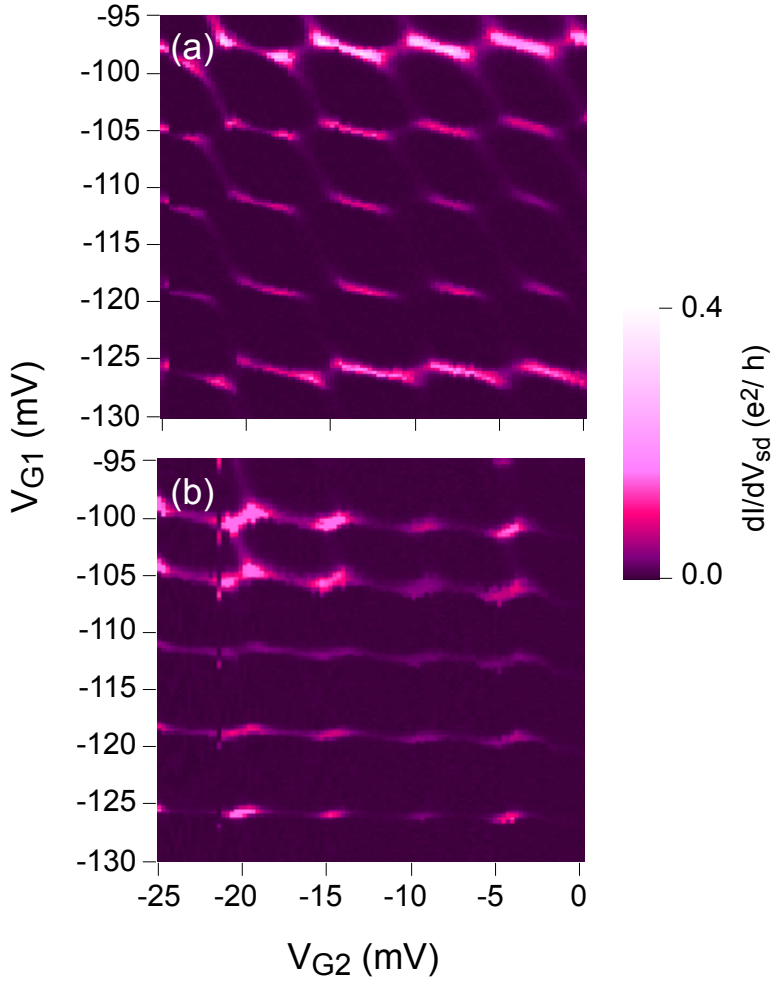

Figure B.2: Colorscale plot of the differential conductance versus gate voltages applied at top-gates 1 and 2 for two different voltages applied at the center gate: (a) V_{Center} = -0.1 V. (b) V_{Center} = 0.1 V. The temperature is 300 mK and the applied bias 128 μV. $V_{back-gate}$ =0 V.

Appendix C

CVD-growth recipe for single-walled carbon nanotubes

C.1 Catalyst preparation

Catalyst composition

The liquid based catalysts consist of the following components iron nitrate ($Fe(NO_3)_3$-$9H_2O$), molybdenum dioxide dichloride (MoO_2Cl_2) and alumina (Al_2O_3) in different combinations. The alumina nanopowder is used with two different particle sizes with diameters of 4 and 40 nm. The solvents are water, methanol, ethanol and 2-propanol (isopropylic alcohol). The composition is similar to that of the catalyst used by Kong et al. [6]. But there is a difference in the recipe, MoO_2Cl_2 is used instead of MoO_2 which was not available.

The catalyst is prepared with stock solutions that guarantee a constant composition over time. 30 mg Al_2O_3 (either 4 or 40 nm nanopowder) is dissolved in 20 ml 2-propanol, 93 mg $Fe(NO_3)_3$-$9H_2O$ is dissolved in 20 ml 2-propanol and 27 mg MoO_2Cl_2 is dissolved in 20 ml 2-propanol. These stock solutions are sonicated over night with an Ultrasonic300, power and degas in middle position. Next, they are mixed to the actual catalyst consisting of 0.5 ml alumina solution (either 4 or 40 nm), 0.5 ml iron nitrate solution and 0.5 ml molybdenum dioxide dichloride solution diluted with 18.5 ml 2-propanol to a final volume of 20 ml. The catalyst is sonicated overnight after mixing and for 2 hours prior to use. (This corresponds to final concentrations of 0.37 mM Al_2O_3, 0.29 mM $Fe(NO_3)_3$-$9H_2O$ and 0.17 mM MoO_2Cl_2, respectively.)

Sample preparation:

The catalyst is sonicated 2 hours prior to use. The samples are sonicated in acetone for 5 minutes and in 2-propanol for 2 minutes as well as placed in the UV cleaner for 10 minutes. Simultaneously the biggest clusters are removed by a sedimentation step that lasts between 10 to 30 minutes. The sample (Si/SiO_2 substrate, area $\approx$ 2 cm $\times$ 2 cm) is placed on a spinning table (2'000 rpm for 40 seconds), 1 droplet of catalyst is added when the maximal speed is reached.

C.2 Growth protocol methane/hydrogen process

Here the step by step protocol for the methane/hydrogen CVD process is given. With this recipe, the SWNT with the highest quality have been grown. For more details about the setup of gas systems see Chapter 1. The effect of room temperatures deviating from the calibration temperature 20 °C is negligible ($< 2\%$). The gas system is operated with three gas lines for argon, hydrogen and methane, respectively. The pressure drop over the flowmeters is set to 0,2 bar, using the reduction valves of the gas bottles. This makes a pressure correction unnecessary. For more information about corrections necessary when using flowmeters, see [7].

1. Mount sample, close tube.
2. Open all gas valves (Ar (check if there are bubbles), CH_4, H_2).
3. Flush the lines for 2 minutes.
4. Close H_2 and CH_4 valves.
5. Keep Ar flowing at 1'500 ml/min±3% (The reading at the variable area flow meter is 105 l/h, this corresponds to a corrected flow of: $\frac{105'000ml}{60min}\sqrt{\frac{1.293}{1.784}} = 1'489ml/min.$)
6. Heat-up oven to 900 °C.
7. Open H_2 flow up to 500 ml/min±3% (The reading at the variable area flowmeter is 8 l/h, this corresponds to a corrected flow of: $\frac{8'000ml}{60min}\sqrt{\frac{1.293}{0.090}} = 505ml/min$).
8. Close Ar.
9. Open CH_4 up to 1000 ml/min±3% (The reading at the variable area flowmeter is 45 l/h, this corresponds to a corrected flow of: $\frac{45'000ml}{60min}\sqrt{\frac{1.293}{0.717}} = 1'007ml/min$).
10. Leave the gasses flowing for 10 minutes.
11. Open up Ar up to 1.5 l/min (leave H_2 open).

12. Close CH_4.
13. Let oven cool down to 550 °C.
14. Close H_2.
15. Unmount sample when temperature $\leq$ 350 °C.
16. Close Ar.

References

[1] S. Oberholzer, *PhD Thesis, University of Basel* (Logos Verlag, Berlin, 2001).

[2] A. Zorin, Rev. Sci. Instrum. **66**, 4296 (1995).

[3] M. Buitelaar, *PhD Thesis* (unpublished, University of Basel, 2002).

[4] Oxford Instruments Superconductivity, *Kelvinox Dilution Refrigerator and Superconducting Magnet system. Operator's Handbook* (Oxford Instruments, Tubney Woods, Abingdon, UK, 2001).

[5] P. Jarillo-Herrero *et al.*, Nature **429**, 389 (2004).

[6] J. Kong *et al.*, Nature **395**, 878 (1998).

[7] J. Furer, *PhD Thesis* (unpublished, University of Basel, 2005).

Publication list

Publications in journals and proceedings:

- *Quantum dot coupled to a normal and a superconducting lead.*

  M.R. Gräber, T. Nussbaumer, W. Belzig, and C. Schönenberger, Nanotechnology **59**, 2871 (2004).

- *Kondo resonance in a carbon nanotube quantum dot coupled to a normal and a superconducting lead.*

  M.R. Gräber, T. Nussbaumer, W. Belzig, T. Kontos, and C. Schönenberger, Proceedings of the XXXIXth Rencontres de Moriond on quantum coherence and computing, 363 (2004).

- *Electrical field control of spin.*

  S. Sahoo, T. Kontos, J. Furer, C. Hoffmann, M.R. Gräber, A. Cottet, and C. Schönenberger, Nature Physics **1**, 99 (2005).

- *Molecular states in carbon nanotube double quantum dots.*

  M.R. Gräber, W. A. Coish, C. Hoffmann, M. Weiss, J. Furer, S. Oberholzer, D. Loss, and C. Schönenberger, to be published in Physical Review B (2006).

- *Defining and controlling double quantum dots in single-walled carbon nanotubes.*

  M.R. Gräber, M. Weiss, and C. Schönenberger, to be published in Semiconductor Science and Technology (2006).

Poster contributions:

- *Quantum dot coupled to a normal and a superconducting lead*

  M. R. Gräber, T. Nussbaumer, T. Kontos, and C. Schönenberger

  Poster at the International Summer School on dynamics of interacting electrons in quantum wires, Miraflores, Spain, Sept. 27th - Oct. 4th , 2003.

- *Quantum dot in the Kondo regime coupled to a normal and a superconducting lead*

  M. R. Gräber, T. Nussbaumer, W. Belzig, T. Kontos, and C. Schönenberger

  Poster at the XXXIXth Rencontres de Moriond on quantum information and decoherence in nanosystems, La Thuile, Aosta Valley, Italy, Jan. 25th - Feb. 1st, 2004.

- *Quantum dot in the Kondo regime coupled to a normal and a superconducting lead*

  M. R. Gräber, T. Nussbaumer, W. Belzig, T. Kontos, and C. Schönenberger

  Poster at the Gordon Research Conference on nanostructure fabrication, Tilton, NH, USA, July 18th - July 23rd 2004.

- *Carbon nanotube double quantum dots*

  M. R. Gräber, W.A. Coish, C. Hoffmann, J. Furer, M. Weiss, S. Oberholzer, D. Loss, and C. Schönenberger

  Poster at the German-US GDEST Workshop on "Quantum information and Coherence", München, Germany, December 8th - December 9th 2005.

- *Carbon nanotube double quantum dots*

  M. R. Gräber, W.A. Coish, C. Hoffmann, J. Furer, M. Weiss, S. Oberholzer, D. Loss, and C. Schönenberger

  Poster at the annual meeting of the Swiss Physical Society, Lausanne, February 13th - February 14th 2006.

Talks:

- *An artificial molecule inside a carbon nanotube.*

  Talk at the annual meeting of the Swiss Physical Society, Bern, July 14th 2005.

- *Carbon nanotube quantum electronics*

  Invited talk at Ciba Specialty Chemicals, Basel, November 21st 2005.

- *An artificial molecule inside a real one: Carbon nanotube double quantum dots*

  Invited talk at Sony Stuttgart Technology Center, Stuttgart, December 1st 2005.

- *The influence of the metal-molecule interface on charge transport through molecules*

  Invited talk at Sony Stuttgart Technology Center, Stuttgart, February 7th 2005.

- *Carbon nanotube double quantum dots.*

  Talk at the annual meeting of the Swiss Physical Society, Lausanne, February 14th 2006.

For valuable lectures and experimental guidance during my studies I am indebted to:

Karlsruhe

G. Schön, M. Wegener, O. Knab, F. Wenzel, T. Mannel

Hamburg

D. Fay, D. Grundler, D. Heitmann, G. Mack, U. Merkt, W. Metz, M. Schilling, C. Schüller, B. Sonntag, G. Zimmermann

Buffalo, NY

F. Gasparini, B. McCombe, R. Gonsalves

Toronto

J. Wei

Basel

C. Schönenberger, W. Belzig

Acknowledgements

At the end of this thesis I would like to thank the people whose support was essential for my doctoral research. Let me first thank my supervisor Prof. Christian Schönenberger for giving me the opportunity to pursue a PhD in his group. I have very much benefitted from his scientific advice and support. Thanks also to the co-referees Prof. Wolfgang Belzig and Prof. Jörg Kotthaus for reading through my thesis and the interesting discussions during my defense talk.

The low-temperature experiments have been conducted in close collaboration with the postdocs Thomas Nussbaumer, Christian Hoffmann, and Markus Weiss. For further experimental support thanks to the current and former members of the Schönenberger group, namely Laetitia Bernard, Erasmus Bieri, Mark Buitelaar, Michel Calame, Bong-Ryoul Choi, Francois Dewarrat, Alex Eichler, Jürg Furer, Lucia Grüter, Teresa Gonzalez, Adam Hansen, Roman Huber, Soufiane Ifadir, Dino Keller, Andreas Kleine, Takis Kontos, Jianhui Liao, Zuquin Liu, Stefan Oberholzer, Sangeeta Sahoo, Jelena Trbovic, Songmei Wu, and Zheng-Ming Wu. For theoretical input, I greatly appreciate discussions with Bill Coish, Patrik Recher, Prof. Christoph Bruder, and Prof Daniel Loss.

Special thanks to the team of the mechanical workshop and the technology group, in particular Werner Roth for the supply with cryogenic liquids and Peter Reimann for assistance recording a video of a double quantum dot device (http://pages.unibas.ch/phys-meso/PublicRelation). Moreover, the expertise of the electronics workshop around Michael Steinacher made life and experiments a lot easier. Thanks a lot.

Financial support for this work has been provided by the Swiss National Science Foundation, the NCCR on Nanoscience, the University of Basel, and the "Camille und Henry Dreyfus Stipendium".

Finally I would like to thank Anna Schorner for her support in generating the print output of this thesis.